DOCTORAL THESIS

MAGNETIC VORTEX NANODISCS FOR CANCER CELL DESTRUCTION

MAITE GOIRIENA GOIKOETXEA

SUPERVISOR: ALFREDO GARCÍA ARRIBAS

2017

eman ta zabal zazu

Universidad del País Vasco
Euskal Herriko Unibertsitatea

Acknowledgements

This Thesis has been carried out thanks to a pre-doctoral fellowship funded by the BCMaterials (Basque Center for Materials, Applications and Nanostructures), which is included within the Basque Excellence Research Centers (BERC).

En primer lugar, quiero agradecer a mi director, Alfredo García Arribas. Gracias por haberme guiado durante estos casi cinco años de tesis, he aprendido mucho de ti. Pero, sobre todo, quiero agradecerte por el apoyo que me has dado y por la confianza que has tenido siempre en mí. Gracias por tu sentido del humor y por tu cercanía, no he podido sentirme más a gusto.

No puedo olvidar al Prof. Luis León, que fue mi tutor durante el máster de Nuevos Materiales y el que me impulsó a entrar en el mundo de la investigación. Sin su apoyo no habría conocido al que hoy en día es mi grupo de investigación, el grupo de Magnetismo y Materiales Magnéticos de la Universidad del País Vasco.

Asimismo, quiero agradecer al que en aquel momento era el director del grupo, el Prof. Manu Barandiaran, por acogerme con los brazos abiertos. Manu ha sido, sin duda, un pilar fundamental en el comienzo de mi carrera científica.

Esta Tesis habría sido imposible sin la ayuda de la gente del grupo de Magnetismo y Materiales Magnéticos. En especial Edu y Pablo, que me ayudaron a salir del cascarón; Iñaki por todos los MOKE/SQUID/FORC/VSM y otras medidas con muchas siglas y, sobre todo, por el buen rollo; Valentín, por ayudarnos a arreglar el RIE; Andrey, por tantas horas de *sputtering*; Javi Alonso, por transmitir esa serenidad; y Malú, por toda su ayuda y consejo. No puedo olvidarme de Jorge Feuchtwanger, que forma parte de todos los grupos del departamento; gracias por resolverme tantas dudas y por estar siempre dispuesto a ayudar.

I would like to thank Prof. Cowburn for giving me the opportunity of working within his group at the Cavendish Lab (Cambridge, UK). It was a great experience in all senses. Special thanks for Rhodri Mansell, Emma Welbourne and Tarun Vemulkar for helping me with the experiments. Thanks Alex, Dédalo, Amalio, Jung-Wei, Lucy, Linda, Dorothée, Shin and Spencer for your kindness and good moments.

También me gustaría agradecer a Alicia Muela y a David Muñoz por acogerme en su laboratorio e introducirme en el mundo de la biología. La biomedicina es un área que me fascina y me siento muy agradecida por haberles tenido como mentores.

Tesiko ixe bost urte honek oso zoriontsuek izen dire niretzat. Zenbat barre, bazkari, eskapada ta momentu on, aupa Electricity! Ezin naz hasi banaka-banaka eskerrak emoten, bakoitzagaz kapitulo bat idatzi ahalko nekelako, bakarrik esan ahal dotsuet asko maitxe zaitzuetela ta bizitza osorako lagunek zariela; Irati, Lulu, Anabel, Iraultza, Garaio, Libe, Popi, Janire, Mattin, Edu, Luca, Dani, Eugen, Esti, Inari, Rakel, Ivan, Andoni, Catarina. Zuen zatitxu bana daroat nigaz.

Zelan ahaztu nire kuadrilie, tesitik aparte bizixe dauela gogorarazten dostienak. Batez be, beti hor zauzienak, Ana ta Jani, eskerrik asko zuen laguntasunegaitxik.

Eskerrik beroenak nire familixentzako: ama, aita, Iraia ta Olatz, ez bakarrik tesiko azkeneko hillietan ni jasatiarren, bizi osoan emon dostazuen indar eta maitxasunegaitzik baino. Zer eingo neke zuek barik!

Eskerrik asko Eneko, zure alboan politxaua ta errezaua dalako dana.

Baina tesi hau, berezi-bereziki, nire amuma Susana eta amuma Andereri eskeini nahi dotsatie, oin dala urte batzuk asko gure albotik juan arren, zuen altzoan zelan egoten nintzen akordetan nazelako. Erre ez zituzten sorgiñen lobak garelako.

“Imagination creates reality.”

Richard Wagner

Contents

Introduction

The present Thesis addresses the study of $Ni_{80}Fe_{20}$ (Permalloy) nanodiscs in the magnetic vortex state, from synthesis to application. This brief introduction intends to emphasize the novelty of the research and concomitantly, the motivation for which this work has been developed, along with the exposition of the main objectives.

The vortex state, characterized by the magnetic moments being curled in the plane of the disc and, therefore, by a null net magnetisation at remanence, possesses attractive features for emerging multidisciplinary applications such as magnetic information storage, spintronics and, especially, biomedicine. In magnetic information storage, the vortex spin configuration is expected to display smaller thermal and quantum fluctuations than conventional systems, as it comprises many spins [1]. Vortex-state discs are also used as an active layer in spin-torque nano-oscillators generating signals in the microwave range excited by a DC spin-polarized current [2]. Furthermore, vortex-state discs, dispersed in water, can act as magneto-mechanical actuators: the force generated by their oscillation in a low amplitude and low frequency magnetic field is capable of damaging the membrane of cancer cells [3, 4] or to be used as drug delivery agents [5]. Indeed, the vortex configuration in micro- and sub-micrometric discs has been extensively studied [6-9] and they have already been demonstrated to destroy cancer cells. The downscaling of this attractive magnetic structure could definitely expand the possibilities of the applications, *e.g.*, increasing magnetic memory storage density and favouring internalization by the cells for biomedical applications. Despite its relevance, very few works deal with the study of the magnetisation in sub-100 nm vortex discs [10, 11] and, to the best of our knowledge, no work in the literature reports their application in biomedicine. It is in this scenario where the initiative for the present Thesis arose.

Thereupon, we planned the strategy of the work by setting three ambitious objectives:

Objective 1. Development of a low-cost and high-yield fabrication technique to prepare sub-100 nm Permalloy discs in the vortex state.

Objective 2. Uncovering of the magnetic behaviour of sub-100 nm Permalloy discs.

Objective 3. Study of the suitability of the nanodiscs to destroy cancer cells by magneto-mechanical actuation.

The execution of each objective constitutes a chapter of the Thesis.

Disc-shaped sub-100 nm structures can be fabricated by different lithographic methods. Among them, electron-beam lithography (EBL) and deep-ultraviolet lithography (DUV) allow for the best control of the shape and the size of the nanostructure. However, EBL suffers from an extremely low yield production, and DUV requires very expensive equipment that is not often available for research purposes. The first objective of the Thesis implied the development of an alternative technique applicable to a wide range of laboratories, with no need of sophisticated equipment, while allowing for a high production yield, at least capable of producing nanostructures in a quantity enough to assess the potential of the nanodiscs in biomedicine at laboratory level. Chapter 1 describes the search for the most appropriate bottom-up fabrication route, based on self-assembled templates, together with the morphological characterization of the nanostructures obtained with the selected preparation method.

The second objective of the Thesis consisted in developing a complete study of the magnetic behaviour of sub-100 nm Permalloy discs from the experimental, theoretical and analytical points of view. This challenge was faced in such a way as to delimit the range of geometries for magnetic vortex stability at the nanoscale and to uncover the particularities of the vortex configuration that arise at such small scale. Additionally, the magneto-mechanical capability of the nanodiscs in water was investigated for the application in cells. These studies are presented in Chapter 2.

Thirdly, the suitability of the nanodiscs for cancer cell treatment was studied in close comparison with the results obtained in micrometric discs. In this work, lung carcinoma cells were used for the *in vitro* experiments. The execution of this objective implied the study of the internalization process of the nanodiscs in cancer cells, along with their cytotoxic effect, and the influence of a low magnetic field on the viability of the cells. Chapter 3 covers the experiments and results obtained in this regard.

References

[1] B. Pigeau, G. de Loubens, O. Klein, A. Riegler, F. Lochner, G. Schmidt, L.W. Molenkamp, V. S. Tiberkevich and A. N. Slavin, "A frequency-controlled magnetic vortex memory", *Applied Physics Letters,* vol. 96, pp. 132506-3, 2010.

[2] S. Tsunegi, K. Yakushiji, A. Fukushima, S. Yuasa and H. Kubota, "Microwave emission power exceeding 10 mW in spin torque vortex oscillator", *Applied Physics Letters*, vol. 109, pp. 252402, 2016.

[3] D-H. Kim, E. A. Rozhkova, I. V. Ulasov, S. D. Bader, T. Rajh, M. S. Lesniak and V. Novosad, "Biofunctionalized magnetic-vortex microdiscs for targeted cancer-cell destruction", *Nature Materials*, vol. 9, pp. 165–171, 2010.

[4] S. Leulmi, X. Chauchet, M. Morcrette, G. Ortiz, H. Joisten, P. Sabon, T. Livache, Y. Hou, M. Carrière, S. Lequien and B. Dieny, "Triggering the apoptosis of targeted human renal cancer cells by the vibration of anisotropic magnetic particles attached to the cell membrane", *Nanoscale*, vol. 7, pp. 15904, 2015.

[5] D-H. Kim, P. Karavayev, E. A. Rozhkova, J. Pearson, V. Yefremenko, S. D. Bader and V. Novosad, "Mechanoresponsive system based on sub-micron chitosan-functionalized ferromagnetic disks", *Journal of Materials Chemistry*, vol. 21, pp. 8422, 2011.

[6] A-V. Jausovec, G. Xiong and R. P. Cowburn, "Cycle-by-cycle observation of single-domain-to-vortex transitions in magnetic nanodisks", *Applied Physics Letters*, vol. 88, pp. 052501-3, 2006.

[7] T. Shinjo, T. Okuno, R. Hassdorf, K. Shigeto and T. Ono, "Magnetic Vortex Core Observation in Circular Dots of Permalloy", *Science*, vol. 289, pp. 930-2, 2000.

[8] A. Wachowiak, J. Wiebe, M. Bode, O. Pietzsch, M. Morgenstern and R. Wiesendanger, "Direct Observation of Internal Spin Structure of Magnetic Vortex Cores", *Science*, vol. 298, pp. 277-3, 2002.

[9] E. K. Semenova, F. Montoncello, S. Tacchi, G. Dürr, E. Sirotkin, E. Ahmad, M. Madami, G. Gubbiotti, S. Neusser, D. Grundler, F. Y. Ogrin, R. J. Hicken, V. V. Kruglyak, D. V. Berkov, N. L. Gorn and L. Giovannini, "Magnetodynamical

response of large-area close-packed arrays of circular dots fabricated by nanosphere lithography”, *Physical Review B*, vol. 87, pp. 174432-19, 2013.

[10] R. K. Dumas, C.-P. Li, I. V. Roshchin, I. K. Schuller and K. Liu, “Magnetic fingerprints of sub-100 nm Fe dots”, *Physical Review B*, vol. 75, pp. 134405-5, 2007.

[11] I. V. Roshchin, C-P. Li, H. Suhl, X. Batlle, S. Roy, S. K. Sinha, S. Park, R. Pyn, M. R. Fitzsimmons, J. Mejía-López, D. Altbir, A. H. Romero and I. K. Schuller, “Measurement of the vortex core in sub-100 nm Fe dots using polarized neutron scattering”, *Europhysics Letters*, vol. 86, pp. 67008-5, 2009.

1

Fabrication of discs

Nanoparticles are typically synthesised by chemical routes, as it is the case of popular superparamagnetic iron oxide nanoparticles (SPION). Many techniques are able to produce uniform nanoparticles of different shapes by using appropriate precursors and capping ligands during the reaction [1]. Nevertheless, controlling the nanoparticle growth process can be challenging, and even the most successful approaches produce nanoparticles with non-negligible size and shape distributions [2]. Additionally, wet chemistry synthesis is still hampered by a relatively low yield [3], which prevents its implementation for mass production. Both drawbacks are especially important for medical applications where large amount of particles with reproducible shapes and properties are required.

Physical fabrication routes, which combine a lithographic method with a material deposition technique (*e.g.*, sputtering or thermal evaporation), allow for a tightly controlled material output with a well-determined structure shape, size and composition. Therefore, nanoparticles with a more complex structure than spheres, like discs, are more efficiently fabricated through physical approaches. Moreover, the ease control of the fabrication conditions makes the process automatic and reproducible. Physical fabrication methods can be classified into top-down and bottom-up processes; top-down methods are based on carving and shaping the desired structure from larger starting blocks, whereas bottom-up methods consist on building the desired structure from constitutive units.

The usual top-down procedure is to pattern a thin film of the selected material, deposited by evaporation or sputtering, into the desired structures by means of a suitable lithographic method. Microscale structures are almost exclusively fabricated by conventional photolithography or optical lithography. At smaller scales, electro-beam lithography (EBL) is the most used method, mainly for fundamental studies of the properties of the nanostructures [4–6]. However, the extremely low yield of EBL and its small area processing capability are great drawbacks for fabricating nanostructures for biomedical applications. Deep-ultraviolet (DUV) lithography, currently the industry standard for microelectronic fabrication, does not suffer from that restriction and it is probably the better-adapted technique for nanofabrication with exploitation at an industrial scale in mind. However, the required equipment is not often available for research purposes due to its elevated cost. Interference and nanoimprint lithographies are other promising alternatives for fabricating magnetic nanostructures [7, 8].

Nanofabrication approaches based on self-assembled templates, which are considered bottom-up procedures, are capable of combining inexpensive processing with large area coverage, thus providing an acceptable production yield. For instance, alumina membranes [9] and arrays of self-assembled nanospheres [10] have been successfully used to produce a rich variety of nanoarchitectures, including nanopillars [11, 12], nanorings [13, 14] and antidots [15, 16]. Interestingly, both alumina templates and nanosphere lithography (NSL) are also suitable to prepare disc-shaped structures. In the case of using alumina membranes, apart from the typical on-wafer dot structure [17], multi-segmented nanowires with modulated composition can be prepared [18]. In this way, large amounts of Permalloy nanodiscs can be fabricated by intercalating Ni-rich layers (*i.e.*, Permalloy) and Fe-rich layers and eventually removing the Fe-rich layers [19]. NSL, that uses a two-dimensional (2D) colloidal crystal of polystyrene spheres in a close packed hexagonal structure as template, has been also used to produce arrays of Permalloy nanodots [20, 21]. However, in practice, it is often difficult to obtain high quality monolayers of ordered spheres over large surfaces, and either empty regions or zones with multiple layers of spheres appear, limiting the usability of NSL. These problems are solved, in an alternative approach, using charged spheres that are sparsely distributed over the surface under the influence of electrostatic interactions. This method, denominated sparse colloidal lithography (SCL), produces typically less densely packed nanostructures, but improves the overall yield by extending the production area. The fabrication of nanostructures of different shapes has been demonstrated using the SCL technique with sizes down to about 20 nm [22]. Hole-mask colloidal lithography (HCL) was first introduced as an evolution of SCL to improve the versatility and usefulness of the technique [23]. It has been successfully used, for instance, to fabricate magneto-plasmonic nanostructures [24] and suspended nanodiscs for enhanced plasmonic biosensors [25].

1.1. Nanofabrication

For the fabrication of Permalloy nanodiscs, we opted for the development of bottom-up procedures as they guarantee a cost-effective and high-throughput fabrication process while allowing for good control of size, composition and shape of the nanostructures. Particularly, self-assembled templates were studied in order to find the optimum technique to prepare Permalloy discs.

The search for the most suitable fabrication technique was commenced using alumina templates and followed by nanosphere lithography. The experimental processes of the two approaches are described in the following section highlighting the advantages and disadvantages encountered in each case, which gave way to the selection of the definitive technique used in this work: hole-mask colloidal lithography.

1.1.1. Route search

A) Alumina membranes

The alumina membrane route implies the use of porous alumina as a template to create Permalloy discs over a substrate.

Alumina membranes were prepared by the two-step anodization technique [26], which involves four main steps (schematically illustrated in the Figure 1.1): (1) electropolishing of the aluminium to remove undesired materials from the surface of the metal, (2) first anodization of the aluminium to create the initial porous alumina, (3) removal of the porous alumina revealing a close-packed hexagonally ordered concave pattern and (4) second anodization to create the final porous alumina from the remaining pattern.

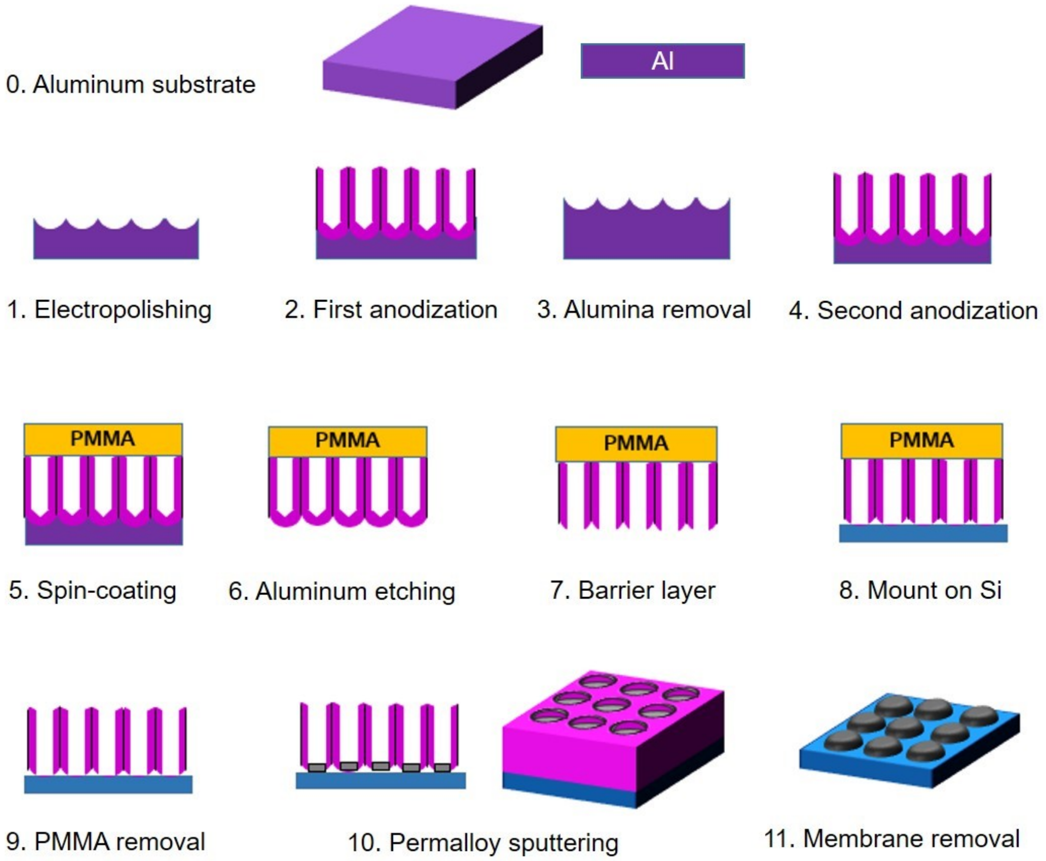

Figure 1.1. Flow diagram of the two-step anodization process to create nanostructures using alumina templates.

In our experimental set-up (Figure 1.2), leads of graphite acted as cathode and the aluminium itself as anode. The electrolyte for electropolishing was a mix of ethanol and perchloric acid (1:4) and a DC voltage of 20 V was applied (10 °C). The initial porous alumina was chemically removed by an aqueous solution of phosphoric acid (H_3PO_4, 0.4 M) and dichromic acid ($H_2Cr_2O_7$, 0.2 M) at 70 °C for about 12 h. Two different electrolytes were tested for the anodization steps: oxalic acid and phosphoric acid. The parameters for both anodization steps were obtained from the Thesis of Celia Tavares de Sousa *"Development of Nanoporous Alumina Templates for Biotechnological Applications"* (Universidade do Porto, 2011) and are collected in Table 1.1. The reactions that take place at the electrodes are as follows:

Reduction (Graphite): $3H^+ + 3e^- \rightarrow 1.5H_2$

Oxidation (Aluminium): $Al^0 \rightarrow Al^{3+} + 3e^-$

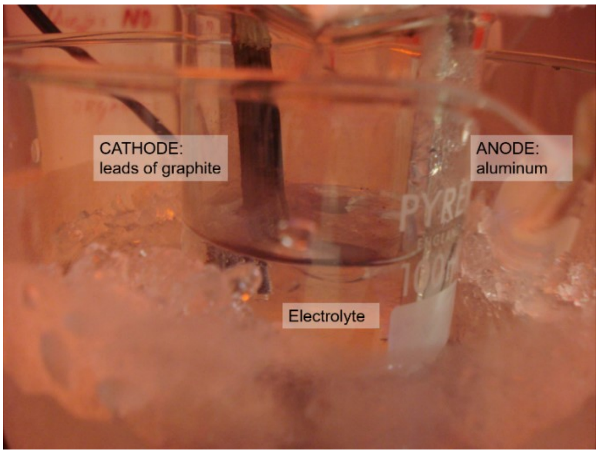

Figure 1.2. Anodization set-up consisting in a cathode of graphite, an anode of aluminium and the electrolyte of phosphoric acid.

Table 1.1. Anodization conditions for the two-step anodization process to create porous alumina templates.

Electrolyte	Concentration (M)	DC voltage (V)	Temperature (°C)	Anodization rate (μm/h)
H_2CO_4	0.3	40	4	2.5
H_3PO_4	0.1	195	1	2

The steps 2, 3 and 4 of the alumina membrane preparation were imaged by scanning electron microscopy, SEM (Figure 1.3). When using oxalic acid as electrolyte, the final pores were irregular with a mean diameter around 35 nm (Figure 1.3*c*). Therefore, the electrolyte was replaced by phosphoric acid, which led to more circular final pores with a mean diameter of 200 nm (Figure 1.3*f*).

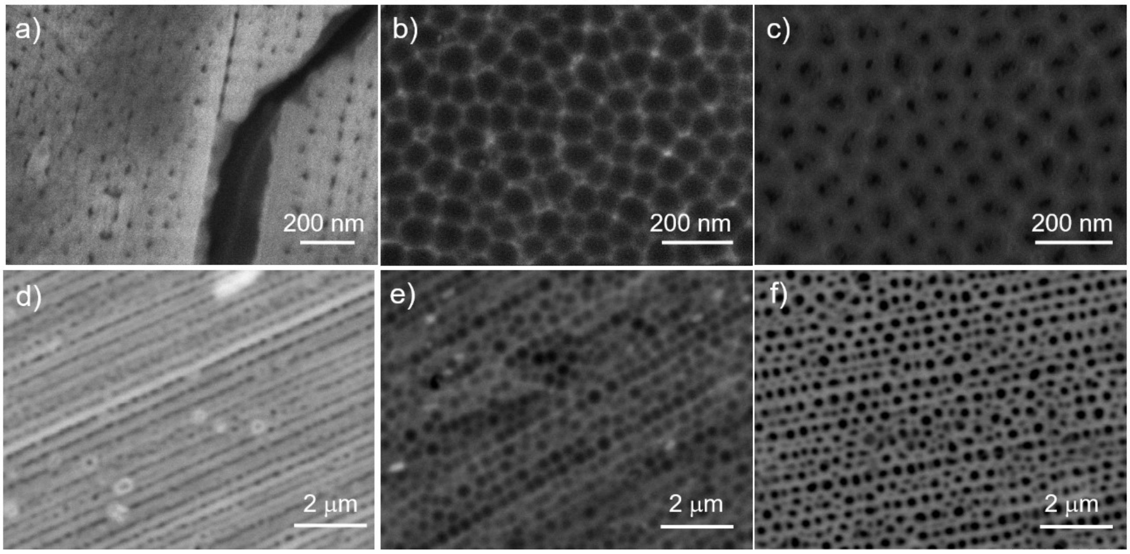

Figure 1.3. Scanning electron micrographs of alumina membrane preparation steps for oxalic acid and phosphoric acid. *a, d*) First anodization. *b, d*) First porous alumina removal. *c, f*) Second anodization.

Despite the improvement of the pores circularity using phosphoric acid, the size distribution was too large to proceed to the next steps. To overcome this problem, we tested different aluminium electrodes, from aluminium wire pressed into a sheet, to commercial aluminium foil, with no success. Eventually, we made use of a general service at the University of Oviedo specialized in the preparation of alumina membranes. Similarly, they used phosphoric acid in the anodization reactions and fabricated the membrane, shown in Figure 1.4, with a mean pore diameter of 470 nm and depth of 700 nm. Then, they performed the steps previous to the deposition of Permalloy: (5) spin-coating of a PMMA layer on top of the membrane, (6) aluminium removal by a mix of copper chloride and hydrochloric acid, (7) breaking of the porous alumina's bottom barrier layer by phosphoric acid, (8) mounting of the porous alumina membrane on a silicon substrate and (9) PMMA removal by acetone.

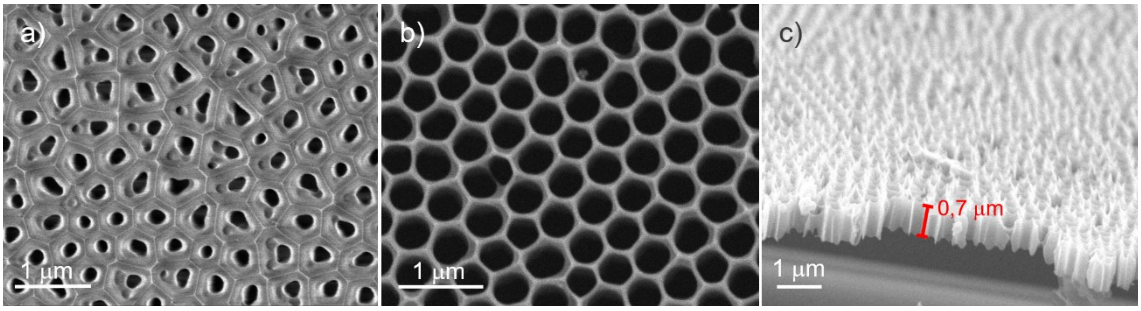

Figure 1.4. Alumina membranes prepared at the University of Oviedo. *a*) First anodization. *b*) Second anodization. *c*) Alumina membrane mounted on a silicon substrate.

Next, 60 nm of Permalloy was deposited (step 10) from a target with nominal composition of $Ni_{80}Fe_{20}$ by DC magnetron sputtering (the fundamentals and specifications of the system are described in Appendix A). The quality of the Permalloy film is of great importance for a good magnetic behaviour. The optimum deposition parameters to obtain extremely soft Permalloy films were determined during previous investigations devoted to developing materials for magnetic sensors [27]. These parameters were used for all of the Permalloy depositions of the present Thesis (Table 1.6 in section 1.1.3).

Lastly, the alumina membrane was removed by ethanol under sonication (step 11). The result of the process is displayed in Figure 1.5. It consists of a dots structure, where the dots are not individually isolated but attached to each other forming a continuous patterned thin film. Only in very few regions, are the dots separated (Figure 1.5*a*).

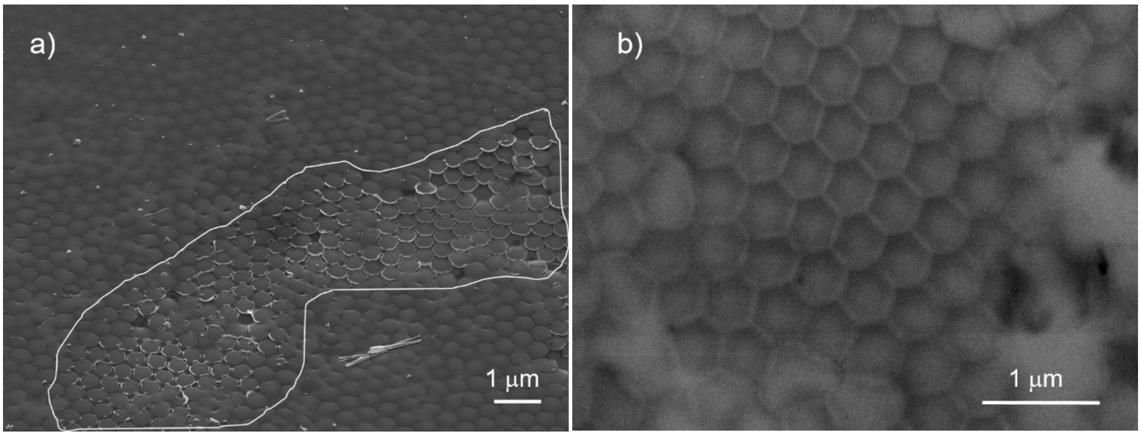

Figure 1.5. SEM images of the final structure of Permalloy prepared by alumina membrane method. *a*) Tilted micrograph where a small region of separated dots is distinguished. *b*) Dots with no separation.

The main reason why there is no separation between the dots is the bad adhesion of the alumina membrane to the silicon substrate, along with the fact that the substrate must be placed upside down in the sputtering chamber. Consequently, the membrane is not sufficiently stuck to the substrate and, during the deposition, Permalloy atoms are able to reach the regions under the pores walls. Clearly, the resolution of this problem and the optimization of the technique required greater efforts. However, at that point, another bottom-up procedure started attracting our attention because of its better suitability for the preparation of nanodiscs down to 100 nm, taking into account our available laboratory resources.

B) Nanosphere lithography (NSL)

Nanosphere lithography uses polymer spheres, typically polystyrene (PS) spheres, that assemble over a surface forming a hexagonal close-packed (HCP) structure, which later acts as template to create arrays of different nanostructures as depicted in Figure 1.6. The fabrication process was structured as follows: (1) PS spheres assembly on a thin film, (2) PS spheres size reduction by oxygen ion plasma, (3) etching of the non-protected thin-film by ion plasma, (spheres removal) and (4) PS spheres removal. Permalloy can be sputtered either at the beginning of the procedure, *i.e.*, before the assembly of the PS spheres (Figure 1.6*a*), or at the end, after the removal of the spheres (Figure 1.6*b*).

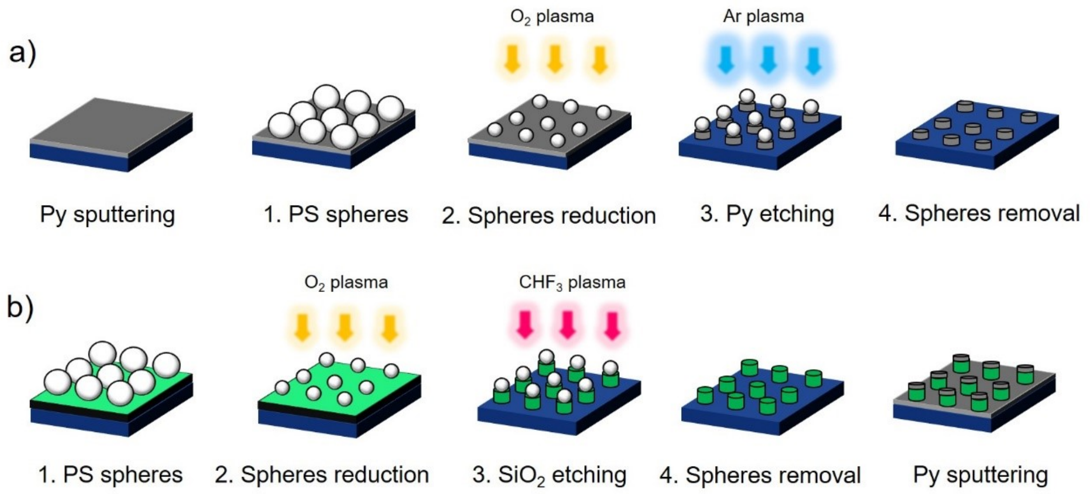

Figure 1.6. Flow diagram of the NSL modified to produce Permalloy discs. Permalloy can be deposited either before the assembly of the PS spheres (*a*) or after the removal of the PS spheres (*b*).

The next paragraph gives a brief description of the polystyrene spheres synthesis. Then, we will focus on the experimental details and the results of each step: note that all the steps but the third (etching of the non-protected layer) are the same for both routes (*a* and *b*).

The polystyrene spheres were synthetized by dropwise method [28, 29] in the Laboratory of Macromolecular Chemistry at the University of the Basque Country. Briefly, the stabilizer (polyvinylpyrrolidone, PVP) was dissolved in the reaction medium (ethanol) in a round-bottomed flask and the solution formed by the monomer (styrene) and the polymerisation initiator (azobisisobutyronitrile, AIBN) was added dropwise. The flask was immersed in an oil bath (70 °C) under a constant stirring and was connected to a reflux condenser, to avoid the evaporation of the ethanol, and to a nitrogen-filled balloon. The experimental set-up is shown in Figure 1.7. The polymerisation reaction lasted 24 h. Next, the solution was centrifuged (4000 rpm, 20 min), decanted and re-dispersed in ethanol three times to remove the residual styrene and PVP. Lastly, the solution was drained in vacuum. The stabilizer quantity and the monomer-initiator addition rate are crucial for the control of the size and the size distribution of the final polystyrene spheres. Using a PVP content of 20 % by weight of the styrene and an addition rate of 100 μl/s, we obtained spheres with a mean diameter of 2.5 μm and a standard deviation of 0.3 μm.

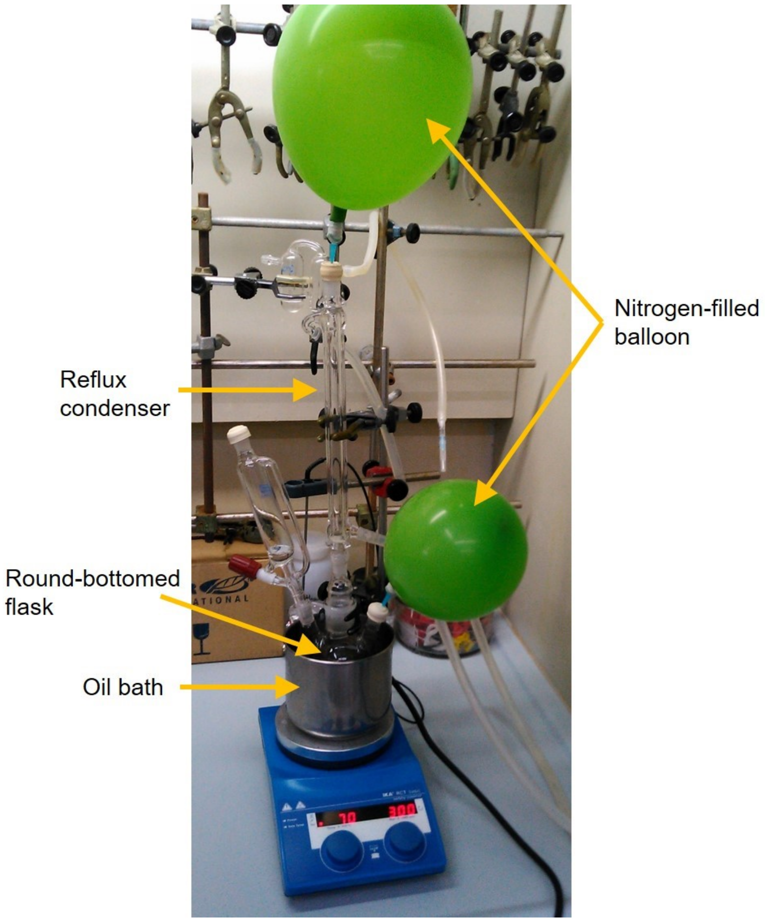

Figure 1.7. Experimental set-up for the synthesis of polystyrene spheres.

The assembly of the PS spheres on the substrate was carried out through different coating techniques: dip-coating, drop-coating and spin-coating.

The *dip-coating* technique is based on the direct assembly of PS spheres at the air–water interface [30]. The aqueous colloidal suspension (10 wt.%) was diluted with ethanol to form a 50 vol.% mixture of dispersion and applied to the water surface via a partially immersed hydrophilic glass slide with at a tilt angle of approximately 45° with respect to the water surface. To help the direct crystallization process, small amounts of surfactant (Triton X-100) were added to the water phase prior spreading of the colloids. The monolayer readily formed at the air–water interface. A hydrophilic substrate (silicon wafer) was immersed into the subphase and elevated under a shallow angle to transfer the monolayer. The substrate was dried on a hot-plate at 80 °C. Figure 1.8 schematically presents the dip-coating procedure.

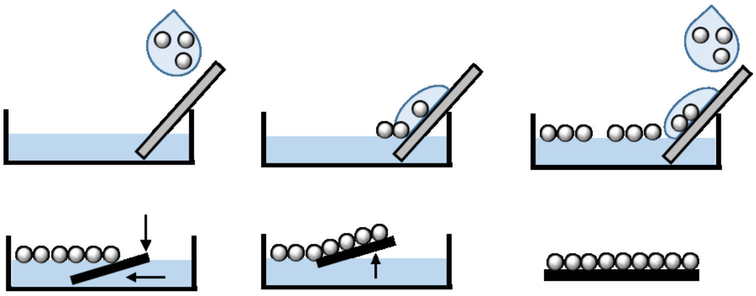

Figure 1.8. Flow diagram of dip-coating procedure.

In the *drop-coating* method, the aqueous colloidal suspension (10 wt.%) was diluted with ethanol to form a 50 vol.% mixture of dispersion and Triton X-100 was added (in 1:400 by volume ratio respect to the ethanol). An aliquot of this suspension was drop-coated onto the substrate and allowed to dry. Ideally, the spheres self-assembled to form a HCP monolayer [31] as schematized in the Figure 1.9.

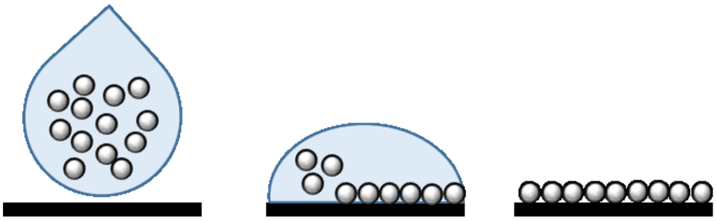

Figure 1.9. Flow diagram of drop-coating procedure.

In the *spin-coating* technique, the aqueous colloidal suspension (10 wt.%) was diluted with ethanol to form an 8:1 volume ratio dispersion. An aliquot of this suspension was spin-coated on the samples. The spin-coating program consisted of three stages: (*i*) 400 rpm for 10 s to spread the beads solution evenly; (*ii*) 800 rpm for 2 min to spin away the excess bead solution; (*iii*) 1400 rpm for 10 s to spin off the excess materials from the edges [12]. Figure 1.10 is a schematic description of the spin-coating procedure to obtain monolayers of PS spheres.

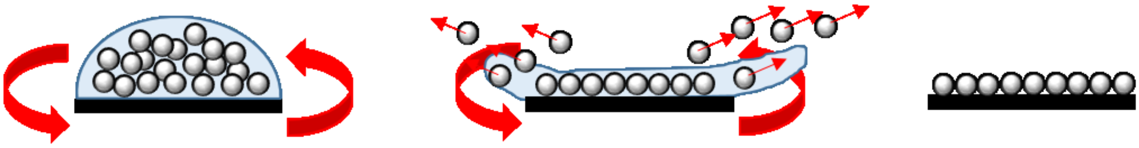

Figure 1.10. Flow diagram of spin-coating procedure.

In the three coating techniques, the surface tension plays a key role. As mentioned above, in the case of the dip- and drop-coating, the use of a surfactant

(Triton X-100) was necessary to control the surface tension. However, inappreciable variations in the concentration of the surfactant led to huge changes in the PS spheres arrangement. Moreover, in the particular case of the dip-coating, the hydrophilicity of the substrate resulted to be especially crucial which, despite using the same surface treatment procedure, was almost impossible to control because of its dependence on more factors, such as ambient humidity and water purity. In the case of the drop-coating, the amount of PS spheres in the drop was also critical and, in most of the cases, we were not able to avoid the particles excess, causing the formation of multilayers. In the case of the spin-coating instead, the centrifugal force helps spreading the PS spheres without the addition of surfactants, while it spins away the excess of particles. Therefore, after optimizing the parameters (rotational speed, duration of each step and concentration of PS beads), the spin-coating appeared to be the most controllable and reproducible technique and the majority of the samples were prepared through it, being the obtained monolayer areas in the order of hundreds of μm^2, as shown in Figure 1.11.

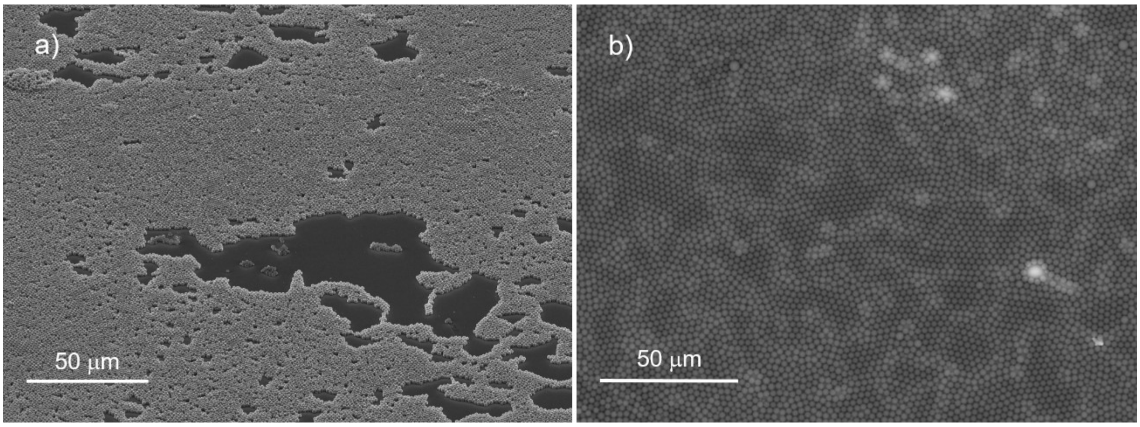

Figure 1.11. Close packed hexagonal arrays of PS spheres. *a*) Tilted micrograph. *b*) Top view.

After the formation of the HCP arrays, the spheres were reduced in size by means of oxygen ion plasma in a reactive ion etching (RIE) system. The fundamentals and specifications of the system are described in Appendix A. The reduction of PS spheres was performed through a combustion reaction between the oxygen ions and polystyrene, producing carbon dioxide and water. The optimized parameters of the dry etching are collected in Table 1.2. The reduction in diameter is about 300-400 nm, and the etching can be repeated several times to reduce the bead size almost to the half, as shown in Figure 1.12.

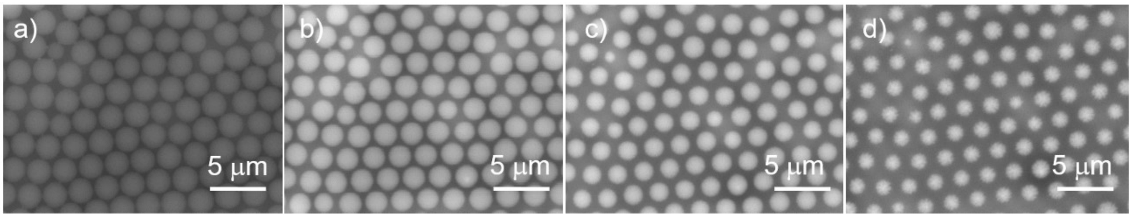

Figure 1.12. PS spheres size reduction by oxygen plasma etching. *a*) PS spheres before etching with a mean diameter of 2.5 μm. *b*) After 1 min etching. *c*) After 2 min etching. *d*) After 3 min etching with a mean diameter of 1.5 μm.

After 3 min of etching, the ion bombardment also affects the shape of the PS beads, losing its sphericity (Figure 1.13). Nevertheless, as the circular base is conserved, they still work as protecting masks for the next step: ion plasma etching of the bottom thin film that, as explained before, can be Permalloy itself or a sacrificial layer, such as silicon oxide.

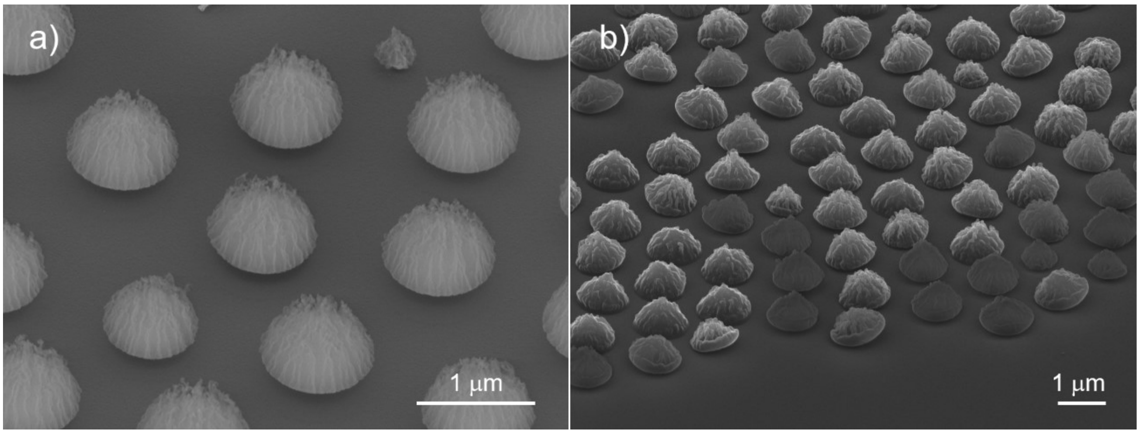

Figure 1.13. PS spheres after 3 min of oxygen plasma etching.

In the first case (illustrated in Figure 1.6*a*), 60 nm of Permalloy were sputtered on a silicon substrate and, afterwards, the PS spheres were deposited and reduced in size. The etching of the exposed Permalloy thin film was performed by argon ion milling which is a pure mechanical etching due to its chemical inertness. The parameters of the etching had to be optimized one-by-one in order to obtain an isotropic etching of Permalloy while not damaging the circularity of the PS spheres (Table 1.2). At the end, PS spheres are removed by tetrahydrofuran. The optimization of the parameters can be observed in the Figure 1.14, where the circularity of the Permalloy structure is improved from Figure 1.14*a* to 1.14*c*.

Table 1.2. Reactive ion etching parameters used in nanosphere lithography.

Etching process	Gas flux (sccm)	Pressure (mTorr)	Power (W)	Time (min)
PS bead reduction	O_2: 12, Ar: 5	100	100	1
Permalloy milling	Ar: 15-100	10-100	50-200	5-60
Silicon oxide etching	CHF_3: 10	20	50	20

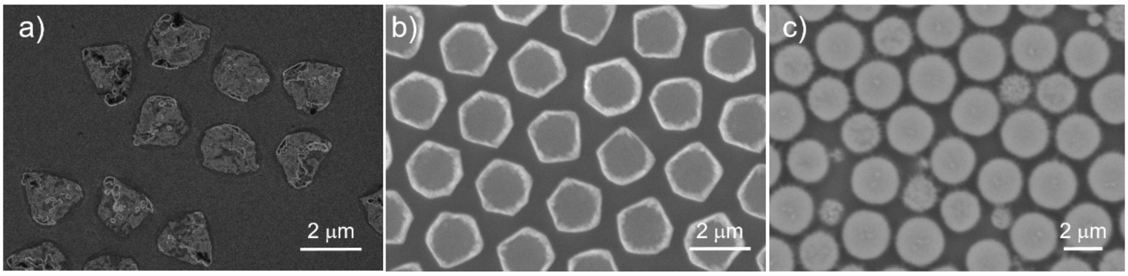

Figure 1.14. Permalloy dots after PS spheres removal. The Permalloy etching parameters are different. *a*) 100 sccm Ar, 100 mTorr, 200 W, 5 min. *b*) 15 sccm Ar, 10 mTorr, 100 W, 20 min. *c*) 15 sccm Ar, 10 mTorr, 50 W, 60 min.

In the second case (illustrated in Figure 1.6*b*), we made use of the 400 nm thick thermal oxide grown on top of the silicon wafers (manufactured by Si-Mat). After the deposition and reduction of the PS spheres, the non-protected silicon oxide was sculpted using fluoroform plasma, which reacts as follows [32]:

$2CHF_2^+ + SiO_2 \rightarrow 2CO + H_2 + SiF_4$

For this approach, apart from the homemade PS spheres, commercial spheres down to 0.5 μm were used. The obtained silicon oxide pillars are shown in the Figure 1.15. The following steps would be Permalloy sputtering and removal of the silicon oxide pillars to release the discs. However, we did not performed them due to two main reasons: first, the magnetic characterization of the discs on-substrate is not possible since the sample would behave as a continuum Permalloy thin film, and second, the difficulty of chemically etching the silicon oxide.

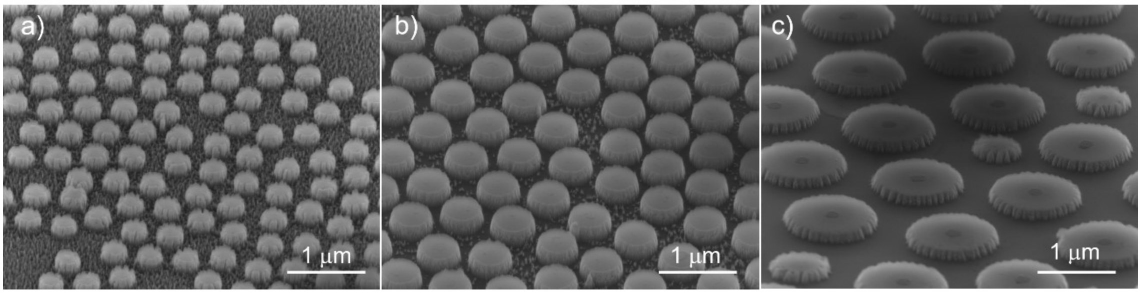

Figure 1.15. Silicon oxide pillars obtained from PS spheres of different sizes. *a*) PS spheres of 0.5 μm. *b*) PS spheres of 0.7 μm. *c*) PS spheres of 2 μm.

While we were immersed in the optimization of the NSL, a novel technique, named hole-mask colloidal lithography (HCL), drew our attention. HCL is actually a variant of NSL with the difference that it uses surface charged polystyrene spheres. In principle, HCL could solve the main problem hindering the NSL that is the difficulty of creating monolayers over large areas. Thus, we focused our efforts on preparing Permalloy nanodiscs through HCL.

1.1.2. Hole-mask colloidal lithography (HCL)

The HCL fabrication process involves three main stages: (*i*) formation of a short-range-ordered polystyrene (PS) nanoparticles array onto a polymeric layer, (*ii*) transfer of the self-assembled PS pattern to a sputtered titanium thin film that is used as a mask to etch the holes in the polymeric layer, and (*iii*) fabrication of nanodiscs by sputtering Permalloy within the nanoholes, followed by the removal of the polymeric layer. The complete process flow is schematized in Figure 1.16, detailing the successive fabrication steps.

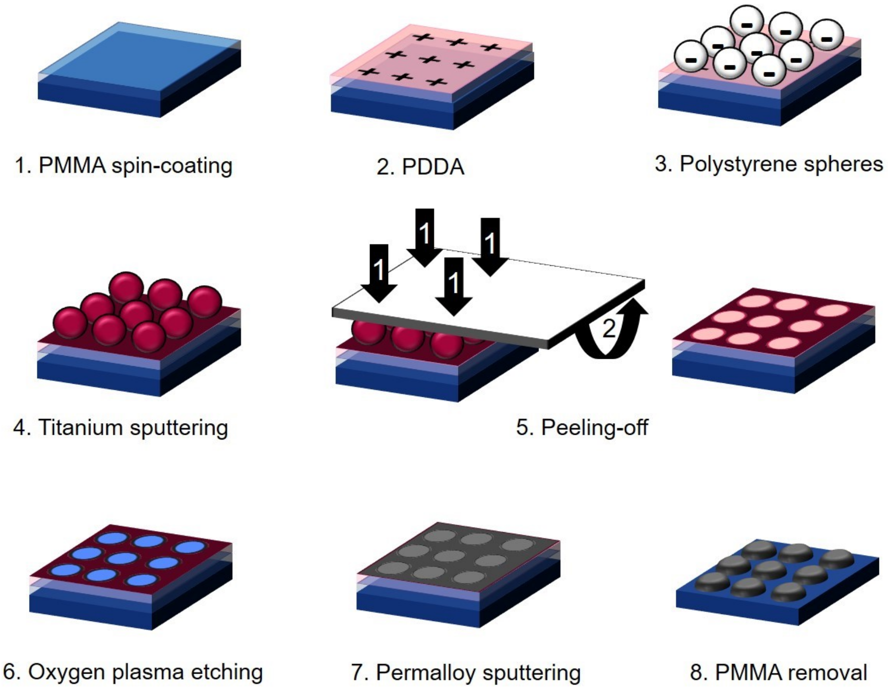

Figure 1.16. Schematized description of the process steps for fabricating Permalloy nanodiscs with magnetic vortex state by hole-mask colloidal lithography.

(1) PMMA spin coating

Silicon wafers with a 400 nm thick SiO_2 layer on top were used as substrates. Polymethyl methacrylate with 495.000 molecular weight diluted in anisole (PMMA

495 A2) was purchased from MicroChem. Before the spin coating, the substrate was cleaned by a standard approach: the substrate is submerged in acetone for 3 min under ultra-sonication and then dried with nitrogen air. The process is repeated using isopropanol and de-ionized (DI) water.

The PMMA was deposited by spin-coating onto the substrate. Several tests needed to be done to achieve a uniform PMMA thin film with the desired thickness, 100 nm. The final spin-coating program consists of three stages: (*i*) 500 rpm for 5 s to spread the PMMA solution evenly; (*ii*) 1000 rpm for 45 s to obtain a uniform PMMA layer of 100 nm (according to the spin speed curve from PMMA MicroChem specifications); (*iii*) 300 rpm for 5 s to deaccelerate.

The PMMA layer was afterwards pre-baked on a hot plate at 180 °C for 90 s to evaporate the solvent.

(2) Surface treatment

The hydrophobicity of PMMA must be reduced to avoid spontaneous de-wetting of the surface during subsequent polyelectrolyte and particle deposition steps, which would introduce inhomogeneities in the particle distribution. To do that, the surface was treated with an oxygen plasma by RIE (see Table 1.3). The incorporation of oxygen to the surface leads to the increase of oxygen containing groups, like C-O bond and ester binding (O=C-O), and the formation of new functional groups like carbonyl (C=O). Consequently, the hydrophilicity of the PMMA surface increases significantly [33].

Table 1.3. Reactive ion etching parameters used in hole-mask colloidal lithography.

Etching process	Gas flux (sccm)	Pressure (mTorr)	Power (W)	Time
Hydrophobicity reduction	O_2: 30, Ar: 3	25	5	5 s
PMMA etching	O_2: 30, Ar: 3	25	50	4 min

Next, the PMMA film was charged positively through the incubation of a solution of poly-diallyldimethylammonium chloride (PDDA), with 200.000-350.000 molecular weight, 0.2 wt.% in Milli-Q water (Sigma Aldrich). PDDA is a strongly cationic polyelectrolyte that easily dissociates in aqueous solutions. The incubation consists of applying a drop of PDDA on the treated PMMA film, for 1 min, so the PDDA can bind to the functional groups of the PMMA surface (Figure 1.18). Then the sample was carefully rinsed with DI water to remove the excess of PDDA. Finally, the surface was dried in a low-pressure nitrogen flow, resulting in a PMMA film with sparsely distributed positive charges.

Figure 1.18. Incubation of PDDA on a hydrophilic PMMA film.

(3) Charged PS spheres assembly

A drop of 0.2 wt.% solution containing the negatively charged polystyrene nanospheres was dispensed over the surface and incubated in the same manner as the PDDA (Figure 1.19). We used commercial nanospheres (Life Technologies) with nominal size of 100 nm for the fabrication of sub-100 nm discs (the reduction of the size from the sphere to the final disc is further explained). In the same manner, we used nanospheres with nominal size of 200 nm to prepare discs with diameter above 100 nm, which are expected to present a clear vortex configuration for a wider range of thicknesses, and are included in the study to help understanding the behaviour of the discs with smaller size. The nanospheres are stabilized with sulphate anions. Each PS nanosphere is bonded to 500 and 7000 sulphate anions per particle of 100 nm and 200 nm respectively, resulting in a surface charge density of hundreds of nC/cm^2. Electrostatic repulsion between the colloids and attraction between the colloids and the surface defines a short-range-ordered PS nanoparticle array. Nevertheless, in the case of 200 nm spheres, the capillarity forces are similar to electrostatic forces, thus the nanospheres tend to aggregate. The Figures 1.20*a* and 1.20*b* show SEM images of the nanospheres attached onto the PMMA layer after this step.

Figure 1.19. Incubation of PS spheres on the positively charged PMMA thin film.

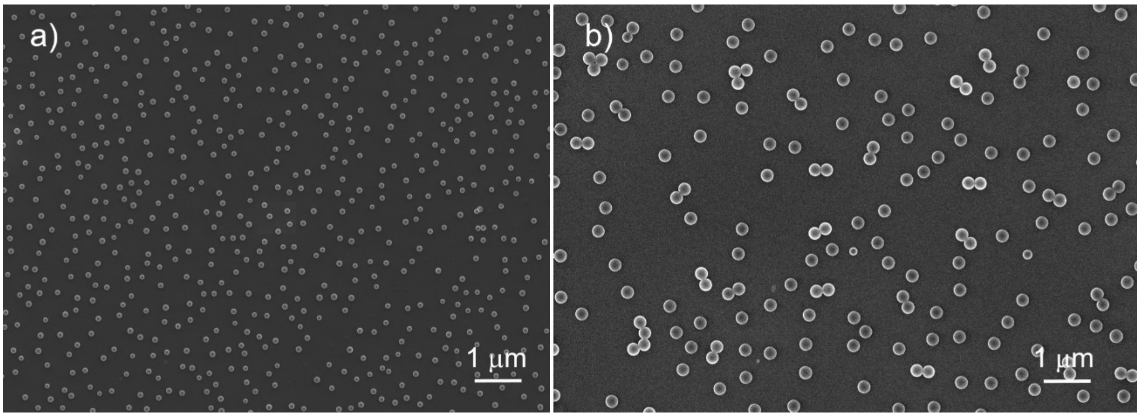

Figure 1.20. PS nanospheres with sulphate groups distributed over the PMMA layer. *a*) 100 nm spheres in a short-range-ordered array. *b*) 200 nm spheres, small aggregates are observed.

(4) Deposition of the hard mask

A thin film, resistant to oxygen plasma, was sputtered on top of the PS spheres and PMMA, which would act as the hard mask in the following steps. In a first attempt, a 20 nm thick chromium (Cr) layer was used for that purpose. Nevertheless, the surface roughness of the Cr hindered the fifth step, so it was replaced by titanium (15 nm). The DC magnetron sputtering conditions are collected in Table 1.6.

(5) PS spheres peeling-off

The mechanical removal of the spheres (and the metal deposited on top of them) was performed through an adhesive tape. The selection of the adhesive is critical; the adhesion force must be high enough to peel the spheres off, but low enough not to remove the whole metal thin film. The appropriate adhesion force value resulted to be around 100 g/25 mm (180° peel angle). We used a blue adhesive polyvinyl chloride (PVC) film 1008R (Semiconductor Production Systems, SPS), with 95 g/25 mm adhesion force. The adhesive was applied on the sample by means of a cotton swab making increasingly bigger circles from the centre to the edges of the sample, with a constant pressure enough to attach the film.

In the case of the sample covered with chromium, due to its high roughness, the force needed to adhere the PVC film to the surface was relatively large. Indeed, the roughness hinders the adherence between the surfaces [34]. Thus, the force applied to adhere the PVC film to the top PS spheres, resulted high enough to detach the Cr thin film below as well. In short, the PVC film either detached the whole Cr thin film (including the PS spheres) or did not detach anything.

In the case of the sample covered with titanium, thanks to its low roughness, a low-pressure force was effective to detach only the nanospheres and the titanium deposited on top of them, revealing the holes through which PMMA is exposed. The peel angle was 180°. Figure 1.21 shows an image of a sample, after the peeling-off step, next to the PVC film where a shadow corresponding to the detached nanospheres can be observed.

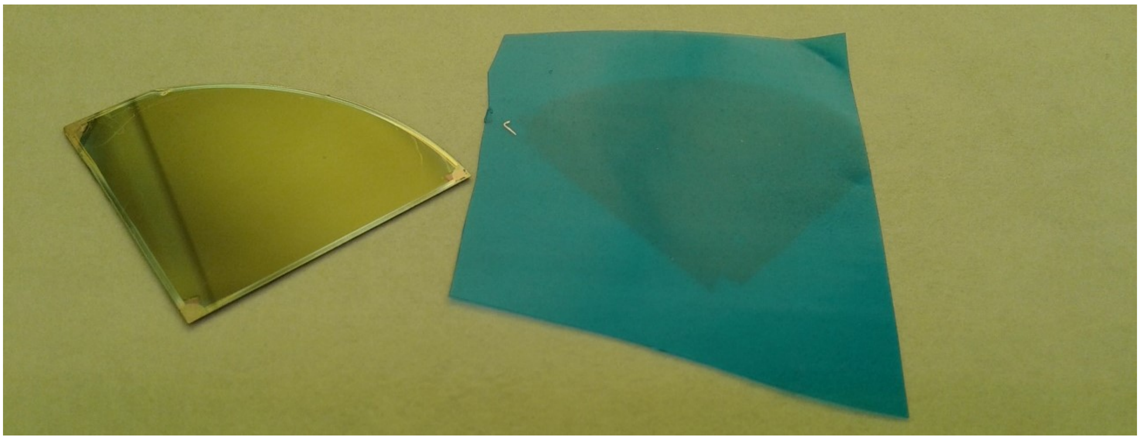

Figure 1.21. Peeling-off process. On the right, PVC film with detached PS nanospheres and the titanium deposited on top of them. On the left, the sample after the peeling-off step which now consists on a PMMA layer covered with a hole patterned titanium hard mask.

(6) PMMA dry etching

Once the PS spheres were removed and the holes were revealed in the titanium thin film, the non-protected PMMA was etched in oxygen plasma. The mechanism of PMMA etching is a standard combustion reaction, the same as in the PS spheres size reduction step (conditions in Table 1.3). The reaction lasts 4 min, which was the calibrated time necessary to remove a 100 nm thick PMMA layer, completing the creation of the hole-mask. Figure 1.22*a* shows an image of the surface after this step. Figure 1.22*b* reveals that the hole diameter is smaller than the sphere diameter.

Obviously, the contact area of the PS sphere with the PMMA is smaller than 100 nm, therefore, the titanium atoms also reach regions under the sphere during the sputtering.

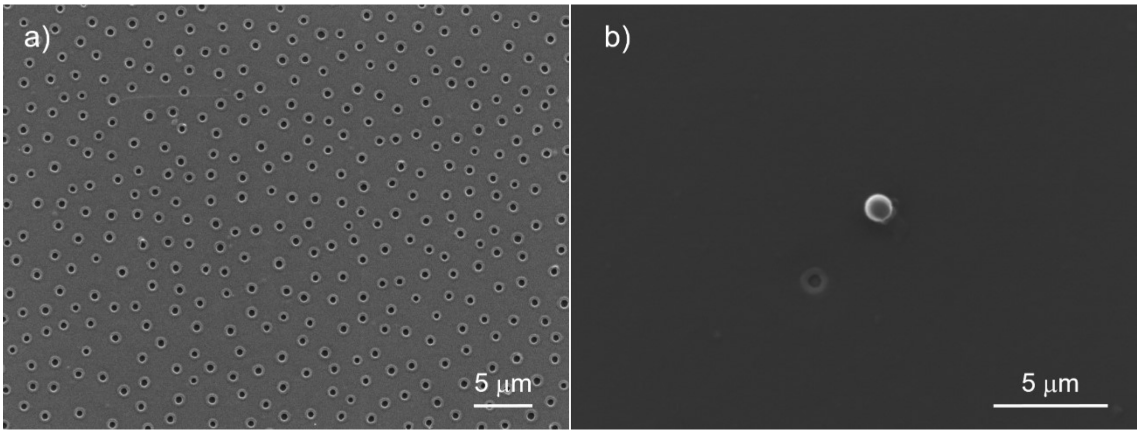

Figure 1.22. Titanium hole-mask after removal of 100 nm PS spheres and PMMA etching in oxygen plasma. *a*) Top view of the holes. *b*) Titanium film with a hole and a remaining PS sphere.

(7) Permalloy sputtering

Permalloy was sputtered within the patterned nano-holes. For the further assessment of the region of vortex stability in sub-100 nm discs, different deposition times were selected to produce discs with thicknesses in the range of 20 to 50 nm. In the case of the larger discs fabricated from the spheres of 200 nm in diameter, we selected two thicknesses where the vortex should be stable (30 and 50 nm) to ease the understanding of the magnetic behaviour of the smaller discs.

For the biomedical tests, few nanometres of gold were sputtered to form a gold-Permalloy-gold sandwich structure (Table 1.6). Gold serves as biocompatible covering and provides a substrate for easy surface modification of the discs with cancer-targeting ligands.

(8) Lift-off

Finally, PMMA was removed by chemical etching, lifting off the titanium mask and defining the fabricated nanodiscs over the substrate surface. The PMMA, after being baked at high temperature, was strongly adhered to the substrate surface. Hence, the standard acetone lift-off process was not sufficient and a final oxygen plasma ashing was needed. Our lift-off procedure involves three stages: (*i*) 2 h in acetone, (*ii*) 1 min under ultra-sonication (US) in the same solvent, (*iii*) 1 min in isopropanol under US, (*iv*) 1 min in DI water under US and (*v*) 10 min of oxygen plasma by RIE.

Figure 1.23 shows sets of nanodiscs fabricated from PS spheres of 100 nm and 200 nm, with thicknesses from 30 to 50 nm.

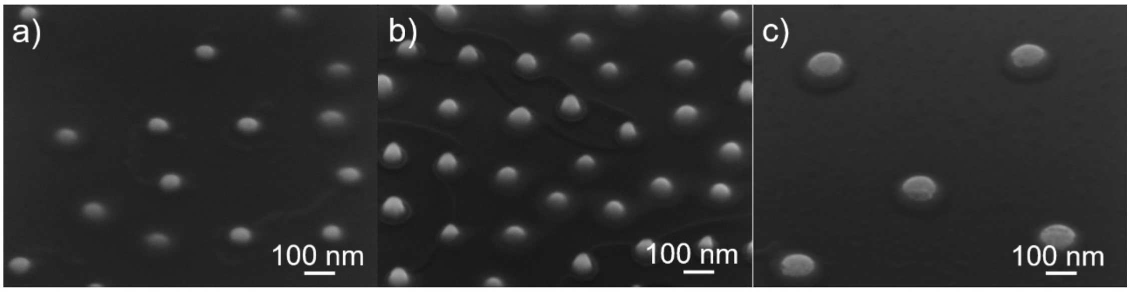

Figure 1.23. Tilted view of the Permalloy nanodiscs fabricated by hole-mask colloidal lithography. Sub-100 nm discs with (*a*) 30 nm and (*b*) 50 nm in thickness. *c*) Sub-200 nm discs with 30 nm in thickness.

The size distributions were established by image analysis using ImageJ software [35]. The mean diameter of the discs resulted to be about 30 % less than the original diameter of the PS beads: the spheres of 100 nm lead to discs with 60 or 70 nm in diameter (we used two different batches of PS beads) (Figures 1.24*a* and 1.24*b*), whereas the 200 nm spheres resulted in discs with 145 nm in diameter (Figure 1.24*c*). This scale-down can be attributed to shadow effects (lack of perfect directionality) during the sputtering of the Ti mask and the deposition of the Permalloy. On the one hand, as pointed before, the final hole dimension is defined by the PS sphere area that is in contact with the PMMA, which leads to a significant reduction in diameter. On the other hand, the sputtering in holes of such small dimensions results rather challenging due to the shadow effect of the hole walls. Consequently, the nanodisc base diameter results reduced and, more importantly, the surface of the disc becomes slightly dome-shaped. This effect is accentuated when increasing the disc thickness (50 nm) but is almost negligible in the case of thinner discs (below 30 nm). In any case, the dome-shape insignificantly affects the magnetic configuration, as it will be discussed in the following chapter.

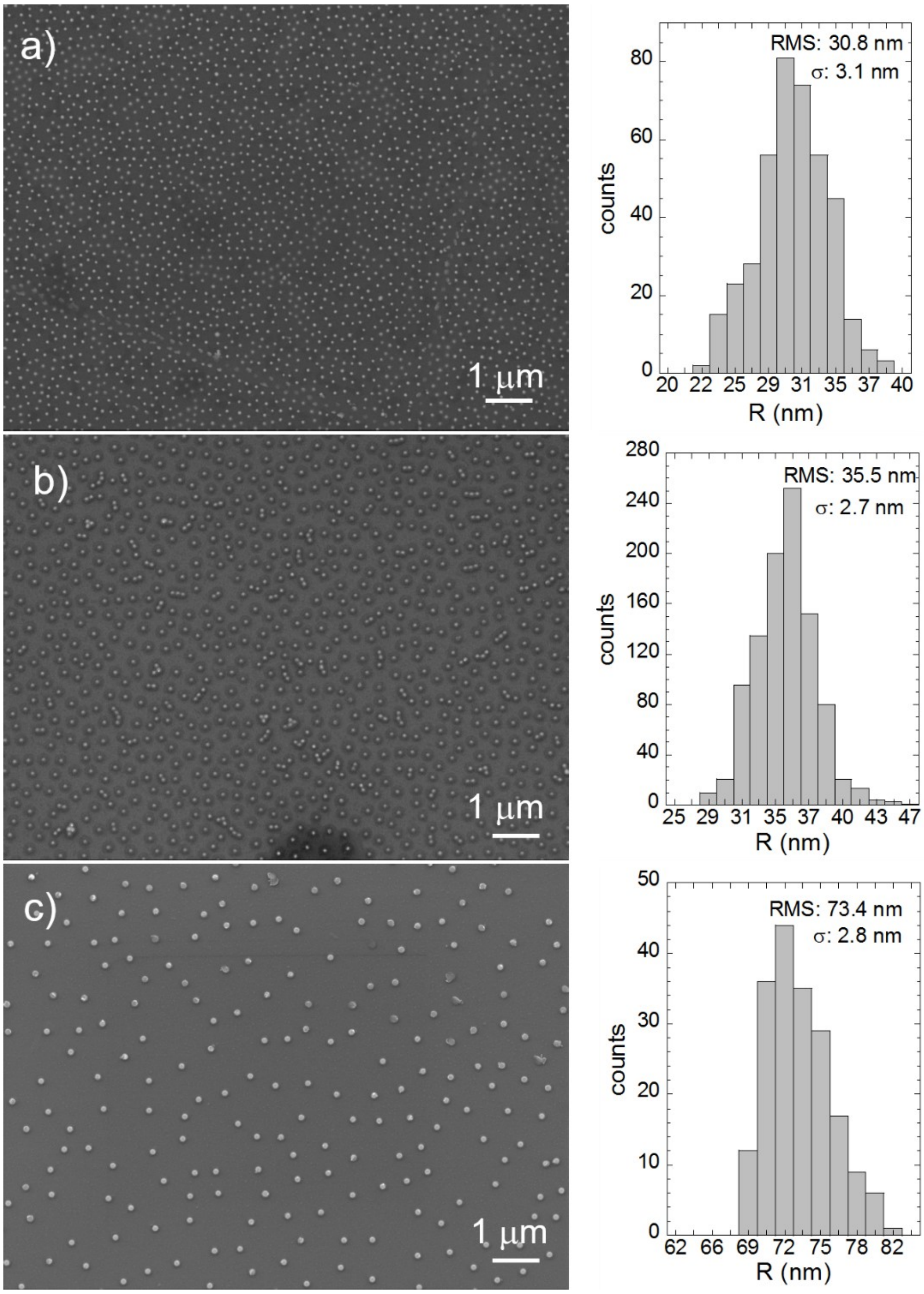

Figure 1.24. Size distributions of the Permalloy nanodiscs fabricated by HCL from spheres of 100 nm diameter (*a, b*) and 200 nm diameter (*c*).

The thickness of the discs (*T*) was accurately determined by atomic force microscopy (see Appendix A). The lateral resolution of the atomic force microscopy (AFM) is rather poor due to the convolution effect caused by the tip finite size. An AFM standard (composed of steps 20 nm high) was used to quantify the magnitude of this effect, which results to be about 75 nm as shown in Figure 1.25.

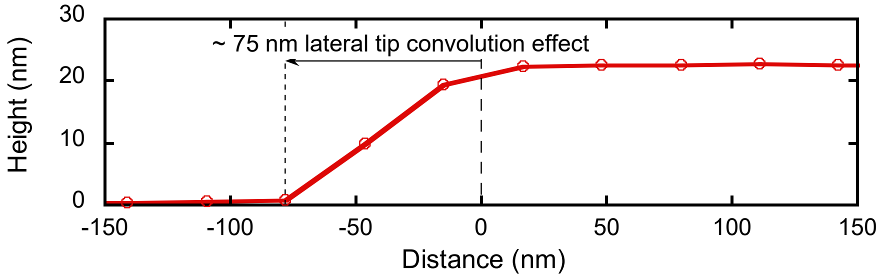

Figure 1.25. Quantification of the magnitude of the tip convolution effect in AFM measurements. The “rising” slanted profile caused by this effect in a 20 nm high calibration standard, measured in the same conditions that the samples, is about 75 nm long.

Considering the convolution effect, the lateral dimensions measured by AFM agree with the ones measured by SEM as can be observed in the profiles shown in Figure 1.26.

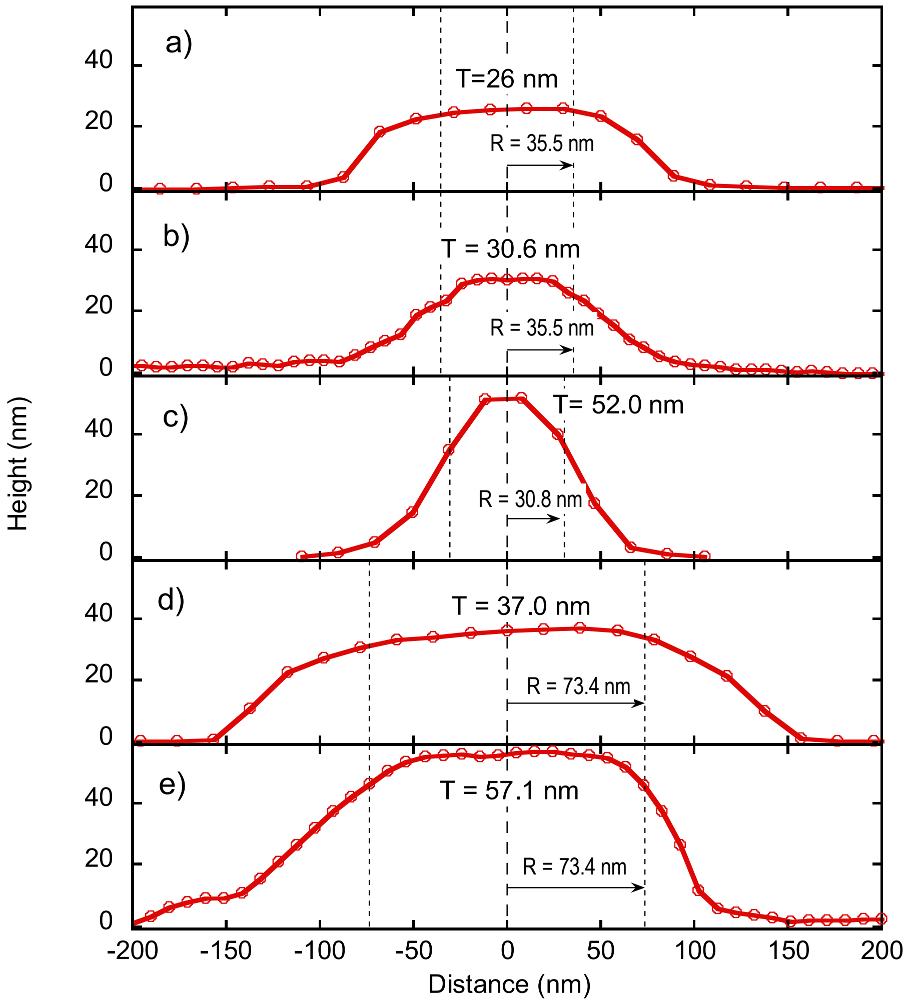

Figure 1.26. Profiles obtained from AFM measurements for the nanodiscs having nominal thicknesses of 20 nm (*a*), 30 nm (*b, d*) and 50 nm (*c, e*). All the samples but the *c*, have a capping Au layer of 3-4 nm.

After the preparation and morphological characterization of a large amount of samples (over 170 samples were prepared in almost 80 batches), we made a selection of five sets that are thoroughly studied in the following chapter. The main criteria of selection were two: (1) the expected magnetic relevance based on the diameter to thickness aspect ratio and (2) the quality of the samples, *i.e.*, high density of nanodiscs over the substrate with a constant interdot distance and with no Permalloy "islands". Table 1.5 collects the relevant morphological data of the five nanostructures and identifies them with abbreviations to ease their references in the next chapters.

Table 1.5. Identification and morphological data (R = radius, T = thickness) of the Permalloy discs.

Sample label	**Abbreviation**	**Nominal size**		**Real size**[1]	
		***R* (nm)**	***T* (nm)**	***R* (nm)**	***T* (nm)**
Small-20	S-20	30	20	35 ± 3	22 ± 1
Small-30	S-30	30	30	35 ± 3	28 ± 1
Small-50	S-50	30	50	31 ± 3	52 ± 1
Large-30	L-30	70	30	73 ± 3	33 ± 1
Large-50	L-50	70	50	73 ± 3	53 ± 3

[1] Uncertainty in R corresponds to the standard deviation σ of the size distribution. The uncertainty in T is an estimated upper limit.

For the experiments with cells taking place after the study of the magnetic behaviour, the nanodiscs must be released from the substrate. Although we had not seen any previous report on it, the HCL fabrication method can be easily adapted to allow releasing the prepared nanostructures.

1.1.3. Nanodiscs release

The strategy in mind was to use a sacrificial layer that could be selectively etched after the patterning process, freeing the nanostructures fabricated on top of it. Four alternative procedures were tested for that purpose.

a) NaCl substrate

Sodium chloride (NaCl) round substrates (25 mm diameter, 4 mm thickness) were purchased in Sigma Aldrich. The PMMA was spin coated in the same manner as described above. The further steps involve the use of water to rinse the excess of PDDA and PS spheres. In order to avoid the dissolution of the salt wafer and facilitate its manipulation, it was protected by the PVC film as shown in Figure 1.27. However, during the PDDA rinsing, the water partially dissolved the exposed salt wafer face, revealing the poor impermeability of the PMMA layer.

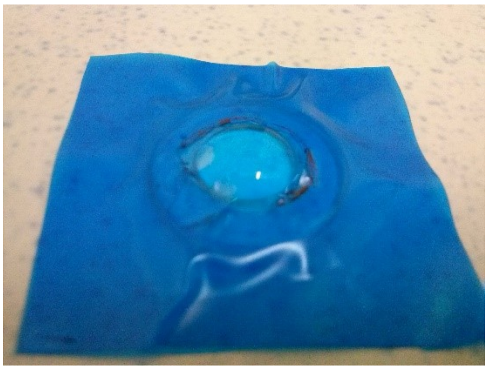

Figure 1.27. NaCl substrate partially protected by the PVC film, the PMMA face remains uncovered.

In the second attempt, the wafer was placed facing down during the PDDA excess water rinse, expecting that the gravity would not allow the water to reach the substrate, but it did. Hence, we decided to replace the water by cyclohexane, which neither dissolves the salt nor the PMMA. However, during the incubation of PS spheres, we saw how pieces of PMMA layer were detaching from the NaCl substrate until they reached the surface of the drop; the cyclohexane reduced the adherence between the NaCl substrate and the PMMA layer. In any case, we later knew that the cyclohexane is not a suitable rinse solvent as it is non-polar and cannot deal with the electrostatic forces taking place in the colloidal lithography. Water was excluded as rinse polar solvent, but other common polar solvents like acetone, isopropanol, ethanol or methanol would etch the PMMA. A more chemically resistant substrate was needed.

b) Glass substrate

Soda lime glass (Corning glass slides) were used as the second candidate for nanodiscs release. Its chemical composition is as follows: SiO_2 73 %, Na_2O 14 %, CaO 7 %, MgO 4 %, AlO_3 2 %. Hydrofluoric acid (HF) is known to dissolve many materials, especially oxides and, so, glass [36]. Nevertheless, it is also a highly corrosive solution capable of etching Permalloy as well. Therefore, Permalloy structures must be protected by an inert thin film, *e.g.*, gold. In order to determine the etching conditions, first, millimetre-sized structures (50 nm Au-200 nm $Fe_{20}Ni_{80}$-50 nm Au) were patterned on the glass substrates by photolithography (see Figure 1.28*a*). HF 48 vol.% was diluted in water forming a 50 vol.% mixture. After several tests, the etching rate resulted to be around 10 μm/min and the patterned sandwich structures were released as shown in Figure 1.28*b*. Moreover, the gold layers seemed to protect the Permalloy efficiently as the structure was attracted by a permanent magnet after the etching (Figure 1.28*c*).

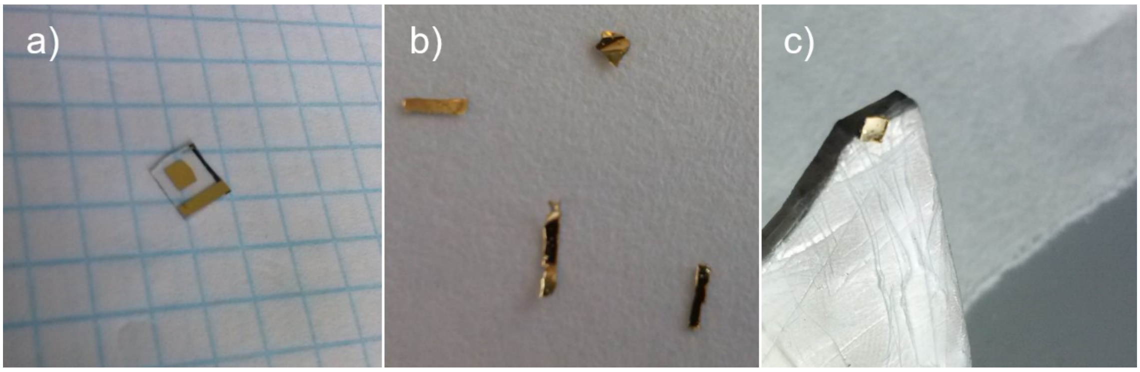

Figure 1.28. Gold-Permalloy-gold structured thin films fabricated by photolithography on the soda lime glass substrate. *a*) Before the etching. *b*) Au-FeNi-Au structures released from the substrate. *c*) Au-FeNi-Au structure released from the substrate and attracted to a permanent magnet.

The glass-HF release procedure was considered promising, at least, at the macroscale (the length of the patterned structure was around 2 mm). Nevertheless, at the nanoscale, the effect of the HF on the sides of the Permalloy discs that remain exposed could be great enough to damage the nanostructure. In order to study the effect of the etchant on the non-protected Permalloy, we decided to fabricate discs at the microscale. In that way, the size of the structure was reduced by three orders of magnitude, getting closer to the nanodiscs, whereas the tracking of the etching process would be immediate, as there was no need of applying for high-resolution microscopy. The discs 10 μm in diameter were fabricated by photolithography (the procedure is described in detail in the section 1.2.1).

The microdiscs (10 nm Au - 180 nm Permalloy - 10 nm Au) were fabricated on a silicon wafer covered with 400 nm of silicon oxide that can be also etched in hydrofluoric acid (HF). Then, the non-protected silicon oxide was etched in a CHF_3 plasma by RIE using the recipe presented in Table 1.2. Figure 1.29 shows a Permalloy microdisc, covered with gold, prior and posterior to the dry etching.

According to AFM measurements, 200 nm of silicon oxide were removed. In that way, it was expected that the HF would easily etch the silicon oxide under the discs releasing them more rapidly. Nevertheless, 1 h of wet etching in HF:H_2O (1:10) resulted not to be sufficient to release the discs, furthermore, most of them seemed to be damaged as shown in Figure 1.29*c*.

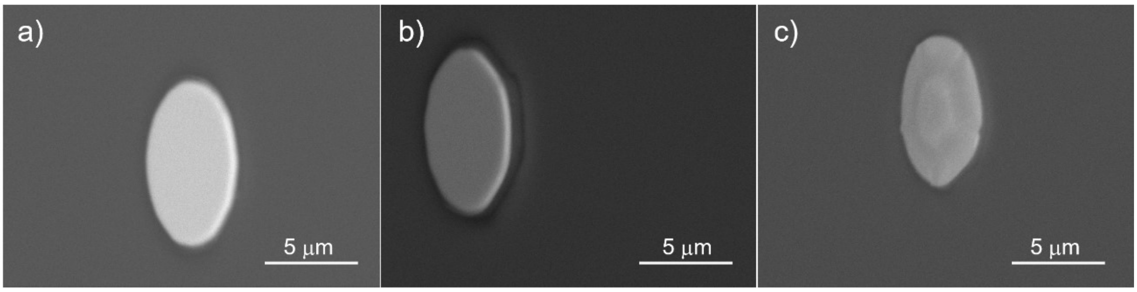

Figure 1.29. Gold-Permalloy-gold microdisc (*a*) before and (*b*) after silicon oxide etching in CHF_3 plasma and (*c*) after wet etching in HF.

Besides the negative results obtained in the microdiscs release experiments, any remnant trace of hydrofluoric acid, however low it may be, would be disastrous in the further biological tests. These facts, along with the difficult handling of such hazardous substance, routed our search to another sacrificial layer.

c) Copper sacrificial layer

Copper is a common sacrificial layer in micromachining processes that can be selectively etched using different solutions [37-39]. 50 nm of copper were sputtered over a silicon wafer with 400 nm of SiO_2 (Table 1.6) and the microdiscs were fabricated by photolithography on top of it. Then, the copper was chemically etched by a mixture of copper chloride (<10 wt.%) and ammonium hydroxide (<5 wt.%). Chloride ions react with the copper precipitating as CuCl. However, ammonia is known as a strong complexing agent capable of forming soluble copper complexes such as $Cu(NH_3)^{2+}$ and $Cu(NH_3)_4^{2+}$, which helps dissolving the precipitate compounds. After the etching, the wafer was horizontally removed from the etchant solution and immersed in DI water. The microdiscs were completely detached by several minutes of sonication. Figure 1.30*a* shows some microdiscs trapped in the CuCl precipitate, whereas in Figure 1.30*b* clean microdiscs can be seen after the addition of an appropriate volume of ammonium.

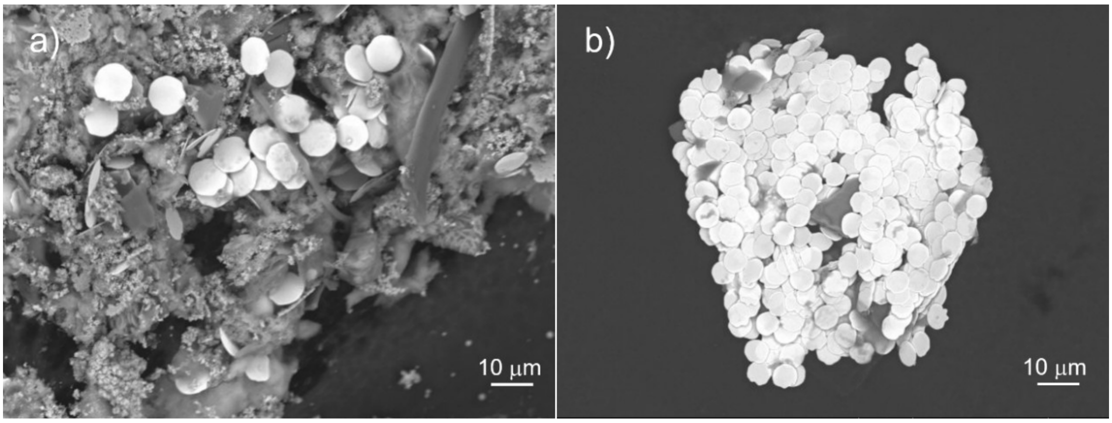

Figure 1.30. Microdiscs, 10 µm in diameter, after copper etching with (*a*) too low volume of NH_3OH and (*b*) with an appropriate volume of NH_3OH.

Although the success in releasing the microdiscs through the copper etching, the procedure presented important drawbacks like a low etching rate (less than 1 nm/min), a high opacity of the solution (deep purple colour) and the formation of precipitates, even though they can be dissolved. Furthermore, ion chlorides present a non-negligible reactivity with iron and nickel [40].

d) Germanium sacrificial layer

The germanium is easily etched by hydrogen peroxide (H_2O_2), which presents no reactivity with nickel and a negligible reactivity with iron [40]. Moreover, the products formed in the reaction are soluble [41]. Thereupon, 50 nm of germanium were sputtered over the silicon wafers with 400 nm of SiO_2 (Table 1.6) and microdiscs were, once again, fabricated by photolithography on top of it. After 3 min in H_2O_2 33 vol.%, the whole germanium thin film was removed and the wafer was carefully transferred to DI water. The microdiscs were completely detached after 1 min of sonication. They are shown in Figure 1.31.

Table 1.6. Sputtering parameters used in the fabrication of the discs. The Ar flux and the working pressure were kept constant at 10 sccm and $3.2 \cdot 10^{-3} mbar$.

Material	Power (W)	Voltage (V)	Intensity (A)	Rate (nm/min)
Ni_{80} Fe_{20}	100	373	0.28	25
Cr	60	288	0.20	2.5
Ti	60	307	0.23	4
Au	60	448	0.12	30
Cu	60	353	0.20	25
Ge*	50	150	-	4

*RF sputtering

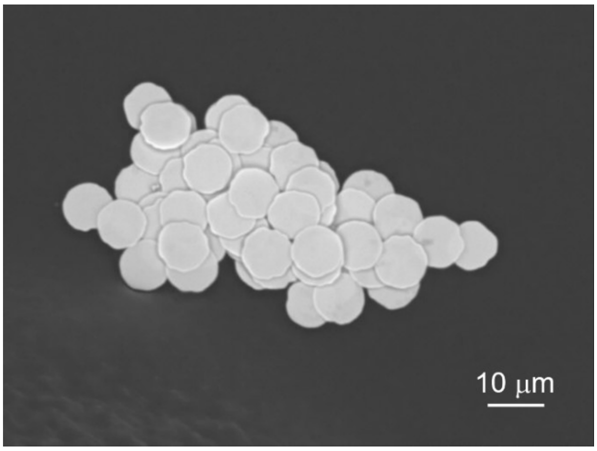

Figure 1.31. Microdiscs, 10 μm in diameter, released through the Ge-H_2O_2 procedure.

Due to the negligible reactivity between Permalloy and hydrogen peroxide, the formation of no precipitates, the transparency of the solution and the high etching rate (more than 15 nm/min), the germanium was selected as the optimum sacrificial layer to be adapted to hole-mask colloidal lithography for the release of nanodiscs. Hence, HCL was reproduced on a 50 nm of germanium thin film and nanodiscs with different dimensions were prepared. The nanodiscs were successfully released in the following manner: (*i*) a drop of H_2O_2 is incubated on the sample for 10 min, (*ii*) the sample with the drop is introduced in a 1 ml Eppendorf tube filled with DI water, (*iii*) the tube is sonicated for 5 min, (*iv*) the sample is removed from the tube and immersed in a second one, (*v*) the second tube is sonicated for 5 min to ensure the complete detachment of the nanodiscs, (*vi*) both tubes are placed onto a NdFeB permanent magnet overnight to collect the nanostructures at the bottom, (*vii*) the supernatant is removed and replaced by DI water three times. We developed this "drop-etching" method not to loss nanodiscs during the detachment process. Figure 1.32*a* shows a SEM image of a group of 40 nm thick Permalloy discs, 30 nm in radius, sandwiched between two 5 nm thick gold layers, whereas the discs shown in Figure 1.32*b* are 70 nm in radius and 30 nm thick covered with 3 nm of gold.

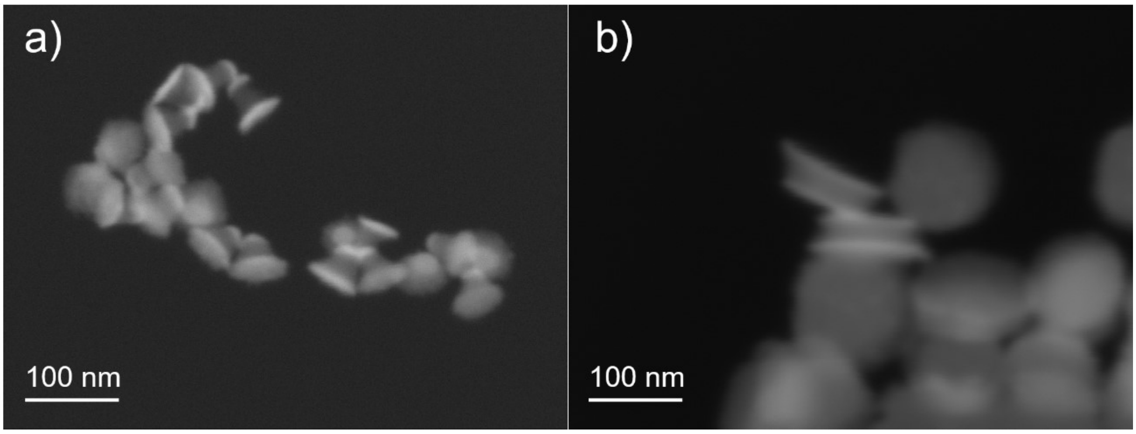

Figure 1.32. Nanodiscs fabricated by HCL and released using a germanium sacrificial layer. *a*) 30 nm in radius and 5 nm Au- 40 nm $Fe_{20}Ni_{80}$ – 5 nm Au thick. *b*) 70 nm in radius and 3 nm Au - 30 nm $Fe_{20}Ni_{80}$ - 3 nm Au thick.

1.2. Microfabrication

Microdiscs of two different sizes were used for two purposes: (1) discs 10 μm in diameter were used to search for the optimum release procedure that has been explained in the previous section, and (2) discs 2 μm in diameter were used to study the influence of the size in the experiments with cancer cells. Indeed, most of the works reported in the literature, used 1-2 μm Permalloy discs to treat cancer cells through magneto-mechanical actuation [42-44]. Our motivation was to perform a comparative study between the nanodiscs and the well-stablished microdiscs to investigate the influence of the size in the cell uptake, cytotoxicity and magneto-mechanical actuation effectiveness. This will be explained in Chapter 3.

Both sets of microdiscs were fabricated by standard optical lithography. The fabrication of the larger discs, 10 μm in diameter, was performed in the Clean Room of the University of the Basque Country (UPV/EHU). The smaller discs with a diameter of 2 μm, instead, were prepared in the Clean Room facilities of the Cavendish Laboratory and Nanoscience Centre at the University of Cambridge during my 3 months stay within the group of *Thin Film Magnetism* under the supervision of Prof. Russell Cowburn and Dr. Rhodri Mansell.

1.2.1. Optical lithography

The photolithography is the most widely used form of lithography. In the integrated circuits industry, pattern transfer from masks onto thin films is accomplished almost exclusively via photolithography. Basically, it uses light, typically ultra-violet

(UV), to transfer a geometric pattern from a photomask to a light-sensitive chemical resist on the substrate [45].

The fabrication of the microdiscs by photolithography involves 5 main stages: (1) spin-coating of the photoresist on a silicon wafer, (2) UV radiation to transfer the pattern from the photomask to the resist layer, (3) removal of the non-crosslinked resist or development, (4) deposition of the Permalloy and (5) lift-off. The flow diagram presented in the Figure 1.33 summarizes the procedure. Depending on the pattern of the photomask, the lift-off will reveal an array of discs on the substrate (Figure 1.33*a*) or it will release the discs from the substrate (Figure 1.33*b*).

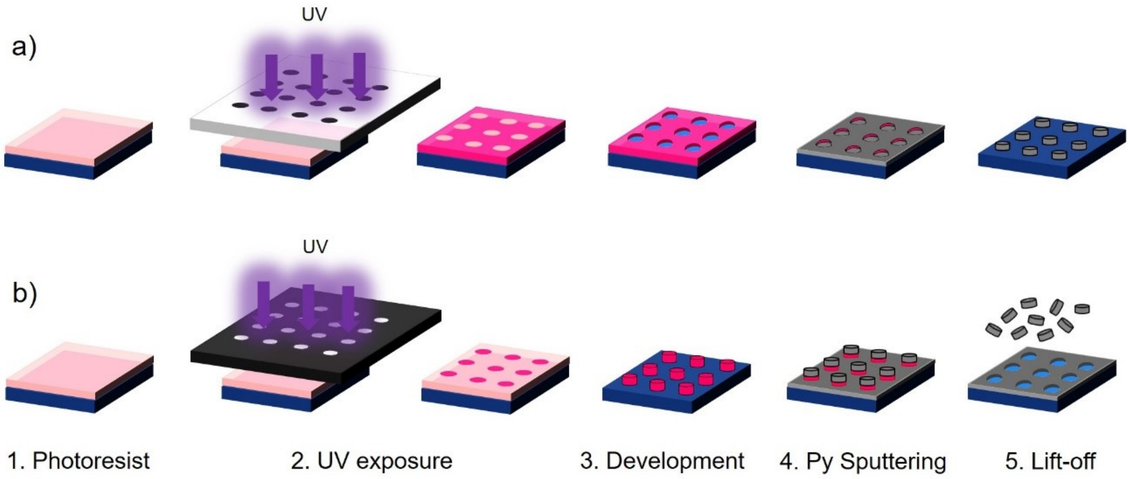

Figure 1.33. Flow diagram of photolithography to prepare Permalloy microdiscs using negative photoresist. The discs can be either attached to the substrate, if using a mask with opaque dots (*a*), or released from the substrate, in the case of using a mask with an opaque anti-dot structure (*b*).

To improve the resist film adhesion to silicon oxide surface, hexamethyldisilazane (HMDS) was applied. HMDS chemically bonds its Si atoms to the oxygens of oxidized surfaces, accompanied by the release of ammonia (NH_3). The methyl groups of the HMDS fragment thereby form a hydrophobic surface and, thus, improve resist wetting and adhesion. The HMDS was applied by spin-coating: (*i*) 1000 rpm for 15 s to spread the HMDS solution evenly; (*ii*) 4000 rpm for 30 s to obtain a thin and uniform HMDS layer; (*iii*) 1000 rpm for 15 s to deaccelerate.

The light-sensitive resist or photoresist can be positive (the portion of the photoresist that is exposed to light becomes soluble to the developer) or negative (the portion of the photoresist that is exposed to light becomes insoluble to the developer). In this work, ma-N 1400 negative tone photoresist was employed (Micro Resist Technology). After wafer cleaning by the standard process described in the section 1.1.2. (*PMMA spin-coating* step), the resist was spin-coated. The final spin-coating program consists of three stages: (*i*) 1000 rpm for 5 s to spread the resist solution evenly; (*ii*) 3000 rpm for 30 s to obtain a uniform resist layer of 1 μm (according to the spin speed curve from Micro Resist Technology specifications); (*iii*) 1000 rpm for 5 s to deaccelerate. The resist layer was afterwards pre-baked on a hot plate at 100 °C for 90 s to evaporate the solvent.

The pattern of the photomask was transferred to the resist by ultra-violet light exposure. The designs of the photomasks were performed by Autocad software and manufactured by JD Photo Data. The photomasks consist of a low reflective chromium oxide on soda lime glass. The only difference between the fabrication of the 10 μm and 2 μm discs lies in the photomask pattern: in the first case, only the dots are painted with chromium oxide (Figure 1.33*a*), whereas in the second case, the pattern is the inverse (see Figure 1.33*b*). The photo-mask was placed on top of the resist-coated wafer in such a way as the chromium oxide face contacted the resist. The chromium oxide is opaque to UV light, whereas the glass is transparent. The exposure dose needed to crosslink the ma-N 1410 photoresist is 350 ± 30 mJ cm^{-2}, which divided by the incident light intensity (mW cm^{-2}), measured before each exposure, gives the exposure time, resulting in 23 s for the 10 μm dots and 28 s for the 2 μm dots.

Then, the non-crosslinked portion of the resist was dissolved by the proper developer, in this case ma-D 533/S. The development time is also important as it determines the undercut which is critical for the further lift-off step. The beaker with developer was placed in the ultrasonic bath and the vertically immersed wafer was gently moved back and forth. Following the photoresist and developer specifications, the 10 μm dots resist was developed for 90 s (1 μm of undercut), revealing the hole-patterned resist (Figure 1.34*a*), whereas the 2 μm dots resist was developed for 70 s (0.8 μm of undercut), revealing the pillar-patterned resist (Figure 1.34*b*).

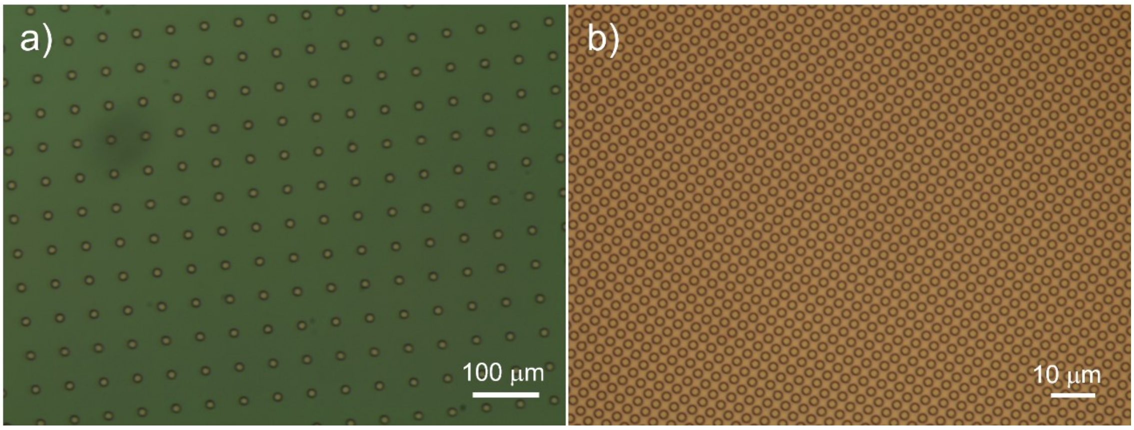

Figure 1.34. Photoresist patterned by UV-lithography. *a*) Photoresist with holes 10 μm in diameter. *b*) Photoresist pillars 2 μm in diameter.

Afterwards, the gold-Permalloy-gold multilayer was deposited on top of the patterned resists with the following thicknesses: 10 nm Au – 180 nm Permalloy – 10 nm Au for the 10 μm discs and 5 nm Au – 60 nm Permalloy – 5 nm Au for the 2 μm discs. The deposition of the larger discs' multilayer was carried out by means of DC magnetron sputtering (Table 1.6). The smaller discs, instead, were deposited by thermal evaporation at the University of Cambridge. The fundamentals and the specifications of the system are described in the Appendix A.

Finally, the patterned resist and the multilayer on top of it were removed by immersing the wafer in acetone for 2 h and sonicating it for less than 1 min. In this way, the 10 μm dots appear on the substrate (Figure 1.35*a*), whereas the 2 μm discs are released from it. The 2 μm discs' solution was replaced by water after several cleaning steps. The particles are shown in the Figure 1.35*b*.

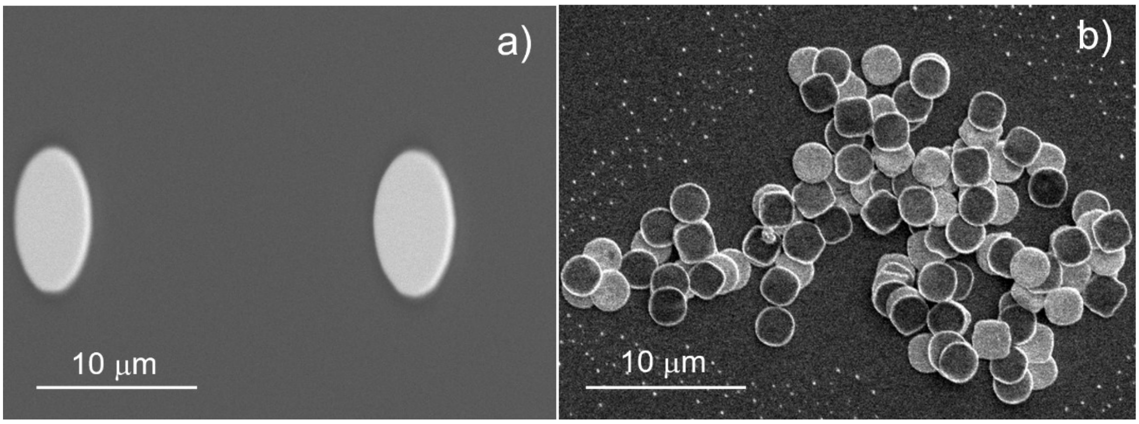

Figure 1.35. Microdiscs (*a*) 10 μm in diameter and (*b*) 2 μm in diameter fabricated by UV-lithography.

However, the lift-off of the discs 2 μm in diameter presented some difficulties. Indeed, in some cases, the surrounding gold-Permalloy-gold layer, deposited on top of the silicon oxide, was detached from the wafer as well, as shown in Figure 1.36*a*. The adherence of the gold to the silicon oxide is low and, most likely, the short sonication time applied in the lift-off process, was sufficient to peel off the gold-Permalloy-gold anti-dot structure. The titanium instead, presents a higher adhesion to the silicon oxide and is biocompatible. Thus, we sputtered Ti 5 nm - $Ni_{80}Fe_{20}$ 60 nm - Ti 5 nm on top of the patterned wafer. As expected, the lift-off worked well, as shown in Figure 1.36*b*, and so, titanium was used as capping layer in all other wafers.

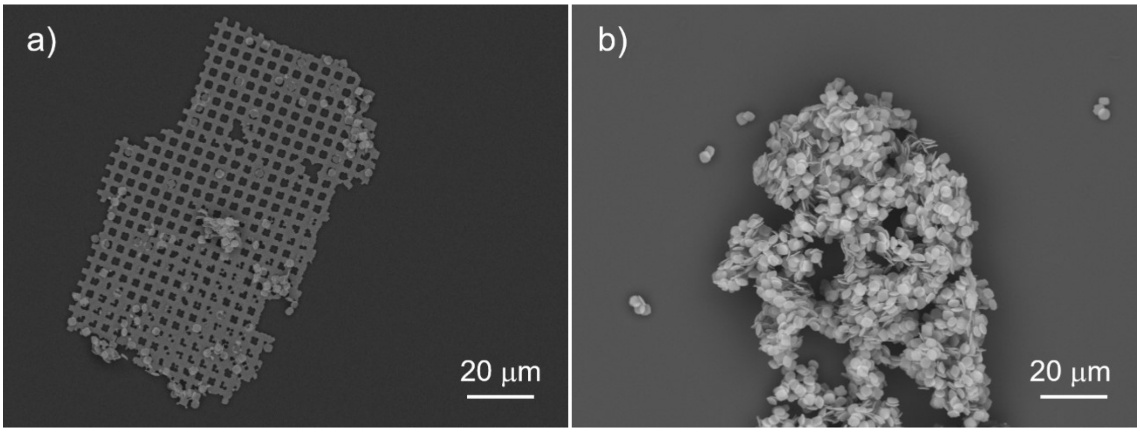

Figure 1.36. Scanning electron micrographs after the lift-off of the microdiscs (R = 1 mm and T = 60 nm). *a*) During the lift-off of the microdiscs covered with gold, the surrounding anti-dot structure is peeled off together with the particles. *b*) Using titanium, only the microdiscs are released from the wafer.

1.3. Comparison of the fabrication techniques

In this chapter, we have assessed the suitability of three template-based fabrication routes to prepare Permalloy nanodiscs. The first one, based on the use of porous alumina membranes, despite its demonstrated potential to fabricate disc-shaped nanostructures, did not yield the expected results and brought important issues that required additional efforts to be solved. The second approach called nanosphere lithography (NSL) that uses polystyrene spheres in a close packed hexagonal structure as template, allowed us to prepare sub-micrometric Permalloy and silicon oxide dots. However, the difficulty of obtaining monolayers of spheres over large areas, led us to adopt a new strategy introducing charged polystyrene spheres in a variant of NSL called hole-mask colloidal lithography (HCL). Through HCL, we were able to prepare Permalloy discs down to 30 nm in radius, with the desired thickness, over the whole area of the substrate thanks to the electrostatic interactions of the spheres. Remarkably, the production yield of the HCL exceeds 4×10^{10} nanodiscs per wafer, which corresponds to 80 μg of material (considering nanodiscs with $R = 35$ nm and $T = 50$ nm). Moreover, the cost-calculations regarding the consumables employed in HCL (without taking into account the facilities), result in an approximate cost per wafer less than 5 €, similar to that calculated for the wafer processing using the optical lithography to prepare microdiscs. However, for the preparation of nanostructures through optical lithography, the high-resolution deep-UV lithography is required which shoots up the costs of the processing. Thus, it has been demonstrated that with standard lab equipment as the sputtering and a reactive ion etching, it is possible to fabricate large amounts of sub-100 nm disc-shaped particles in a relatively short time (~ 11 h per wafer). Additionally, a novel nanoparticles release procedure, based on a germanium sacrificial layer, has been developed and adapted to the HCL for the application of the nanodiscs in biomedicine.

References

[1] S. Laurent, D. Forge, M. Port, A. Roch, C. Robic, L. Vander Elst and R. N. Muller, “Magnetic iron oxide nanoparticles: synthesis, stabilization, vectorization, physicochemical characterizations, and biological applications”, *Chemical Reviews*, vol. 108, pp. 2064-110, 2008.

[2] I. Castellanos-Rubio, M. Insausti, E. Garaio, I. Gil de Muro, F. Plazaola, T. Rojo and L. Lezama, “Fe_3O_4 nanoparticles prepared by the seeded-growth route for hyperthermia: electron magnetic resonance as a key tool to evaluate size distribution in magnetic nanoparticles”, *Nanoscale*, vol. 6, pp. 7542-52, 2014.

[3] E. An-Hui Lu, L. Salabas and F. Schüth, “Magnetic Nanoparticles: Synthesis, Protection, Functionalization, and Application”, *Angewandte Chemie International Edition,* vol. 46, pp. 1222-1244, 2007.

[4] T. Shinjo, T. Okuno, R. Hassdorf, K. Shigeto and T. Ono, “Magnetic Vortex Core Observation in Circular Dots of Permalloy”, *Science*, vol. 289, pp. 930-2, 2000.

[5] V. Novosad, K. Y. Guslienko, H. Shima, Y. Otani, S. G. Kim, K. Fukamichi, N. Kikuchi, O. Kitakami and Y. Shimada, “Effect of interdot magnetostatic interaction on magnetization reversal in circular dot arrays”, *Physical Review B*, vol. 65, pp. 060402, 2002.

[6] S-H. Chung, R. D. McMichael, D. T. Pierce and J. Unguris, “Phase diagram of magnetic nanodisks measured by scanning electron microscopy with polarization analysis”, *Physical Review B*, vol. 81, pp. 024410, 2010.

[7] C. A. Ross, M. Hwang, M. Shima, J. Y. Cheng, M. Farhoud, T. A. Savas, H. I. Smith, W. Schwarzacher, F. M. Ross, M. Redjdal and F. B. Humphrey, “Micromagnetic behavior of electrodeposited cylinder arrays”, *Physical Review B*, vol. 65, pp. 144417, 2002.

[8] S-W. Lee, K-S. Lee, J. Ahn, J-J. Lee, M-G. Kim and Y-B. Shin, “Highly sensitive biosensing using arrays of plasmonic Au nanodisks realized by nanoimprint lithography”, *ACS Nano*, vol. 5, pp. 897-904, 2011.

[9] C. T. Sousa, D. C. Leitao, M. P. Proenca, J. Ventura, A. M. Pereira and J. P. Araujo, "Nanoporous alumina as templates for multifunctional applications", *Applied Physics Reviews*, vol. 1, pp. 031102, 2014.

[10] P. Colson, C. Henrist and R. Cloots, "Nanosphere Lithography: A Powerful Method for the Controlled Manufacturing of Nanomaterials", *Journal of Nanomaterials*, vol. 2013, 948510, 2013.

[11] L. G. Vivas, Y. P. Ivanov, D. G. Trabada, M. P. Proenca, O. Chubykalo-Fesenko and M. Vázquez, "Magnetic properties of Co nanopillar arrays prepared from alumina templates", *Nanotechnology*, vol. 24, pp. 105703, 2013.

[12] C. L. Cheung, R. J. Nikoli, C. E. Reinhardt and T. F. Wang, "Fabrication of nanopillars by nanosphere lithography", *Nanotechnology,* vol. 17, pp. 1339–1343, 2006.

[13] K. L. Hobbs, P. R. Larson, G. D. Lian, J. C. Keay and M. B. Johnson, "Fabrication of Nanoring Arrays by Sputter Redeposition Using Porous Alumina Templates", *Nano Letters*, vol. 4, 2004.

[14] A. Kosiorek, W. Kandulski, H. Glaczynska and M. Giersig, "Fabrication of Nanoscale Rings, Dots, and Rods by Combining Shadow Nanosphere Lithography and Annealed Polystyrene Nanosphere Masks", *Small*, vol. 1, pp. 439-444, 2005.

[15] P. Gawronski, K. J. Merazzo, O. Chubykalo-Fesenko, R. P. del Real and M. Vázquez, "Micromagnetism of permalloy antidot arrays prepared from alumina templates", *Nanotechnology*, vol. 25, pp. 475703, 2014.

[16] P. Tiberto, G. Barrera, L. Boarino, F. Celegato, M. Coïsson, N. De Leo, F. Albertini, F. Casoli and P. Ranzieri, "Arrays of ordered nanostructures in Fe–Pt thin films by self-assembling of polystyrene nanospheres", *Journal of Applied Physics*, vol. 113, pp. 17B516, 2013.

[17] Kai Liu, J. Nogués, C. Leighton, H. Masuda, K. Nishio, I. V. Roshchin and I. K. Schuller, "Fabrication and thermal stability of arrays of Fe nanodots", *Applied Physics Letters*, vol. 81, pp. 4434-4436, 2002.

[18] C. T. Sousa, D. C. Leitao, J. Ventura, P. B. Tavares and J. P. Araújo, “A versatile synthesis method of dendrites-free segmented nanowires with a precise size control”, *Nanoscale Research Letters*, vol. 7, pp. 168, 2012.

[19] W. L. Gan, M. Chandra Sekhar, D. W. Wong, I. Purnama, S. Y. Chiam, L. M. Wong, and W. S. Lew, “Multi-vortex states in magnetic nanoparticles”, *Applied Physics Letters*, vol. 105, pp. 152405, 2014.

[20] E. K. Semenova, F. Montoncello, S. Tacchi, G. Dürr, E. Sirotkin, E. Ahmad, M. Madami, G. Gubbiotti, S. Neusser, D. Grundler, F. Y. Ogrin, R. J. Hicken, V. V. Kruglyak, D. V. Berkov, N. L. Gorn and L. Giovannini, “Magnetodynamical response of large-area close-packed arrays of circular dots fabricated by nanosphere lithography”, *Physical Review B*, vol. 87, pp. 174432-19, 2013.

[21] P. Tiberto, L. Boarino, F. Celegato, M. Coisson, E. Enrico, N. de Leo, F. Vinai and P. Allia, “Synthesis of Ni80Fe20 and Co nanodot arrays by self-assembling of polystyrene nanospheres: magnetic and microstructural properties”, *Journal Nanoparticle Research*, vol. 13, pp. 4211-4218, 2011.

[22] P. Hanarp, D. S. Sutherland, J. Gold and B. Kasemo, “Control of nanoparticle film structure for colloidal lithography”, *Colloids and Surfaces*, vol. 214, pp. 23-26, 2003.

[23] H. Fredriksson, Y. Alaverdyan, A. Dmitriev, C. Langhammer, D. Sutherland, M. Zäch and B. Kasemo, “Hole-mask colloidal lithography”, *Advanced Materials*, vol. 19, pp. 4297-4302, 2007.

[24] H. Y. Feng, F. Luo, D. Meneses-Rodríguez, G. Armelles and A. Cebollada, “From disk to ring: aspect ratio control of the magnetoplasmonic response in Au/Co/Au nanostructures fabricated by hole-mask colloidal lithography”, *Applied Physics Letters*, vol. 106, pp. 083105, 2015.

[25] M. A. Otte, M. C. Estévez, L. G. Carrascosa, A. B. González-Guerrero, L. M. Lechuga and B. Sepúlveda, “Improved biosensing capability with novel suspended nanodisks”, *Journal of Physical Chemistry C,* vol. 115, pp. 5344–5351, 2011.

[26] H. Masuda and K. Fukuda, “Ordered Metal Nanohole Arrays Made by a Two-Step Replication of Honeycomb Structures of Anodic Alumina”, *Science*, vol. 268, pp. 1466-1468, 1995.

[27] A. V. Svalov, I. R. Aseginolaza, A. García-Arribas, I. Orue, J. M. Barandiaran, J. Alonso, M. L. Fernández-Gubieda and G. V. Kurlyandskaya, “Structure and magnetic properties of thin Permalloy films near the ‘transcritical’ state”, *IEEE Transactions on Magnetics*, vol. 46, pp. 333-6, 2010.

[28] J. Lee, J. U. Ha, S. Choe, C-S. Lee and S. E. Shim, “Synthesis of highly monodisperse polystyrene microspheres via dispersion polymerization using an amphoteric initiator”, *Journal of Colloid and Interface Science*, vol. 298, pp. 663-671, 2006.

[29] H. Qi, W. Hao, H. Xu, J. Zhang and T. Wang, “Synthesis of large-sized monodisperse polystyrene microspheres by dispersion polymerization with dropwise monomer feeding procedure”, *Journal of Colloid and Interface Science*, vol. 287, pp. 243-248, 2008.

[30] N. Vogel, S. Goerres, K. Landfester and C. K. Weiss, “A convenient method to produce close- and non-close-packed monolayers using direct assembly at the air–water interface and subsequent plasma-induced size reduction”, *Macromolecular Chemistry and Physics*, vol. 212, pp. 1719–34, 2011.

[31] T. R. Jensen, M. L. Duval, K. L. Kelly, A. A. Lazarides, G. C. Schatz and R. P. Van Duyne, “Nanosphere Lithography: Effect of the External Dielectric Medium on the Surface Plasmon Resonance Spectrum of a Periodic Array of Silver Nanoparticles”, *Journal of Physical Chemistry B*, vol. 103, pp. 9846-9853, 1999.

[32] Ch. Steinbrüchel, H. W. Lehmann and K. Frick, “Mechanism of Dry Etching of Silicon Dioxide”, *Journal of Electrochemical Society*, vol. 132, pp. 180-186, 1985.

[33] A. Vesel and M. Mozeti, “Surface modification and ageing of PMMA polymer by oxygen plasma treatment”, *Vacuum*, vol. 86, pp. 634-637, 2012.

[34] B. Zappone, K. J. Rosenberg and J. Israelachvili, “Role of nanometer roughness on the adhesion and friction of a rough polymer surface and a molecularly smooth mica surface”, *Tribology Letters*, vol. 26, pp.191-201, 2007.

[35] W. S. Rasband, 1997–2014 ImageJ, US National Institutes of Health, Bethesda, Maryland, USA http://imagej.nih. gov/ij/

[36] C. Iliescu, J. Jing, F. E. H. Taya, J. Miao and T. Sun, “Characterization of masking layers for deep wet etching of glass in an improved HF/HCl solution”, *Surface and Coatings Technology*, vol. 198, pp. 314– 318, 2005.

[37] J. Zou, C. Liu, J. Schutt-Aine, J. Chen and S-M. Kang, “Development of a Wide Tuning Range MEMS Tunable Capacitor for Wireless Communication Systems”, 2000, *IEEE*, 10.1109/IEDM.2000.904341.

[38] K. Kim, S. Park, J.-B. Lee, H. Manohara, Y. Desta, M. Murphy and C. H. Ahn, “Rapid replication of polymeric and metallic high aspect ratio microstructures using PDMS and LIGA technology”, *Microsystem Technologies*, vol. 9, pp. 5-10, 2002.

[39] Y. Ein-Eli and D. Starosvetsky, “Review on copper chemical–mechanical polishing (CMP) and post-CMP cleaning in ultra large system integrated (ULSI)”, *Electrochimica Acta*, vol. 52, pp. 1825-1838, 2007.

[40] P. Walkers and W. H. Tarn, “Handbook of metal etchants”, *CRC Press*, 1991.

[41] N. Cerniglia and P. Wang, “Dissolution of Germanium in Aqueous Hydrogen Peroxide Solution”, *Journal of the Electrochemical Society*, vol. 109, pp. 508-512, 1962.

[42] D-H. Kim, E. A. Rozhkova, I. V. Ulasov, S. D. Bader, T. Rajh, M. S. Lesniak and V. Novosad, “Biofunctionalized magnetic-vortex microdiscs for targeted cancer-cell destruction”, *Nature Materials*, vol. 9, pp. 165–171, 2010.

[43] S. Leulmi, X. Chauchet, M. Morcrette, G. Ortiz, H. Joisten, P. Sabon, T. Livache, Y. Hou, M. Carrière, S. Lequien and B. Dieny, “Triggering the apoptosis of targeted human renal cancer cells by the vibration of anisotropic magnetic particles attached to the cell membrane”, *Nanoscale*, vol. 7, pp. 15904, 2015.

[44] Y. Cheng, M. E. Muroski, D. C. M. C. Petit, R. Mansell, T. Vemulkar, R. A. Morshed, Y. Han, I. V. Balyasnikova, C. M. Horbinski, X. Huang, L. Zhang, R. P. Cowburn and M. S. Lesniak, “Rotating magnetic field induced oscillation of magnetic particles for in vivo mechanical destruction of malignant glioma”, *Journal of Controlled Release*, vol. 223, pp. 75-84, 2016.

[45] M. J. Madou, “Fundamentals of Microfabrication and Nanotechnology”, *CRC Press*, vol. II, 2012.

2

Magnetic properties and actuation

The ferromagnetic nanostructures studied in this work are made of Permalloy. This nickel-iron ($Ni_{80}Fe_{20}$) alloy is a soft ferromagnetic material with negligible anisotropy and magnetostriction. Ferromagnetic materials are characterized by a spontaneous magnetisation, generated by the alignment of the magnetic moments located on an atomic lattice [1]. At the macroscale, a ferromagnetic material is usually divided in domains where the magnetic moments are aligned in a definite direction. The domain configuration determines the magnetisation processes when a magnetic field is applied. However, at the nanoscale, the magnetic domains are absent and single domain states or other more exotic configurations appear. This is a paradigmatic example of the paramount importance of size in magnetism.

In the single domain state, the exchange energy dominates and the magnetic nanoparticle behaves as a simple giant spin [2]. With an increase in the particle size, the role of magnetostatic energy increases and disc-shaped particles of adequate dimensions can display the so-called spin-vortex configuration [3, 4]. The vortex state is characterized by the magnetic moments being curled in the plane of the disc, configured in closed circles to minimize the magnetostatic energy. Only at the centre, at the core of the vortex, the magnetic moments get out of the plane and point perpendicularly, to avoid a singularity as shown in Figure 2.1. The magnetic behaviour as a function of the in-plane applied magnetic field is characteristic for vortex structures: at low fields, the vortex core is displaced reversibly in the plane until it reaches the disc lateral border, where it is annihilated and the sample becomes magnetically saturated. Reducing the magnitude of the applied field, the vortex is nucleated again, but at a magnetic field of lower intensity than that for annihilation, and then follows back the original reversible path. This causes a very peculiar hysteresis loop, shown in Figure 2.2, with no remanence or coercive field and open lobes at high fields [5].

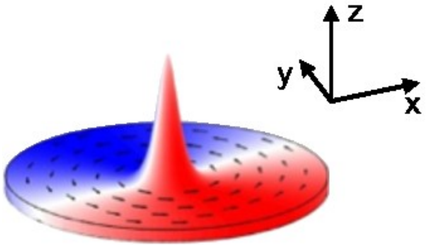

Figure 2.1. Representation of the magnetisation distribution in the ground magnetic vortex state for disc-shaped geometry, acquired from [6]. The colours represent the magnitude and orientation of the *x*-component of magnetisation. The 3D profile indicates the magnitude of its *z*-component.

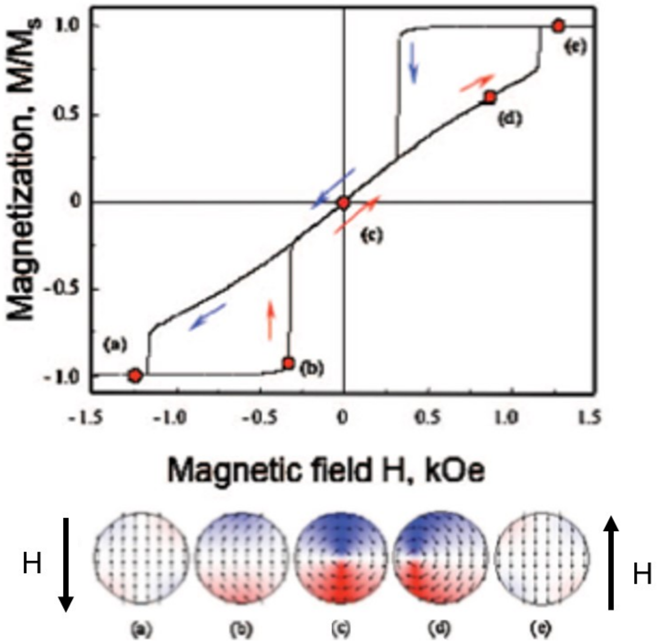

Figure 2.2. The typical hysteresis loop and magnetisation reversal process due to the vortex nucleation, displacement, and annihilation as calculated with a micromagnetic solver for an isolated disc with R = 0.1 μm and T = 30 nm adapted from [5]. The field is applied along the y-direction defined in Figure 2.1. The sketches at the bottom part show the configuration of the in-plane magnetisation in different points of the loop. The core of the vortex displaces perpendicularly to the applied field.

The particular curling configuration of the spins started to be theoretically studied back in the 70s first in spherical particles [7] and later in cylinders [8]. However, the concept of *magnetic vortex* was introduced by A. Hubert and R. Schäfer in 1998 [9]. One year later, R. Cowburn *et al.* measured the characteristic hysteresis loop of the vortex configuration through a high sensitivity magneto-optical method [3] whereas T. Shinjo *et al.* succeeded in imaging the perpendicular magnetisation core by magnetic force microscopy (MFM) [10]. Since then, the vortex state has been extensively studied both experimentally, through magneto-optic Kerr-effect magnetometry [11, 12], Lorentz transmission electron microscopy (LTEM) [13] or spin-polarized scanning tunnelling microscopy (SP-STM) [14], and theoretically, using micromagnetic modelling [15] and fully analytical descriptions [5]. Phase diagrams of the magnetic state as a function of the diameter to thickness aspect ratio have been also established experimentally [16], analytically [17] and by micromagnetic calculations [4, 18]. An example of them is presented in Figure 2.3. All of them indicate that three possibilities may exist for the ground state of the magnetisation: if the disc is very thin, all the magnetic moments are aligned in the plane (in-plane single domain); if the diameter is small and the disc is tall, the magnetisation is perpendicular to the plane of the disc (out-of-plane single domain); out of these cases, the ground state is vortex. However, despite its relevance, a very scarce number of works can be found on sub-100 nm vortex structures [16, 18-20], mainly due to the difficulty of sample preparation and the limitations of the characterization techniques. In this chapter, we study the magnetic behaviour of Permalloy discs down to 30 nm in radius from an experimental, theoretical and analytical point of view. According to the phase diagram calculated by Scholz *et al.* [4] (Figure 2.3), the radius of 30 nm (marked with a red line) is close to the lower boundary of the vortex configuration, which gave us the opportunity of exploring the limits of the vortex stability at the nanoscale by varying the thickness.

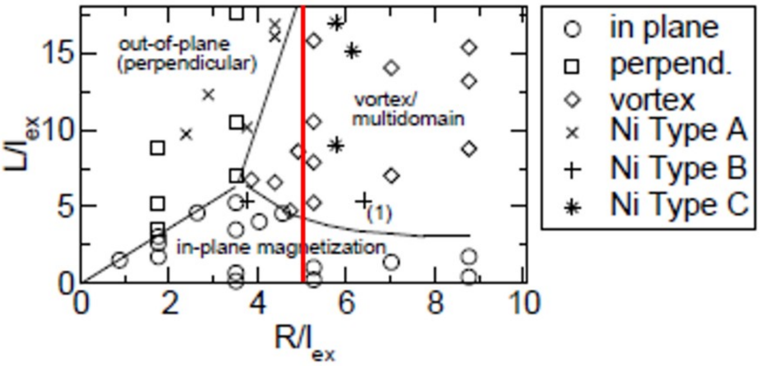

Figure 2.3. Phase diagram of magnetic ground states (axis scaling in units of the exchange length taken as l_{ex} = 5.7 nm) calculated by Scholz *et al.* [4]. The data points indicated by the open symbols have been calculated. The experimental data have been taken from [18]. The red line corresponds to Permalloy nanodiscs with R = 30 nm and different thicknesses that were studied in this Thesis.

The study of the magnetic behaviour of Permalloy nanodiscs, prepared by hole-mask colloidal lithography, was developed in two phases: first, the measurement of the magnetic properties, including the magnetisation processes and the vortex structure, and, second, the assessment of the behaviour of the nanodiscs in fluid, which was interesting for the final experiments with cancer cells.

2.1. Magnetic characterization

The magnetisation processes of the nanodiscs were studied by measuring the hysteresis loops, either through magneto-optic Kerr effect magnetometry (MOKE) or with a magnetometer based on a superconducting quantum interference device (SQUID). The first order reversal curve (FORC) method was employed in one sample of nanodiscs. Additionally, the vortex cores of the nanodiscs were imaged using magnetic force microscopy (MFM). The main features of each measurement device are described in Appendix A. To explain some points of the measured hysteresis loops and to gain insight in the magnetic behaviour of the small vortex discs, micromagnetic simulations were performed. Lastly, a new analytical model is proposed to describe the magnetisation reversal processes accounting for the particularities encountered in such small discs.

2.1.1. Magnetisation processes

In order to assess the region of the vortex stability at the nanoscale, we set the radius of Permalloy discs to 30 nm and varied the thickness from 20 to 50 nm. The studied samples, named S20, S30 and S50, are situated by red dots in the schematic phase diagram, shown in Figure 2.4, outlined from previously published data [21]. The results of larger discs with $R = 70$ nm (L30 and L50), also situated in the phase diagram, will be later discussed.

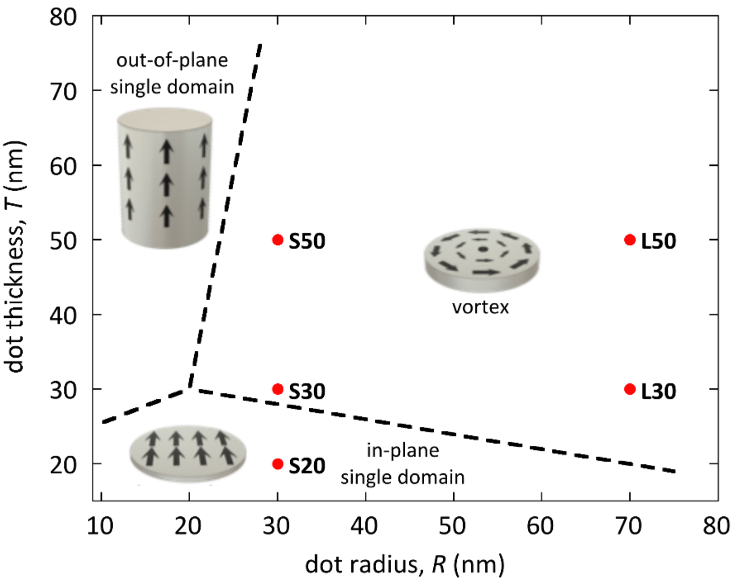

Figure 2.4. Schematic phase diagram of the magnetic ground state of Permalloy discs, as a function of their thickness and radius, elaborated from experimental and theoretical results. The dashed lines separate the regions with different magnetic configurations. The arrows drawn in the cylinders reflect the configuration of the magnetisation. The samples studied in this work are situated in the diagram by red dots.

The measured hysteresis loops for the discs having a radius of R = 30 nm are presented in Figure 2.5. The shape of the hysteresis loop of T = 20 nm (Figure 2.5*a*) corresponds to a single domain behaviour where the in-plane magnetic moments reverse all at once in low magnetic fields, similarly to monodomain nanoparticles, which is consistent with its position in the phase diagram. Discs with T = 30 nm (Figure 2.5*b*) already presents the main features of a magnetic vortex configuration, but there can still be some reminiscence of single domain behaviour, hinted by the presence of a considerable remanence in the loop. This is compatible with the existence of an intermediate metastable state, between single domain and vortex state, which has already been disclosed in 97 nm wide and 26 nm thick Permalloy discs [11]. In this work, three remanence states were detected corresponding to different sweeping field regimes after demagnetizing the structures into their ground state: discs with zero remanence (vortex); discs with a remanence ratio of 0.3 (intermediate state); discs close to full remanence (in-plane single domain). In our case, the discs are certainly close to phase boundary, but the vortex configuration is already predominant demonstrating that, with a radius of 30 nm, the thickness of 30 nm is probably the minimum possible for obtaining clear vortex behaviour without the dominance of the in-plane single domain reversal processes.

The vortex state is better defined in the discs with T = 50 nm (Figure 2.5*c*), meaning that the hysteresis loop definitely presents the characteristic shape produced by the vortex configuration and its magnetisation reversal process, displaying negligible coercivity, large permeability at zero field and hysteretic lobes at higher fields. Previous experimental evidence of the vortex behaviour in these range of dimensions (iron discs with ~60 nm in diameter reported in [19, 22]) have not produced such perfectly shaped loops.

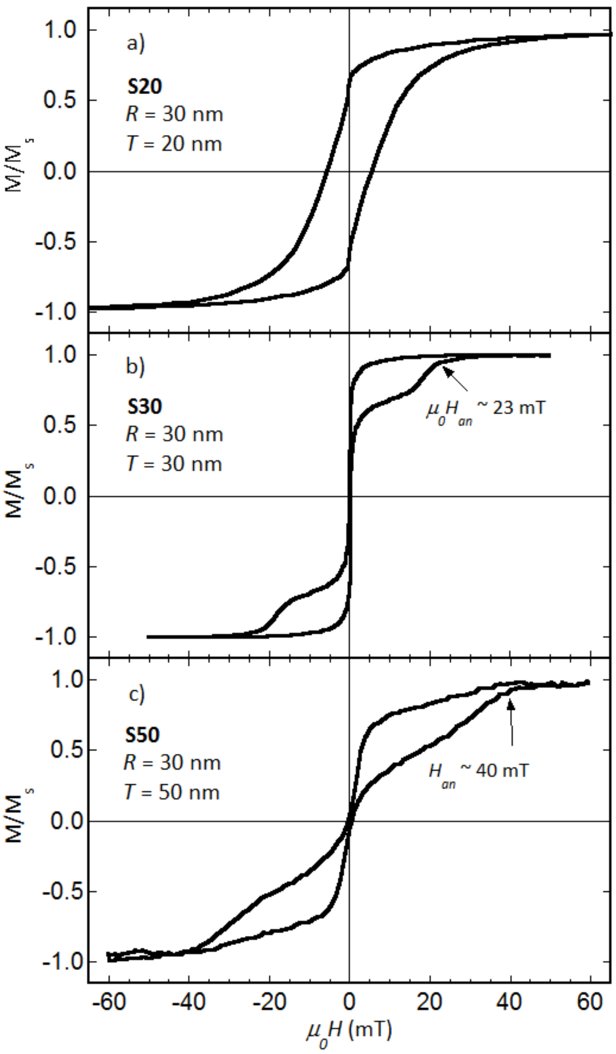

Figure 2.5. Hysteresis loops of $Ni_{80}Fe_{20}$ nanodiscs with nominal radius of R = 30 nm. *a*) SQUID loop of sample S20 with a thickness T = 20 nm, displaying an in-plane single domain behaviour. *b*) SQUID loop of sample S30 with a thickness T = 30 nm. *c*) MOKE loop of sample S50 with a thickness T = 50 nm.

Nevertheless, the hysteresis loop of the sample S50 does not display the canonical vortex shape as predicted by theory [4, 5] or measured in perfectly EBL-defined microdiscs [3], because the vortex annihilation and recovery from saturation until the vortex nucleation present a marked slanted shape. Although the main characteristics of the vortex magnetisation reversal prevail, there seems to be some degree of coherent rotation of the magnetisation. To support this assertion, Figure 2.6 displays the loop of an ideal monodomain spheroidal particle in which the magnetisation reversal takes place completely by coherent rotation producing a linear slanted shape. The shape of the loop of sample S50 indicates the existence of a significant out-of-plane component of the magnetisation, which is clearly a consequence of the closeness of this sample to the region of the stable out-of-plane single domain state.

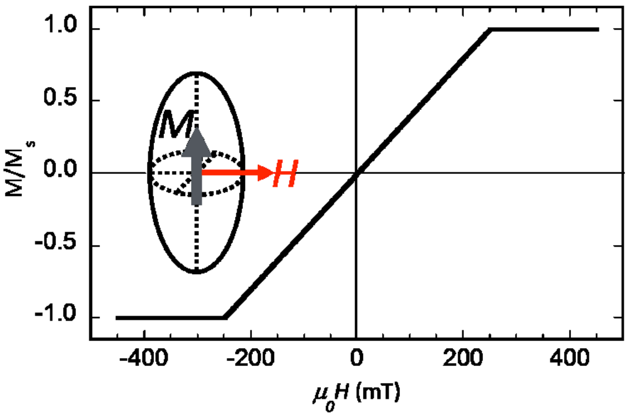

Figure 2.6. The magnetisation curve of an ideal out-of-plane monodomain spheroidal particle in which the magnetisation reversal takes place by coherent rotation.

However, we have also considered that the shape of the loop of the sample S50 could be the result of the averaged contribution of discs with a finite size distribution. To investigate this possibility, micromagnetic calculations with the OOMMF code [23] were performed[1] with a cell size of 4 nm and the material parameters typically employed for Permalloy [4]: saturation magnetisation $M_S = 8 \times 10^5 \mathrm{A\,m^{-1}}$, exchange constant $A = 1.3 \times 10^{-11} \mathrm{J\,m^{-1}}$, no anisotropy. A large Gilbert damping coefficient $\alpha = 0.5$ was used to speed up the calculations. The magnetisation curves for different aspect ratios were systematically calculated. Incidentally, this allowed us to determine our own phase diagram, which is depicted in Figure 2.7 and coincident with those obtained by other authors [4, 16-18]. The magnetic map of the Figure 2.4 is actually a schematic version of this phase diagram.

---

[1] OOMMF simulations were performed by the physics student Mikel Rouco during his end-of-degree project in the University of the Basque Country (UPV/EHU).

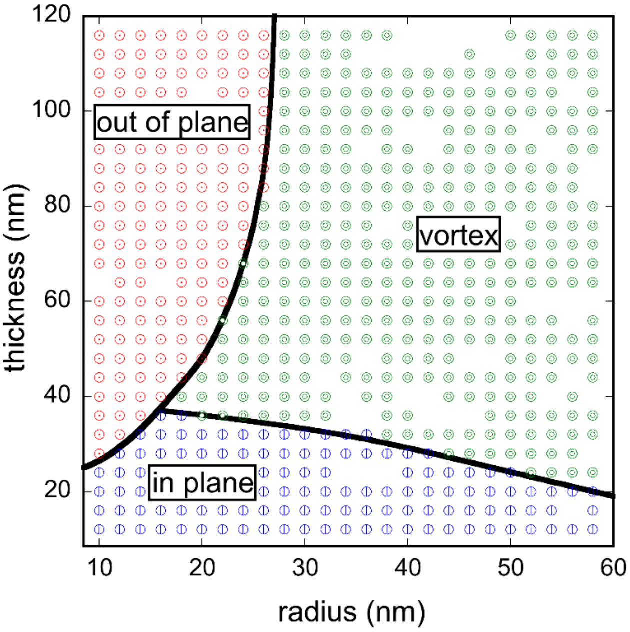

Figure 2.7. Calculated phase diagram of the magnetic behaviour of Permalloy discs depending on their aspect ratio.

The hysteresis loop calculated for a single disc with a radius of 30 nm, shown in the inset of Figure 2.8, displays the canonical behaviour of a vortex structure, with sharply defined annihilation and nucleation jumps. When the simulation includes a wide set of nanodiscs with different sizes, the resulting magnetic response is averaged and the vortex loop is smoothed. The loop in Figure 2.8 was obtained using a distribution of sizes taken directly from a SEM image of the prepared nanodiscs (shown in the lower inset of Figure 2.8). The computed loop satisfactorily resembles the measured one, displayed in Figure 2.5*c*.

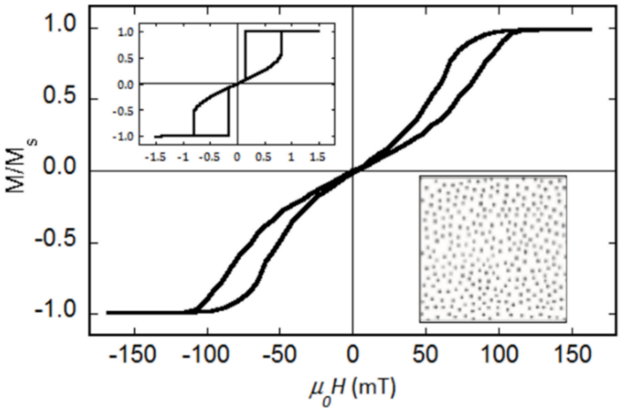

Figure 2.8. Micromagnetic calculation of the hysteresis loop corresponding to an ensemble of nanodiscs with a mean radius of 30 nm. The upper inset shows the canonical hysteresis loop of the vortex state, calculated for a single disc with R = 30 nm. The lower inset shows the set of discs, obtained from a SEM image in section 1.1.2, used in the calculation of the loop.

On the other hand, the simulations presented above were performed for perfectly shaped cylindrical structures, whereas our discs are not strictly so, most of all in the case of discs having $R = 30$ nm and $T = 50$ nm, as pointed in the Chapter 1. Figure 2.9 compares the micromagnetic simulation of a perfectly cylindrical disc to the one of a dome-shaped disc of the same radius and total height. The calculated hysteresis loops are not identical, but the main features are the same.

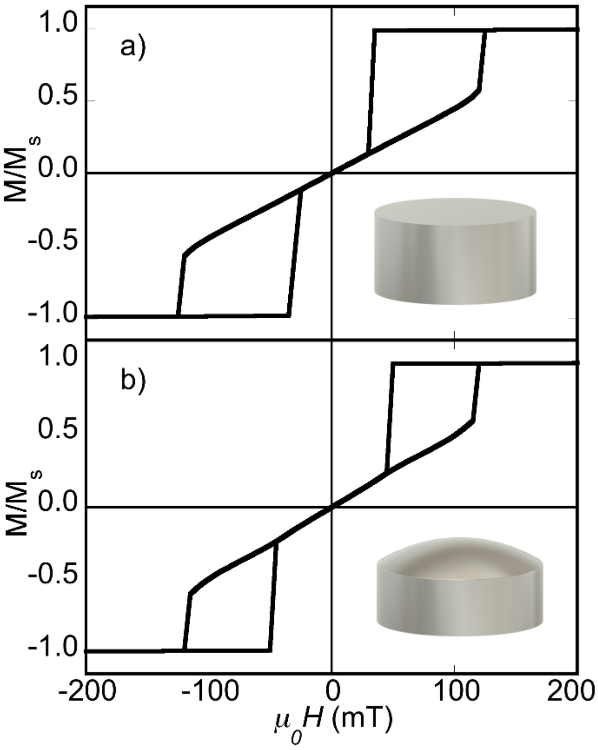

Figure 2.9. Comparison of micromagnetic calculations for two nanostructures with the same radius and total thickness. The loop in (*a*) corresponds to a perfectly cylindrical disc (the ones used to calculate the phase diagram of Figure 2.7). The loop in (*b*) corresponds to a dome-shaped disc with a saggita of 20 % of the total height.

In any case, importantly, the samples S20, S30 and S50 served us to experimentally assess the region of vortex stability in discs with 30 nm radius, predicting this region to be delimited by a thickness range between 30 nm and 50 nm. Moreover, the observed magnetic behaviours nicely fit within the magnetic phase diagram. This constitutes an additional evidence of the quality of the prepared nanostructures regarding their magnetic behaviour.

As mentioned in the Chapter 1, larger nanodiscs, 70 nm in radius, were also prepared because, as they are expected to present a clear vortex configuration for a wider range of thicknesses (see phase diagram of Figure 2.4), they could help to understand the behaviour of the smaller discs. Figure 2.10 displays the hysteresis loops measured in the discs with $R = 70$ nm. For both samples with different thicknesses $T = 30$ nm and $T = 50$ nm, the shape of the hysteresis loop is the canonical one corresponding to the classical vortex behaviour. The finite remanence and coercivity present in the SQUID measurement plotted in Figure 2.10*a* may come from a non-representative, badly patterned part of the sample, and probably at the border of the substrate, since it is not present in the loop measured by MOKE, shown in the inset.

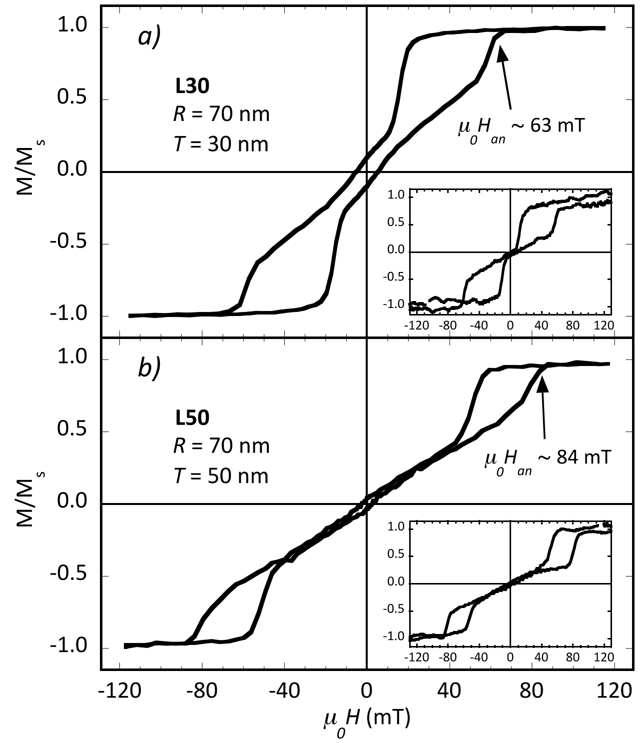

Figure 2.10. Hysteresis loops of $Ni_{80}Fe_{20}$ nanodiscs with nominal radius of $R = 70$ nm. *a)* SQUID loop of sample L30 with a thickness $T = 30$ nm. *b)* SQUID loop of sample L50 with a thickness $T = 50$ nm. The insets show the MOKE loops measured in the same samples.

Additionally, we acquired first order reversal curves (FORC) for nanodiscs having $R = 70$ nm and $T = 40$ nm, which provide information about the relative proportions of reversible and irreversible components of the magnetisation. A FORC is measured by saturating a sample, decreasing the field to a reversal field H_R, and then sweeping the field back to saturation in a series of regular field steps. This process is repeated for many values of H_R yielding a series of FORCs, and the measured magnetisations at each step give a filled hysteresis loop as shown in Figure 2.11*a*. In this case, we used the SQUID magnetometer, which provides the sensitivity and the speed required for this measurement. The FORC distribution $\rho\ (H_R, H)$, which is defined as a mixed second order derivative, can be plotted in coordinates of (H_B, H_C) on a three-dimensional plot (Figure 2.11*b*) or a contour map (Figure 2.11*c*), where H_C is the local coercive field, $H_C = (H - H_R) / 2$, and H_B is the bias field, $H_B = (H + H_R) / 2$.

The FORC diagrams, shown in Figures 2.11*b* and 2.11*c*, are characterized by three main features: two pronounced peaks at $H_C = 16$ mT and $H_B = \pm 40$ mT, corresponding to the vortex reversal process, and a ridge along $H_B = 0$ peaking at $H_C = 0$, which probably comes from badly patterned part of the sample as it happened with L30. In any case, the reversal of the magnetisation of nanodiscs having $R = 70$ nm and $T = 40$ nm clearly occurs via vortex state. This result can be contrasted with the FORC diagram of 52 nm Fe discs in single domain state measured by Dumas *et al.* [19], where the only predominant feature is a narrow peak along the local coercive field axis with zero bias. However, when increasing the diameter of the Fe discs to 67 nm, the lateral peaks appear indicating the transition from single-domain to vortex state. FORC measurements have been also performed to analyse the vortex reversal process in cobalt sub-micrometre discs [24].

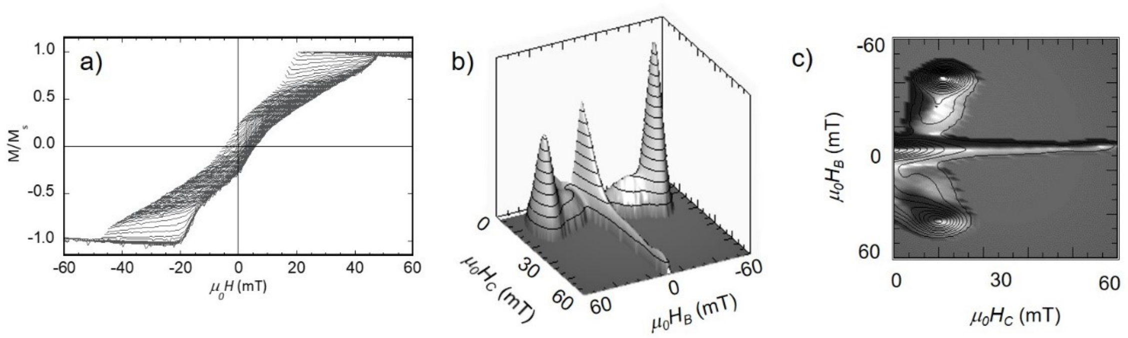

Figure 2.11. First order reversal curve measurements in nanodiscs with $R = 70$ nm and $T = 40$ nm. Series of FORCs (*a*) and the corresponding FORC distribution in a three-dimensional plot (*b*) and a contour map (*c*).

After assessing the magnetisation processes of the Permalloy nanodiscs, we proceeded to study the vortex core structure, including the radius and the out-of-plane component of the magnetisation, from the experimental and theoretical point of view.

2.1.2. Structure of the vortex core

In micrometre-sized discs, since the disc radius is much larger than the radius of the vortex core (R_c), the contribution of the out-of-plane magnetisation component can be neglected from the description of the overall magnetic behaviour of the disc [5, 25]. On the contrary, MFM images obtained[2] in the sample L50 ($R = 70$ nm and $T = 50$ nm) demonstrate that the radius of the vortex core is comparable to the radius of the disc.

Figure 2.12 reveals the initial magnetic state of three nanodiscs where the vortex cores can be clearly observed as black or white spots in the centre of the discs, depending if the magnetisation at the core points up or down. It is considerably challenging to obtain high-quality MFM images in such small structures. In this case, homemade Co coated tips were specifically prepared for these measurements to avoid modifications caused by the high stray fields coming from commercial MFM tips [26]. The measurements were performed in the amplitude modulation mode, oscillating 12 nm and with a typical retrace lift of 20 nm. A second feedback loop, phase lock loop (PLL), was enabled to keep the maximum amplitude and make the phase zero. The image shown in Figure 2.12 is clear enough to estimate the radius of the vortex core R_c to be about half of the disc radius: $R_c \sim 30$ nm.

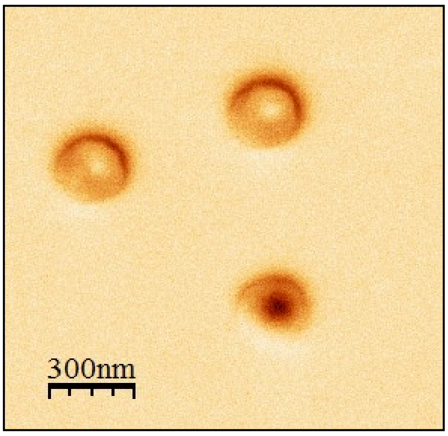

Figure 2.12. Magnetic force micrograph of $Ni_{80}Fe_{20}$ nanodiscs (nominal radius $R = 70$ nm and thickness $T = 50$ nm) at the initial magnetic state with the vortex cores at the centre of the discs pointing up or down (black or white).

---

[2] The MFM measurements were performed by Eider Berganza, Dr. Miriam Jaafar and Dr. Agustina Asenjo from the *Nanomagnetism and Magnetisation Processes group* at ICMM-CSIC, Madrid.

Additional MFM images were recorded under in-plane magnetic fields to monitor the displacement of the vortex core towards the edge of the disc. The images nicely correspond to the magnetic states revealed in the hysteresis loop as shown in Figure 2.13. At zero applied field, the vortex cores are centred, while the core moves towards the edge of the disc when a small field is applied, being the vortex core displacement perpendicular to the field direction. As it can be seen in the loop, the available fields are not enough to completely expel the vortex and go to a saturated in-plane configuration.

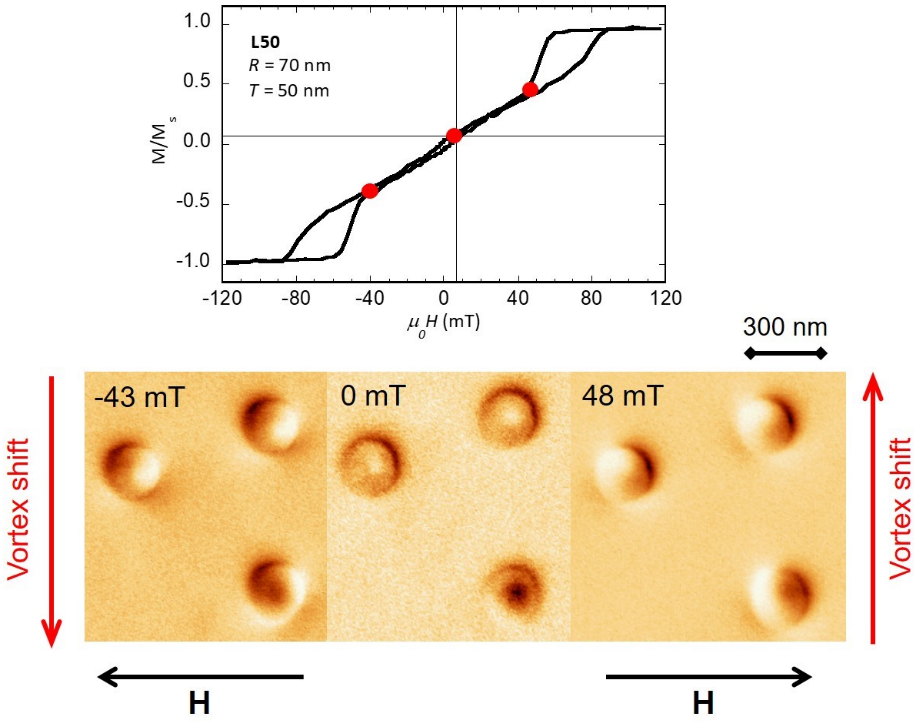

Figure 2.13. SQUID hysteresis loop of sample L50, with the imaged points marked by red dots and the corresponding MFM images under different *in situ* fields.

To complement the experimental results, we performed micromagnetic simulations in discs of the same geometries. Again, we used OOMMF software and the material parameters described previously except the cell size. Although, the usual cell size in this kind of simulations is 4 nm, we obtained the same results with smaller cell sizes. To increase the density of points in Figure 2.14, the data were obtained using cell sizes of 1 nm for samples S30 and S50 (R = 30 nm), and of 2 nm for L30 and L50 (R = 50 nm).

Particularly, we were interested in obtaining the configuration of the magnetisation in the ground state, at zero applied field, to analyse the structure of the vortex. Figure 2.14 represents the calculated out-of-plane component of the magnetisation m_z as a function of the radial coordinate ρ, measured from the centre of the disc (m_z is the reduced value of the magnetisation M_z/M_s, being M_s the saturation magnetisation). The actual magnetisation can be slightly different along the thickness of the disc, so Figure 2.14 represents, for each radial position, the value of m_z averaged along the disc thickness. In a classical magnetic vortex, the magnetisation is curled in the plain ($m_z = 0$), and only at the centre, in the vortex core, it points perpendicularly. In the results of Figure 2.14, the radius of the vortex core R_c can be identified as the radial coordinate where m_z vanishes, *i.e.*, $m_z(R_c) = 0$. The simulation results show that m_z can also be negative, indicating that the individual moments are not perfectly in-plane even out of the vortex core. The determination of the core size by the criteria $m_z = 0$ is therefore affected by some uncertainty that can be estimated by considering the magnitude of the negative m_z values, *i.e.*, we assume that the intersection points between $m_z = [m_z(\rho)]_{\min}$ and $m_z = - [m_z(\rho)]_{\min}$ with $m_z(\rho)$ delimit the core radius uncertainty range. That way, we can estimate the uncertainty in the determination of R_c to be about 3 to 6 nm. The values of R_c are compiled in Table 2.1. In any case, the simulation results clearly confirm that, in all the geometries, the vortex core extends up to a distance of the order of 30 nm from the disc centre. This is in very good agreement with the MFM results, at least for the discs with $R = 70$ nm, where MFM images could be obtained (Figure 2.12). The size of the vortex core R_c is comparable to radius of the disc R. This situation is denominated *large vortex core* (theoretically predicted before [25]), in contrast with the situation of negligibly small vortex core $R_c << R$, occurring in micrometre-sized discs, designated as *classical vortex*. What is definitively remarkable is that, for the small discs with radius $R = 30$ nm, the vortex core extends to the border of the disc. In the case of sample S50, the core seems to be even larger than the disc ($R_c > R$), which we call *extra-large vortex core*, but this situation does not prevent the existence of well-defined vortex-like reversal behaviour as evidenced in the hysteresis loops displayed in Figure 2.5. The colour profiles embedded in Figure 2.14 provide a descriptive illustration of the size and shape of the core of the vortex in the different discs. They correspond to the distribution of m_z values in the plane situated at half height of the discs.

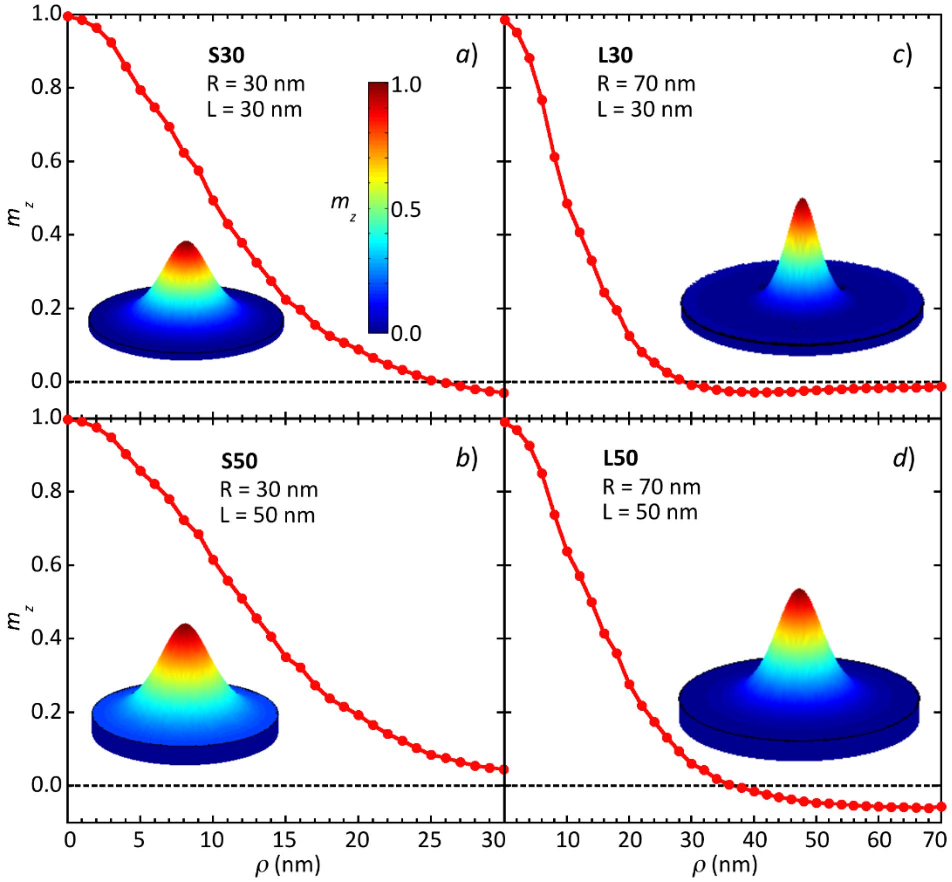

Figure 2.14. Radial dependence of the z-component of the magnetisation, obtained from micromagnetic simulations. The curves represent the value averaged over the thickness of the disc. The colour profiles are created from the m_z values in the plane situated at half height of the discs.

The magnetisation profiles represented in Figure 2.14 deserve a last remark. The negative values of m_z present in the samples S30, L30, and L50 recall the situation encountered in Bloch magnetic skyrmions [27] in which the magnetisation points in opposite directions between the core and the outer part of the structure. In this sense, the magnetisation configuration in the large vortex core discs appears to be evolving from a classical vortex to a situation that recalls a Bloch-skyrmion configuration (it should be reminded here that the latter is not supposed to be stable in Permalloy discs, with no Dzyaloshinskii-Moriya interaction and null perpendicular anisotropy [27]).

2.1.3. Model of magnetisation reversal in the large vortex case

The *large vortex core* situation encountered experimentally and confirmed by the simulation results, cannot be described within the analytical approach for the classical ($R_c \ll R$) vortex magnetisation reversal, developed in Ref. [5]. A revised theory is needed for sub 100 nm discs, where the vortex core is large compared with the size of the disc. Konstantin Guslienko, Ikerbasque Research Professor and author of the Ref. [5], accomplished this task and proposed a model that, among other results, gives an expression for the annihilation field H_{an} as a function of the parameter $c = R_c/R$ (the vortex core radius relative to the radius of the disc). This expression is convenient since H_{an} can be directly compared with experimental results. The main elements of the analytical approach are described below. The complete analysis is provided in Appendix B.

As the distances between the discs are much larger than their diameter for all the samples, it is assumed that the dipolar interdisc interaction is negligibly small in comparison with the in disc magnetic energies [28]. Therefore, the problem of the magnetisation reversal of a disc array is reduced to the problem of the magnetisation reversal of a single circular disc of given radius R and thickness T.

The magnetic energy density (per unit of the disc volume $V = \pi R^2 T$) can be written as

$$w = A(\nabla m_\alpha)^2 - \tfrac{1}{2}\mu_0 M_s \mathbf{m}\mathbf{H_m} + w_H \qquad (1)$$

where A is the exchange constant (which quantifies the strength of the magnetic interaction), $\alpha = x, y, z$, $\mathbf{m} = \mathbf{M}/M_s$ is the unit magnetisation vector, $\mathbf{H_m}$ is the magnetostatic field, and w_H is the Zeeman energy density in an in-plane magnetic field.

The different terms in (1) can be calculated (see Appendix B) for the case of $c = R_c/R > 1$ (*extra-large vortex core*) to obtain the energy $W(c, s, H)$ as a function of c, the position of the vortex core in the plane of the disc (represented by s in reduced coordinates) and the applied field H. The minimization of the energy $\partial W/\partial s = 0$ gives the equilibrium position s_0 of the vortex core for each applied field. The vortex annihilation field is then obtained as the field at which the position of the core equals the radius of the disc ($s_0 = 1$). The resulting expression is

$$H_{an}(c, \beta, R) = \tfrac{(1+c^2)}{2c}\kappa(c, \beta, R) M_s \qquad (2)$$

where $\beta = T/R$ is the aspect ratio of the disc and $\kappa(c, \beta, R)$ is the magnetic stiffness coefficient, whose complete expression is given in Appendix B, equation B4.

The expression in (2) is plotted as a function of c in Figure 2.15*a*, for the geometrical parameters corresponding to the sample S50 (R = 30 nm, T = 50 nm) and using a value for the saturation magnetisation $\mu_0 M_s$ = 0.75 T, assumed to be equal to the one measured in a thin film of the same composition.

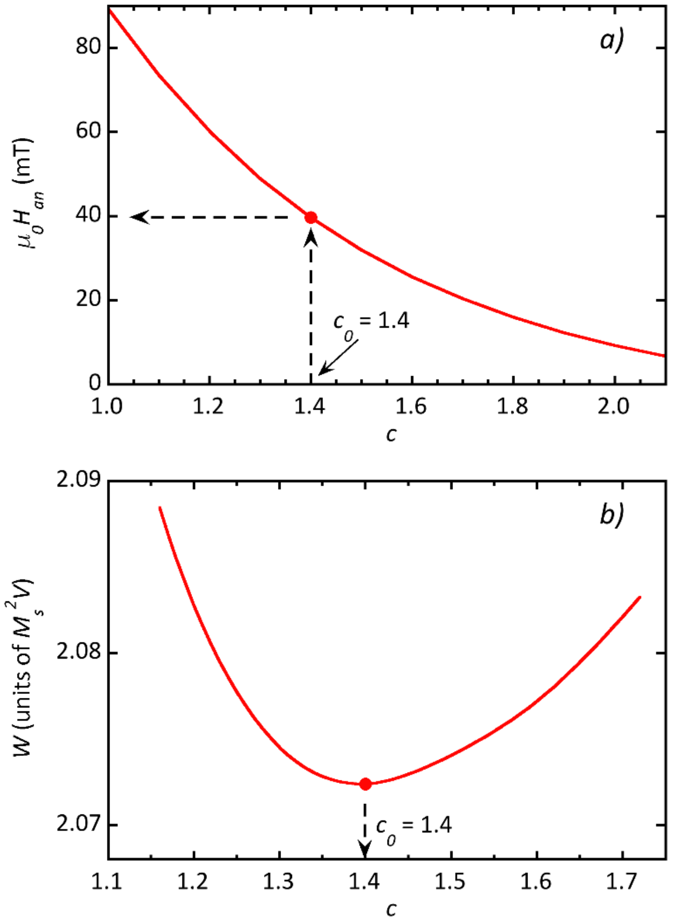

Figure 2.15. Evaluation of theory results using the data corresponding to sample S50: disc thickness T = 50 nm, radius R = 30 nm, $\mu_0 M_s$ = 0.75 T, $A = 1.3 \times 10^{-11}$ J m^{-1}. *a*) The vortex annihilation field as a function of the reduced vortex core radius *c*, calculated by equation 2 for the case $c > 1$. *b*) Magnetic energy calculated by equation 1. The equilibrium value of the vortex core radius c_0 is given by the minimum of the energy. This c_0 value determines the annihilation field for this case to be H_{an} = 40 mT, as shown in the upper plot (*a*).

On the other hand, the equilibrium vortex core radius c_0 can be found by minimizing the magnetic energy $\partial W/\partial c = 0$, calculated with the vortex core situated at the centre of the disc (s = 0). Figure 2.15*b* represents the dependence of $W(c)$ (calculated with the values corresponding to sample S50). The energy minimum corresponds to the equilibrium vortex core radius value of c_0 = 1.4. Using this value in the expression of the annihilation field (Eq. 2 and Figure 2.15a) we obtain H_{an} = 40 mT, in very good agreement with the measured result.

The analytical model for the classical magnetic vortex with $c \ll 1 (R_c \ll R)$, where the core radius is negligible, yields the expression [5]

$$H_{an} = [4\pi F_1(\beta) - (l_{ex}/R)^2]M_s, \tag{3}$$

where the function $F_1(\beta)$, defined in Appendix B, depends on the aspect ratio of the disc and the shape assumed for the vortex core within the rigid vortex model, and l_{ex} is the exchange length, related with the magnetic exchange stiffness constant.

The values of H_{an} obtained from (3) for the classic vortex ($c \ll 1$) are essentially larger than those obtained from Eq. (2) for the *extra-large vortex core* ($c > 1$). If the core of the vortex is smaller than the disc but is still large $c < 1$ equation (3) can be adapted as

$$H_{an}(c, \beta, R) = (1 - c)\lfloor 4\pi F_1(\beta) - (l_{ex}/R)^2 \rfloor M_s. \tag{4}$$

This is the expression that should be, in principle, applicable to samples S30, L30 and L50 which, according to the micromagnetic simulations, are in the case $c < 1$ $(R_c < R)$.

2.1.4. Comparison of the results

In this section, the *large vortex core* state discovered in discs of small radius is analysed by comparing the experimental results, the magnetisation profiles obtained by the micromagnetic simulations, and the predictions of the theory.

The calculated values obtained from equations (2) and (4) for the different samples, together with the experimental and simulated results, are compiled in Table 2.1. The dimensions of the discs are affected by some uncertainty (see Table 1.5, Chapter 1), so the theory column of Table 2.1 displays values for H_{an} and c calculated using sample parameters within those uncertainties.

Table 2.1. Compilation of the values of the reduced vortex radius ($c = R_c/R$) and annihilation field H_{an} obtained from magnetic measurements, micromagnetic simulations and analytical model.

sample	measured	simulation		theory[2]		vortex
	$\mu_0 H_{an}$ (mT)	R_c (nm)	$c = R_c/R$	$\mu_0 H_{an}$	c	type[3]
S30	23 ± 2	26 ± 3	0.7 ± 0.1	36 - 41	0.7 - 0.8	L
S50	40 ± 2	36[1]	1.2	40 - 41	0.8 - 1.4	XL/L
L30	63 ± 2	30 ± 4	0.4 ± 0.1	60 - 61	0.5 - 0.6	L
L50	84 ± 2	34 ± 6	0.5 ± 0.1	68 - 70	0.5 - 0.6	L

[1] approximate value obtained by extrapolation (Figure 2.14*b*).
[2] range of values obtained within sample size uncertainties (Table 1.5, Chapter 1).
[3] L = *large vortex core*. XL = *extra-large vortex core*.

For sample S30, equation (4) gives values between 36 and 41 mT, which are significantly larger than experimentally measured value of 23 mT. As explained before, the hysteresis loop of Figure 2.5*b* evidences that, although the general behaviour is typically vortex-like, the sample presents features of in-plane single domain state. This mixed behaviour limits the applicability of the analytical model. Alternatively, it is also possible that part of the discs of the sample were actually in in-plane single domain state, due to the closeness of the sample to the frontier in the phase diagram, producing in the measurement an average annihilation field H_{an} smaller than the one that the theory predicts.

The results for sample S50 agrees satisfactorily with the theory behind equation (2) for the *extra-large vortex* state in which the vortex core is larger than the disc itself ($c > 1$). However, if the inputs to the equation corresponding to the disc size are increased slightly (within the errors given in Table 1.5, Chapter 1), the *large vortex* state become energetically favourable, giving an equilibrium radius of $c_0 = 0.8$, and an annihilation field (using Eq. 4) of $H_{an} = 41$ mT, which is also close to the value measured experimentally. This means that the sample must possibly be close to the crossover from $c > 1$ (*extra-large vortex* state) to $c < 1$ (*large vortex* state). Incidentally, this also demonstrates the continuity between the results given by equation 4 for $c < 1$ and equation 2 for $c > 1$. In any case, the size of the vortex core in this sample S50 is significantly larger than those of the other studied samples. While being circularly curled, the magnetisation conserves a considerable z-component over the whole surface of the disc, which is definitely caused by the proximity the out-of-plane single domain region in the phase diagram. The *extra-large vortex core,* with its enhanced out-of-plane magnetisation component, makes that the reversal process occur with some coherent rotation of the magnetisation. This result reinforces the first theory we proposed in section 2.1.1 to explain the slanted hysteretic part of the sample S50: the magnetisation reversal takes place both via vortex state and via coherent rotation.

The samples with larger diameters, L30 and L50, are properly described in the *large vo*rtex ($c < 1$) framework represented by equation 4. Their calculated equilibrium vortex core radius is approximately half of the disc radius ($c_0 \sim 0.5$) in accordance to the experimental MFM measurements and simulated magnetisation profiles. The calculated value of the annihilation field for L30 is in rather good agreement with the experiment, whereas the calculated value for L50 is smaller than the measured one (which can be caused by the strong sensitivity of Eq. 2 and 4 to small variations of c).

Based on the above results, we can conclude that all the examined samples present a *large vortex core*, about 30 nm in radius, but the actual size of the core depends on the aspect ratio of the disc. The vortex becomes larger for thicker samples, as the sample approaches towards the out-of-plane single domain state (this is graphically observed in Figure 2.14, where the vortex core of samples S50 and L50 is larger than those of S30 and L30, respectively). In samples with a radius of 30 nm, the large vortex can result in the development of an *extra-large vortex core* state, which is proven to be an intermediate stable state between the *large vortex* ($c < 1$) and perpendicular single domain state ($c >> 1$). The magnetisation reversal process in this state can accurately be described by the theory that leads to equation 2, whereas the transition from the vortex state to the single domain state, maintaining the axial distribution of the magnetisation, was described theoretically in Ref. [29] and, in greater detail in Ref. [17]. The sample S50 (R = 30 nm, T = 50 nm), which is the one with the largest aspect ratio, is the closest to that *extra-large vortex* state. According to the analytical models, this sample is within the range of disc sizes where either the *large vortex* ($c < 1$) or the *extra-large vortex* ($c > 1$) can be stable (and the other one metastable) simultaneously.

From the point of view of applications, for fabricating small discs with a radius of R = 30 nm, the thickness of sample S50 (50 nm), is probably at the limit for presenting a well-defined vortex magnetisation reversal, before the out-of-plane single domain features dominate. On the other boundary, the thickness of sample S30 (30 nm) is probably the minimum possible for obtaining clear vortex behaviour without the dominance of the in-plane single domain reversal processes.

Despite the well-defined vortex state of the discs with R = 30 nm, we decided to use the larger discs with R = 70 nm for the experiments with cells. The main reason is that the bigger size of the discs eases the tracking of the fabrication process, using the SEM located in the Clean Room, as well as the observation of the further *in vitro* experiments by means of a fluorescent/brightfield microscope. In any case, before the experiments with cancer cells, it is essential to study the magnetic behaviour of the nanodiscs in water. As mentioned in the previous chapter, the experiments with cancer cells will be carried out in parallel using nanodiscs and microdiscs to compare the influence of the size on different aspects of the treatment. Thus, in the following section microdiscs 1 μm in radius are studied as well.

2.2. Behaviour of released discs

Static and dynamic measurements were carried out to examine the magnetic behaviour of the released discs. To assess the static behaviour, we used vibrating sample magnetometry (VSM), which gives us the hysteresis loops of the disc-shaped particles in water. These measurements were performed at the Cavendish Laboratory (University of Cambridge, UK) and the main features of the equipment are described in the Appendix A. The dynamic behaviour was studied through a magnetic field assisted light-transmission experiment. Additionally, we compared the force induced by a nanodisc and a microdisc using a simplified model.

2.2.1. Hysteresis loops

The nanodiscs, having R = 70 nm and T = 30 nm, exhibit a complex behaviour in water as reflected in the hysteresis loop of the Figure 2.16. The nanodiscs respond easily to the field, present large permeability and little remanence, however, at larger fields, they interact with each other and the loop presents hysteresis up to higher fields (~ 400 mT) comparing with the loop obtained with the same nanodiscs on the substrate having an annihilation field of ~ 63 mT (Figure 2.10a).

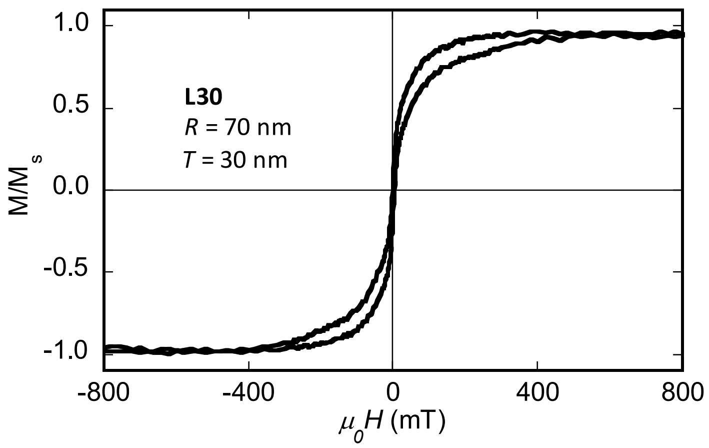

Figure 2.16. Hysteresis loop of $Ni_{80}Fe_{20}$ discs (R = 70 nm and T = 30 nm) in water.

To delve into the behaviour of the nanodiscs in the fluid, we froze the water with the well-dispersed nanodiscs (after 5 minutes of sonication) and repeated the VSM measurement. When no magnetic field is applied during the freezing process, the discs are fixed in random directions giving the hysteresis loop presented in Figure 2.17*a*. On the contrary, when applying a magnetic field of 1 T during the freezing process (Figure 2.17*b*), the centre of the loop is slightly narrowed and the coercive field is reduced getting closer to the characteristic shape of the vortex configuration. However, the alignment seems to be only partial.

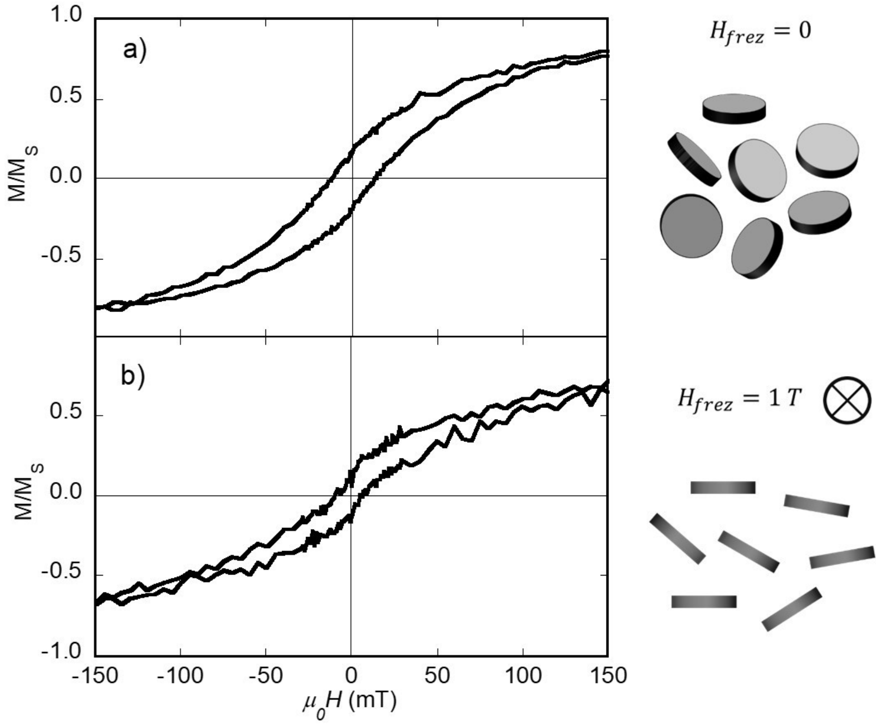

Figure 2.17. Hysteresis loop of $Ni_{80}Fe_{20}$ discs (R = 70 nm and T = 30 nm) after freezing the water. *a*) Freezing without applied magnetic field. *b*) Freezing under a magnetic field of 1 T.

The magnetisation curve of the microdiscs in water is presented in Figure 2.18. The loop displays the main features of the classical vortex configuration with zero remanence and open lobes at higher fields. Furthermore, it nicely fits with the hysteresis loop of a single microdisc measured by MOKE, having almost the same annihilation field value. For the MOKE measurement, the microdiscs were lifted-off from the wafer, cleaned with water and dried on a silicon substrate. This resemblance indicates that although the microdiscs are suspended in water, when the magnetic field is applied, they align with the field direction, so the vortex core shifts along the plane of the disc as it was attached to the substrate. This is in contrast with the behaviour of the nanodiscs in water (Figure 2.16), were they seem not to perfectly align with the magnetic field, probably due to the formation of small agglomerates, precluding the observation of a definite magnetisation reversal process.

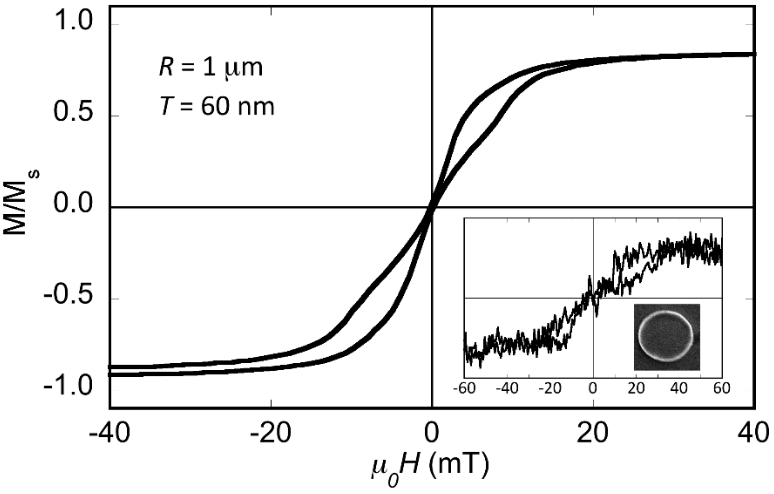

Figure 2.18. Hysteresis loop of $Ni_{80}Fe_{20}$ discs (R = 1 μm and T = 60 nm) suspended in water. The inset figure corresponds to the hysteresis loop of one microdisc measured by MOKE; the field is also given in mT.

2.2.2. Magneto-mechanical actuation

The mechanical responsiveness of the discs to an external magnetic field was determined by measuring the variation of the intensity of a laser beam ($\lambda = 670$ nm, red light) passing through the aqueous solution containing dispersed discs. The laser diode and the detecting photo-diode are the same ones used for the MOKE measurements. In this case, the field was created by a pair of calibrated Helmholtz coils. The experimental set-up is shown in Figure 2.19 accompanied by a schematic view.

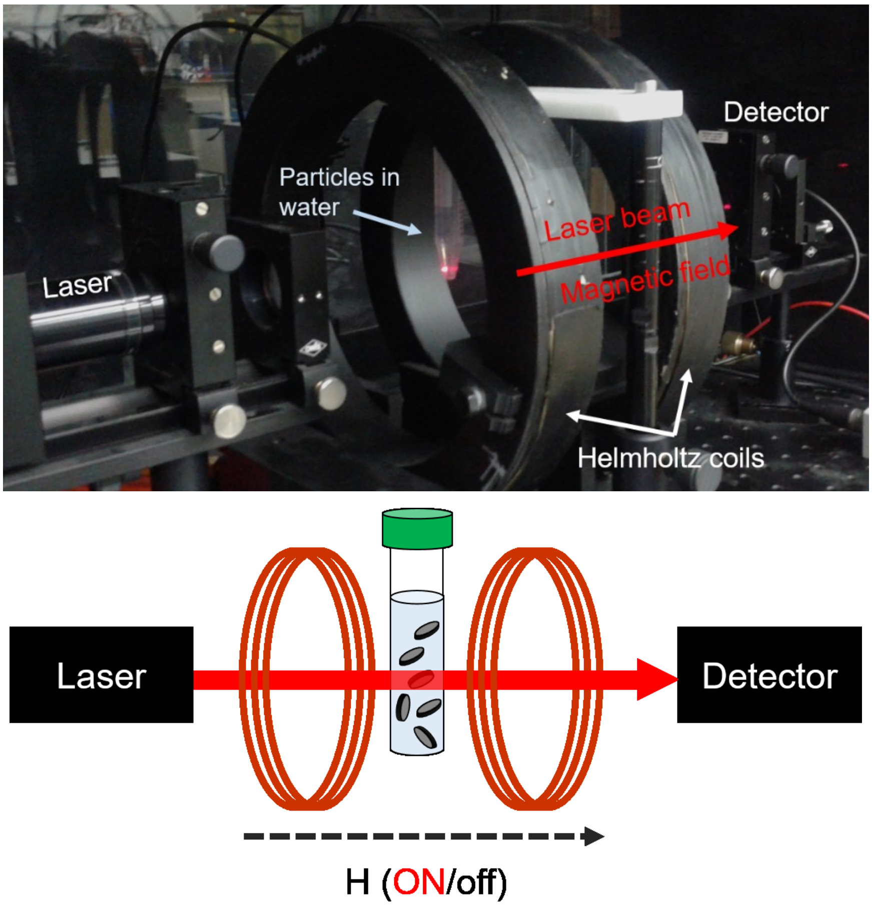

Figure 2.19. Light-transmission experiment to study the mechanical responsiveness of the discs to an external magnetic field.

The experiment consists in applying an intermittent magnetic field (t_{ON} and t_{off}) of 2 mT and 1 Hz and a continuous laser beam passing through the aqueous solution with discs, while the transmitted light intensity is being recorded. The magnetic field and the laser beam are in the same direction. The resulting plots, displayed in Figure 2.20, represent the transmitted light intensity and the applied magnetic field amplitude as a function of time. The dashed line represents the current in the Helmholtz coils, *i.e.*, the magnetic field, being the t_{ON} period highlighted with pink bars.

The response of the nanodiscs and the microdiscs is similar: the transmitted light reaches the maximum intensity when the magnetic field is on, and drops when switched off. This result can be interpreted as the alignment of the plane of the discs with the magnetic field, which allows the light to pass through the aqueous solution and reach the detector, as schematically described in Figure 2.21*a*. However, the relaxation time (t_R) of the microdiscs is clearly larger than the nanodiscs'. We performed the same experiment with spherical Fe_3O_4 particles of 35 nm where the transmitted light should not suffer abrupt changes since the spheres do not have any preferential geometrical orientation with the applied field (Figure 2.21*b*). Nevertheless, as observed in Figure 2.22*a*, the nanoparticles showed a response similar to that of the discs, suggesting that not only the orientation of the discs is occurring. This result suggests the formation of particles chains parallel to the magnetic field as depicted in Figure 2.21*c*.

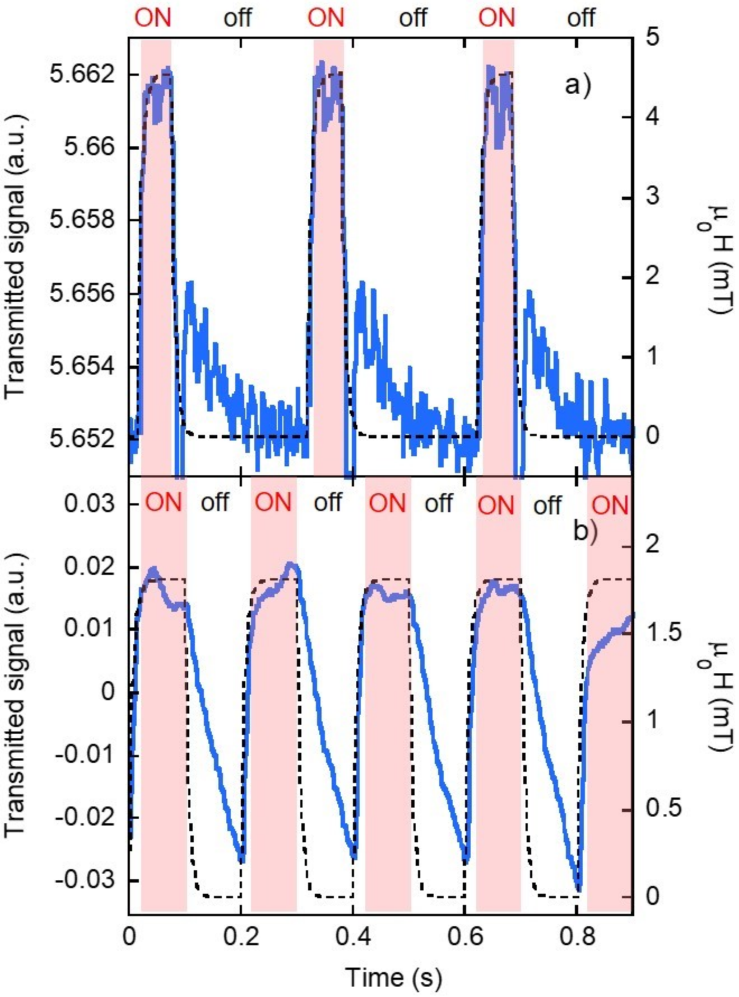

Figure 2.20. Intensity of the transmitted light, under a pulsed magnetic field, when passing through an aqueous solution with (*a*) nanodiscs ($R = 70$ nm and $T = 50$ nm) and (*b*) microdiscs ($R = 1$ μm and $T = 60$ nm).

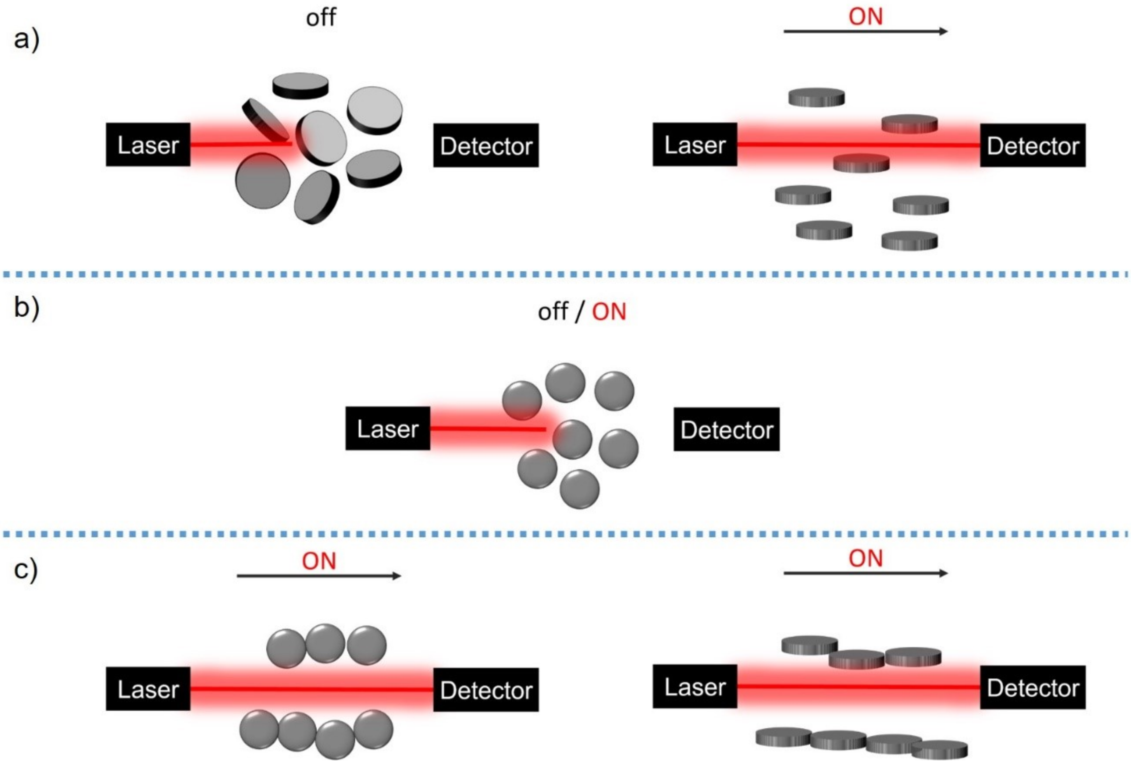

Figure 2.21. Schematic description of the light-transmission experiment. *a*) Initial assumption of the discs' response: during t_{off}, the discs are randomly oriented blocking the light; when t_{ON}, the plane of the discs aligns parallel with the field and the light reaches the detector. *b*) Initial assumption of the spherical nanoparticles' response: the distribution of the particles is the same whether t_{ON} or t_{off}, the light does not reach the detector. *c*) Real response of the particles: the spherical particles form chains allowing the light to pass and so do the disc-shaped particles.

If we allow the particles to relax after the application of the magnetic field, extending t_{off}, the relaxation time (t_R) difference between the nanodiscs and the microdiscs, observed in Figure 2.20, becomes much more visible, as can be seen in Figure 2.22. When the field is switched off, the microdiscs seem to remain forming chains, whereas the nanodiscs, as well as the spherical nanoparticles, relax immediately and are dispersed in the aqueous solution. The strong chaining of the microdiscs can be explained through a self-polarization phenomenon as suggested by S. Leulmi *et al.* [30]. Indeed, if the particles susceptibility is too large, the stray field created by all neighbouring microdiscs on a given one when they are aligned in chain after field application, may maintain a microdisc net polarization even when the applied field is switched off. The self-polarization effect favours the agglomeration of the microdiscs, which is a major drawback for their use in biomedical applications. Hence, this result evidences the great importance of the particle size; the smaller the disc, the better the dispersion in solution.

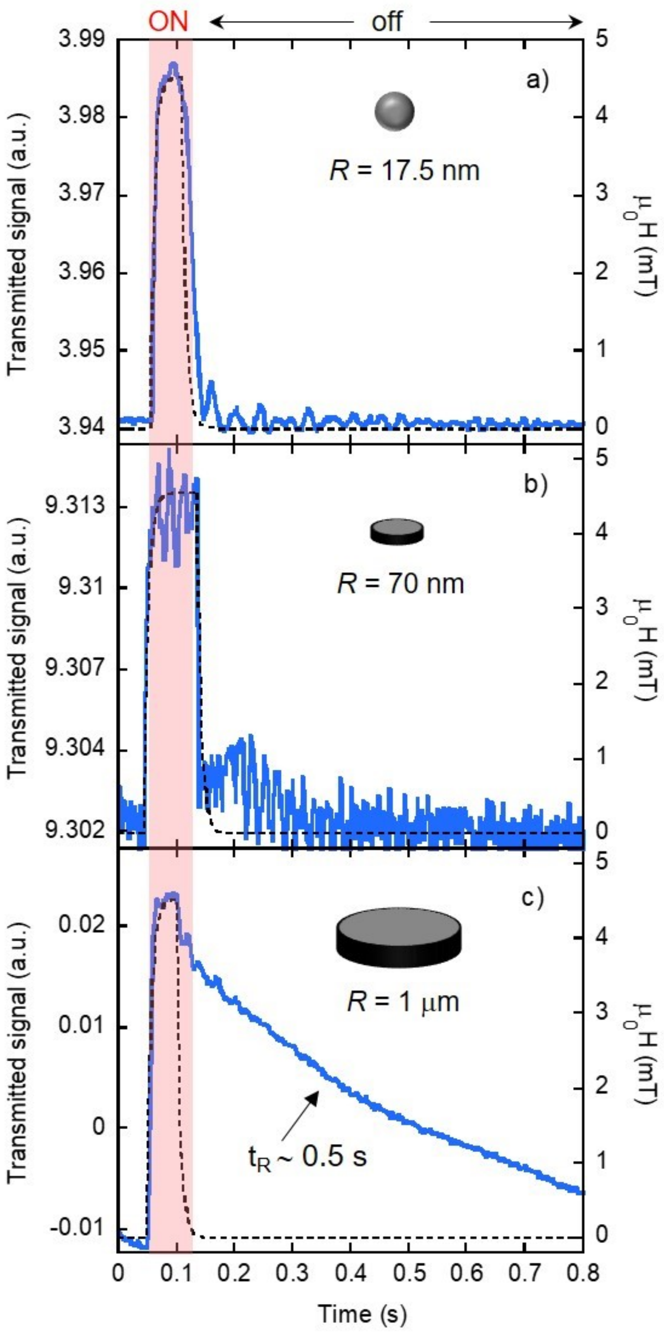

Figure 2.22. Relaxation time of (*a*) spherical Fe_3O_4 nanoparticles, (*b*) $Ni_{80}Fe_{20}$ nanodiscs and (*c*) microdiscs in water after the application of the magnetic field.

2.2.3. Calculation of the force

Finally, we estimated the force that the Permalloy nanodiscs and microdiscs can exert on the cancer cells following the simplified model proposed by D-H. Kim *et al*. [31].

The dynamic equation of motion can be written in terms of the magnetic torque, the drag force, the restoring force and the acceleration, as follows:

$$\mathbf{m}\cdot\mathbf{H}-\beta V\eta\,\frac{d\propto}{dt}-k\propto=I\,\frac{d^2\propto}{dt^2} \tag{5}$$

where $\mathbf{m}$ is the magnetic moment of the disc, $\mathbf{H}$ the applied magnetic field, β the disc shape factor, V the disc volume, η the intracellular viscosity, $\propto$ the disc deflection angle, k the cancer cell stiffness and I is the disc moment of inertia. The magnetic torque can be calculated as:

$$\tau = mHsin\alpha \tag{6}$$

where, m is the total induced magnetic moment per disc, H is the applied magnetic field and α is the angle between the plane of the disc and the applied magnetic field as it is illustrated in Figure 2.23.

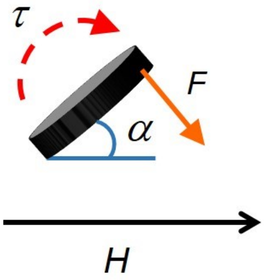

Figure 2.23. Mechanical torque (τ) of a vortex state disc, with an angle α between its plane and the direction of the applied field (*H*), generating a force (*F*).

The total induced magnetic moment per disc can be calculated as follows:

$$m = M_S V (M/M_S)_{H,\alpha} \tag{7}$$

where M_S is the saturation magnetisation for Permalloy ($8\cdot10^5\,\mathrm{A\,m^{-1}}$) and $(M/M_S)_{H,\alpha}$ is the in-plane component of the reduced magnetisation induced by the field H with an angle α. In the experiments with cells, the angle α ranges between 0-90°; we will use an angle of 45° to calculate the torque. The magnetic field applied in our assays is 10 mT. With these values, the in-plane component of the magnetisation can be found in the hysteresis loops as indicated in Figure 2.24. The resulting torque and force ($F = \tau/R$) for the nanodiscs, with $R = 70$ nm and $T = 50$ nm, and for the microdiscs, with $R = 1$ μm and $T = 60$ nm, are collected in Table 2.2.

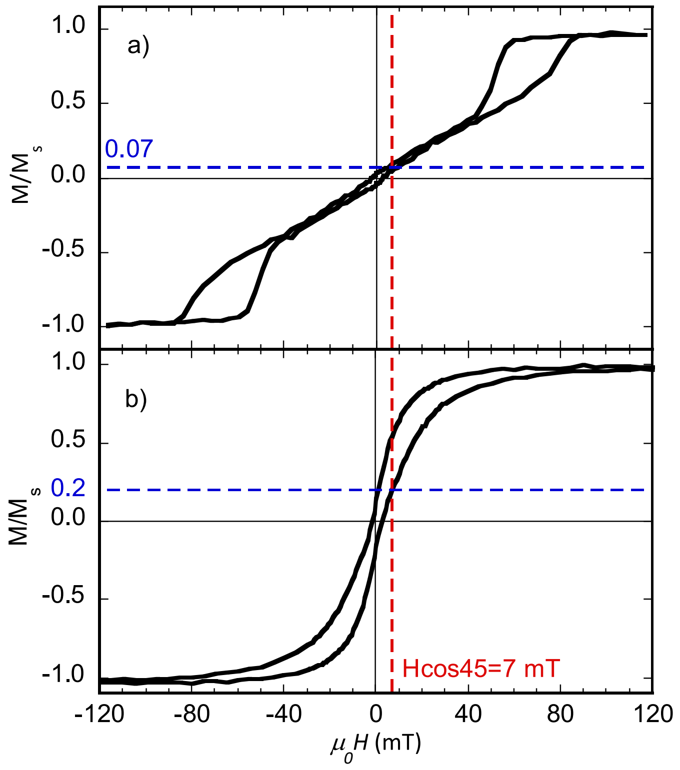

Figure 2.24. Hysteresis loops of $Ni_{80}Fe_{20}$ (*a*) nanodiscs (*R* = 70 nm and *T* = 50 nm) and (*b*) microdiscs (*R* = 1 μm and *T* = 60 nm). The microdiscs were measured by VSM after lifted-off from the wafer, cleaned with water and dried on a silicon substrate.

Table 2.2. Results of the calculations of the forces that can exert Permalloy nanodiscs with *R* = 70 nm and *T* = 50 nm and microdiscs with *R* = 1 μm and *T* = 60 nm.

	V (m³)	$M/M_S{}^1$	m (Am²)	τ (Nm)	F (pN)
Nanodiscs	$7.7 \cdot 10^{-22}$	0.07	$4.7 \cdot 10^{-17}$	$3.3 \cdot 10^{-19}$	4.7
Microdiscs	$1.9 \cdot 10^{-19}$	0.2	$3.0 \cdot 10^{-14}$	$2.1 \cdot 10^{-16}$	210

[1]for *H* = 10 mT and α = 45°.

According to the calculations, the forces that can be induced by a nanodisc with *R* = 70 nm are on the order of piconewtons, whereas the microdiscs with *R* = 1 μm can exert forces of the order of hundreds of piconewtons. This is in good agreement with the forces calculated for microdiscs having *R* = 0.5 μm, that are in the range of tens of piconewtons [31]. Based on the results, the microdiscs should exhibit a larger capability to disrupt the integrity of cancer cells comparing with the nanodiscs. This theoretical prediction was experimentally assessed by *in vitro* assays presented in the next chapter.

References

[1] J. M. D. Coey, “Magnetism and Magnetic Materials”, *Cambridge University Press*, 2010.

[2] W. F. Brown, “The fundamental theorem of fine-ferromagnetic-particle theory”, *Journal of Applied Physics*, vol. 39, pp. 993, 1968.

[3] R. P. Cowburn, D. K. Koltsov, A. O. Adeyeye, M. E. Welland and D. M. Tricker, “Single-Domain Circular Nanomagnets”, *Physical Review Letters*, vol. 83, pp. 1042-5, 1999.

[4] W. Scholz, K. Guslienko, V. Novosad, D. Suess, T. Schrefl, R. Chantrell and J. Fidler, “Transition from single-domain to vortex state in soft magnetic cylindrical nanodots”, *Journal of Magnetism and Magnetic Materials*, vol. 266, pp. 155-163, 2003.

[5] K. Y. Guslienko, V. Novosad, Y. Otani, H. Shima and K. Fukamichi, “Magnetization reversal due to vortex nucleation, displacement, and annihilation in submicron ferromagnetic dot arrays”, *Physical Review B*, vol. 65, 024414, 2001.

[6] X. M. Cheng and D. J. Keavney, “Studies of nanomagnetism using synchrotron-based x-ray photoemission electron microscopy (X-PEEM)”, *Reports on Progress in Physics*, vol. 75, pp. 026501, 2012.

[7] I. Eisenstein and A. Aharoni, “Magnetization curling in a sphere”, *Journal of Applied Physics*, vol. 47, pp. 321, 1976.

[8] N. A. Usov and S. E. Peschanny, “Magnetization curling in a fine cylindrical particle”, *Journal of Magnetism and Magnetic Materials*, vol. 118, pp. L290-L294, 1993.

[9] A. Hubert and R. Schäfer, “Magnetic Domains”, *Springer*, 1998.

[10] T. Shinjo, T. Okuno, R. Hassdorf, K. Shigeto and T. Ono, “Magnetic Vortex Core Observation in Circular Dots of Permalloy”, *Science*, vol. 289, pp. 930-2, 2000.

[11] -V. Jausovec, G. Xiong and R. P. Cowburn, “Cycle-by-cycle observation of single-domain-to-vortex transitions in magnetic nanodisks”, *Applied Physics Letters*, vol. 88, pp. 052501-3, 2006.

[12] V. Novosad, K. Yu. Guslienko, H. Shima, Y. Otani, S. G. Kim, K. Fukamichi, N. Kikuchi and O. Kikatami, “Effect of interdot magnetostatic interaction on magnetization reversal in circular dot arrays”, *Physical Review B*, vol. 65, pp. 060402, 2002.

[13] M. Schneider, H. Hoffmann, and J. Zweck, “Lorentz microscopy of circular ferromagnetic permalloy nanodisks”, *Applied Physics Letters*, vol. 77, pp. 2909, 2000.

[14] A. Wachowiak, J. Wiebe, M. Bode, O. Pietzsch, M. Morgenstern and R. Wiesendanger, “Direct Observation of Internal Spin Structure of Magnetic Vortex Cores”, *Science*, vol. 298, pp. 277-3, 2002.

[15] E. K. Semenova, F. Montoncello, S. Tacchi, G. Dürr, E. Sirotkin, E. Ahmad, M. Madami, G. Gubbiotti, S. Neusser, D. Grundler, F. Y. Ogrin, R. J. Hicken, V. V. Kruglyak, D. V. Berkov, N. L. Gorn and L. Giovannini, “Magnetodynamical response of large-area close-packed arrays of circular dots fabricated by nanosphere lithography”, *Physical Review B*, vol. 87, pp. 174432-19, 2013.

[16] S-H. Chung, R. D. McMichael, D. T. Pierce and J. Unguris, “Phase diagram of magnetic nanodisks measured by scanning electron microscopy with polarization analysis”, *Physical Review B*, vol. 81, pp. 024410, 2010.

[17] K. L. Metlov and K. Y. Guslienko, “Stability of magnetic vortex in soft magnetic nano-sized circular cylinder”, *Journal of Magnetism and Magnetic Materials*, vol. 242–245, pp. 1015–7, 2002.

[18] C. A. Ross, M. Hwang, M. Shima, J. Y. Cheng, M. Farhoud, T. A. Savas, Henry I. Smith, W. Schwarzacher, F. M. Ross, M. Redjdal and F. B. Humphrey, “Micromagnetic behavior of electrodeposited cylinder arrays”, *Physical Review B*, vol. 65, pp. 144417, 2002.

[19] R. K. Dumas, C.-P. Li, I. V. Roshchin, I. K. Schuller and K. Liu, “Magnetic fingerprints of sub-100 nm Fe dots”, *Physical Review B*, vol. 75, pp. 134405-5, 2007.

[20] I. V. Roshchin, C-P. Li, H. Suhl, X. Batlle, S. Roy, S. K. Sinha, S. Park, R. Pyn, M. R. Fitzsimmons, J. Mejía-López, D. Altbir, A. H. Romero and I. K. Schuller, “Measurement of the vortex core in sub-100 nm Fe dots using polarized neutron scattering”, *Europhysics Letters*, vol. 86, pp. 67008-5, 2009.

[21] M. Goiriena-Goikoetxea, A. García-Arribas, M. Rouco, A. V. Svalov and J. M. Barandiaran, “High-yield fabrication of 60 nm Permalloy nanodiscs in well-defined magnetic vortex state for biomedical applications”, *Nanotechnology*, vol. 27, pp. 175302, 2016.

[22] J. Mejía-López, D. Altbir, P. Landeros, J. Escrig, A. H. Romero, I. V. Roshchin, C.-P. Li, M. R. Fitzsimmons, X. Battle and I. Schuller, “Development of vortex state in circular magnetic nanodots: Theory and experiment”, *Physical Review B*, vol. 81, pp. 184417, 2010.

[23] M. J. Donahue and D. G. Porter, 1999 OOMMF user guide, version 1.0 Interagency Report NISTIR 6376 National Institute of Standards and Technology, Gaithersburg, MD Available at (http://math.nist.gov/oommf) Accessed: 22 September 2015

[24] C. Pike and A. Fernandez, “An investigation of magnetic reversal in submicron-scale Co dots using first order reversal curve diagrams”, *Journal of Applied Physics*, vol. 85, pp. 6668-6676, 1999.

[25] K. L. Metlov, “Vortex precession frequency and its amplitude-dependent shift in cylindrical nanomagnets”, *Journal of Applied Physics*, vol. 113, pp. 223905, 2013.

[26] O. Iglesias-Freire, M. Jaafar, E. Berganza, A. Asenjo and Beilstein, “Customized MFM probes with high lateral resolution”, *Journal of Nanotechnology*, vol. 7, pp. 1068-1074, 2016.

[27] K. Y. Guslienko, “Skyrmion State Stability in Magnetic Nanodots With Perpendicular Anisotropy”, IEEE Magnetics Letters, vol. 6, pp. 4000104, 2015.

[28] A. A. Awad, G. R. Aranda, D. Dieleman, K. Y. Guslienko, G. N. Kakazei, B. Ivanov and F. Aliev, “Spin excitation frequencies in magnetostatically coupled arrays of vortex state circular Permalloy dots”, *Applied Physics Letters*, vol. 97, pp. 132501, 2010.

[29] K. Y. Guslienko and V. Novosad, “Equilibrium large vortex state in ferromagnetic disks”, *Journal of Applied Physics*, vol. 96, pp. 4451, 2004.

[30] S. Leulmi, H. Joisten, T. Dietsch, C. Iss, M. Morcrette, S. Auffret, P. Sabon and B. Dieny, “Self-polarization phenomenon and control of dispersion of synthetic

antiferromagnetic nanoparticles for biological applications", *Applied Physics Letters*, vol. 97, pp. 253112, 2010.

[31] D-H. Kim, E. A. Rozhkova, I. V. Ulasov, S. D. Bader, T. Rajh, M. S. Lesniak and V. Novosad, "Biofunctionalized magnetic-vortex microdiscs for targeted cancer-cell destruction", *Nature Materials*, vol. 9, pp. 165–171, 2010.

3

Cancer cell destruction

Cancer is one of the biggest challenges facing the medical research in our time. Encouragingly, thanks to intensive efforts within the last 50 years, significant progress has been made confronting cancer, which gave rise to three main therapies that are currently being used clinically: surgery, radiotherapy, and chemotherapy. However, none of them is strictly tumour-cell specific, leading to substantial damage to healthy tissues and organs and limiting the therapeutic dose. These adverse effects often affect patients more than the disease itself. The initial approach certainly consists of improving the existing methods and/or combining them with new procedures. The long-term goal is to achieve a cancer therapy that is simple, cost-effective, and well tolerated [1].

According to the estimates by the US National Cancer Institute, nanotechnology will prove to be trailblazing in future prevention, diagnosis, and treatment of cancer. Although a wide variety of materials are being used in medicine, magnetic nanoparticles, and especially superparamagnetic iron oxide nanoparticles (SPIONs), seem to hold the greatest potential of success. They are already established in clinical use as contrast agent for magnetic resonance imaging (MRI) (commercial names: Resovist® and Sinerem®). In addition, these particles can be guided non-invasively (to act as drug delivery agents) and have the ability to be heated by external magnetic fields (for magnetic hyperthermia treatments) [1].

Magnetic hyperthermia is certainly one of the oldest forms of cancer therapy. Experimental investigations of the application of magnetic materials for hyperthermia date back to 1957 [2]. Since then, there have been numerous publications describing a variety of schemes using different types of magnetic materials, different field strengths and frequencies and different methods of encapsulation and delivery of the particles [3-7]. In broad terms, the procedure involves dispersing magnetic particles throughout the target tissue, and then applying an AC magnetic field of sufficient strength and frequency (typically of the order of hundreds of kHz) to cause the particles to heat. This heat conducts into the immediately surrounding diseased tissue whereby, if the temperature can be maintained above the therapeutic threshold of 42 °C for 30 min or more, the cancer cells are destroyed [8].

A novel route to destroy cancer cells appeared in the year 2010 along with the publication of the work developed by D-H Kim *et al.* [9]. They used $Ni_{80}Fe_{20}$ particles (1 μm in diameter) with disc-shape and vortex magnetic configuration, that under an AC field as small as 9 mT and 10 Hz, were able to oscillate and damage the integrity of cancer cells to which they were attached. In principle, since there is no heat generation, it is claimed that the magneto-mechanical actuation avoids the risk of damaging the surrounding healthy tissue as it can occur in magnetic hyperthermia. Moreover, it has been proposed that the mechanical force delivered by the discs leads to the apoptosis of the cells instead of the more likely necrotic pathway caused by heating. Apoptosis is the programmed spontaneous cell death, where, at the latest stage, the dead cells are phagocytized by macrophages. Consequently, there should not be any cell-leakage in the surrounding extracellular environment, avoiding inflammatory reactions, in contrast to necrosis [10]. In the light of the promising results achieved with the magneto-mechanically actuated discs, several works have been published in the last 6 years aiming the optimization of this new form of cancer therapy. The main advances reported consist on the implementation of magneto-mechanical actuation from $Ni_{80}Fe_{20}$ microdiscs *in vivo* [11], the development of a rotating magnetic field system to improve the efficiency of the microdiscs torque [12] and the introduction of antiferromagnetic-like CoFeB/Pt microdiscs that exhibit large magneto-mechanical actuation capability [13]. However, none of them has addressed the challenge of reducing the size of the discs down to the nanoscale, which would definitely favour the internalization by the cells.

We studied the interaction of Permalloy nanodiscs (R = 70 nm and T = 50 nm) and microdiscs (R = 1 μm and T = 60 nm) with human lung cancer cells.

As explained in Chapter 1, the nanodiscs were covered with 3-4 nm of gold whereas the microdiscs were covered with either gold or titanium, 5 nm thick, to enhance the biocompatibility. The uptake of the discs by the cells, their cytotoxicity effect and the magneto-mechanical capability were assessed in a comparative study. To the best of our knowledge, the experiments performed in this Thesis are the first ones in the bibliography using vortex state nano-sized discs (down to 70 nm in radius) in contact with a biological system. In this part of the Thesis, we worked closely with David Muñoz and Dr. Alicia Muela from the *Immunology, Microbiology and Parasitology Department* of the University of the Basque Country (UPV/EHU).

3.1. Tuning of the *in vitro* assays

We approached this comparative study from a qualitative point of view, meaning that we were interested in the direct observation of the discs-cells interaction. Therefore, the results of the *in vitro* assays were evaluated mainly by fluorescence/brightfield microscopy, allowing us to check the influence of the discs cell by cell. First, the cell culture and manipulation procedures had to be adequate to fit into this microscopy-based examination technique. The adjustment implied the optimization of the culture conditions, the growth of cells directly on coverslips and the standardization of a cell viability assay. As a result, we fixed the following protocol, summarized in Figure 3.1:

0. Cell culture

The experiments were conducted on human lung carcinoma cells, A549 cell line (American Type Culture Collection, CCL-185). The cell line was propagated in a humidified atmosphere (95 % relative humidity) and 5 % CO_2, at 37 °C in RPMI-based medium (acronyms of Roswell Park Memorial Institute) supplemented with 2 mM L-glutamine and 10 % heat-inactivated foetal bovine serum and a mixture of antibiotics (100 μg/mL penicillin and 100 μg/mL streptomycin) and antimycotics (0.25 μg/mL amphotericin B).

1. Cell detachment

The A549 lung carcinoma cells grow as monolayers adhered to the culture flask. To detach them, the culture medium is removed and 1 ml of a mixture of PBS (phosphate buffered saline) and EDTA (ethylenediaminetetraacetic acid) is added to the flask. After 5 min in the incubator at 37 °C and 5 % CO_2, the cells are released by lightly tapping the flask.

2. Cell harvest

The detached cells are harvested by centrifugation at 1200 rpm for 1 min. The supernatant is removed and replaced with 2 ml of fresh medium. The pellet of cells is re-suspended by carefully pumping with a pipette.

3. Cell counting

Cell counting was performed with a Neubauer chamber. The cell suspension is mixed 1:1 with Trypan Blue, a vital stain that only dyes the dead cells. A drop of 10 μl of the dyed mixture is placed on the counting chamber and the total and dead cells are systematically counted. With these results, the concentration of live cells is calculated. Finally, the cell suspension is diluted with fresh medium to reach a working concentration of 2×10^5 cells/ml.

4. Cell seeding

Coverslips (12 mm in diameter), sterilized by heating at 200 °C for 2 h, are placed in 24-well plate (one coverslip per well). Then, 0.5 ml of the working cell suspension are seeded in each well and the plate is incubated for 2 h, so that the cells are attached to the coverslips.

5. Cell internalization of nanodiscs/microdiscs

The discs are collected at the bottom of the tube, where they were transferred after being released from the substrate, using a NdFeB permanent magnet, so that we can replace the water with culture medium and adjust the concentration to that desired for each assay. The discs suspension is sonicated for 5 min and subsequently added to the wells in a given proportion which is of the order of tens of microdiscs per cell or thousands of nanodiscs per cell. Control wells without discs are also prepared. The plate is incubated at 37 °C in 5 % CO_2 for 24 h. Then, the excess of discs, *i.e.*, the discs non-internalized by the cells, is removed and the wells are washed with PBS three times. In the case of the evaluation of discs' cytotoxicity, the cell viability is assessed straight away.

6. Magneto-mechanical actuation

In the case of the magneto-mechanical actuation, 0.5 ml of fresh medium is added to the wells and AC magnetic field is applied. The cell viability is assessed 1-4 h after the application of the magnetic field.

7. Cell viability assessment

For assessing the viability of the cells, a two-colour nuclear staining assay was performed. NucBlue® live reagent stains the nuclei of all the cells whereas propidium iodide (PI) only stains the nuclei of dead cells. The staining conditions were optimized through a trial-and-error process, which included the selection of the stains, the determination of their concentration and volume and the technical aspects of the staining process. Eventually, the procedure was fixed as follows: *(i*) supernatant removal and addition of 0.5 ml of PBS to the wells, (*ii*) addition of a drop of propidium iodide (PI) and another drop of NucBlue® to each well, (*iii*) 15 min of incubation in darkness, (*iv*) removal of the coverslip from the well using tweezers and washing in PBS and (*v*) placing the coverslip on the glass slide with the adhered cells contacting the plate. Then, the slide is examined under fluorescent/brightfield microscope (NucBlue®, excitation/emission 360/460 nm, is detected through a DAPI -diamidino phenylindole- standard filter set and PI, excitation/emission 535/617 nm, is detected through a TRITC –tetramethylrhodamine isothiocyanate- standard filter set). At the same time, the sample can be examined using the brightfield mode of the microscope, which allows us to see the position of the nanodiscs/microdiscs (whether they are outside or inside the cells) and even to count them.

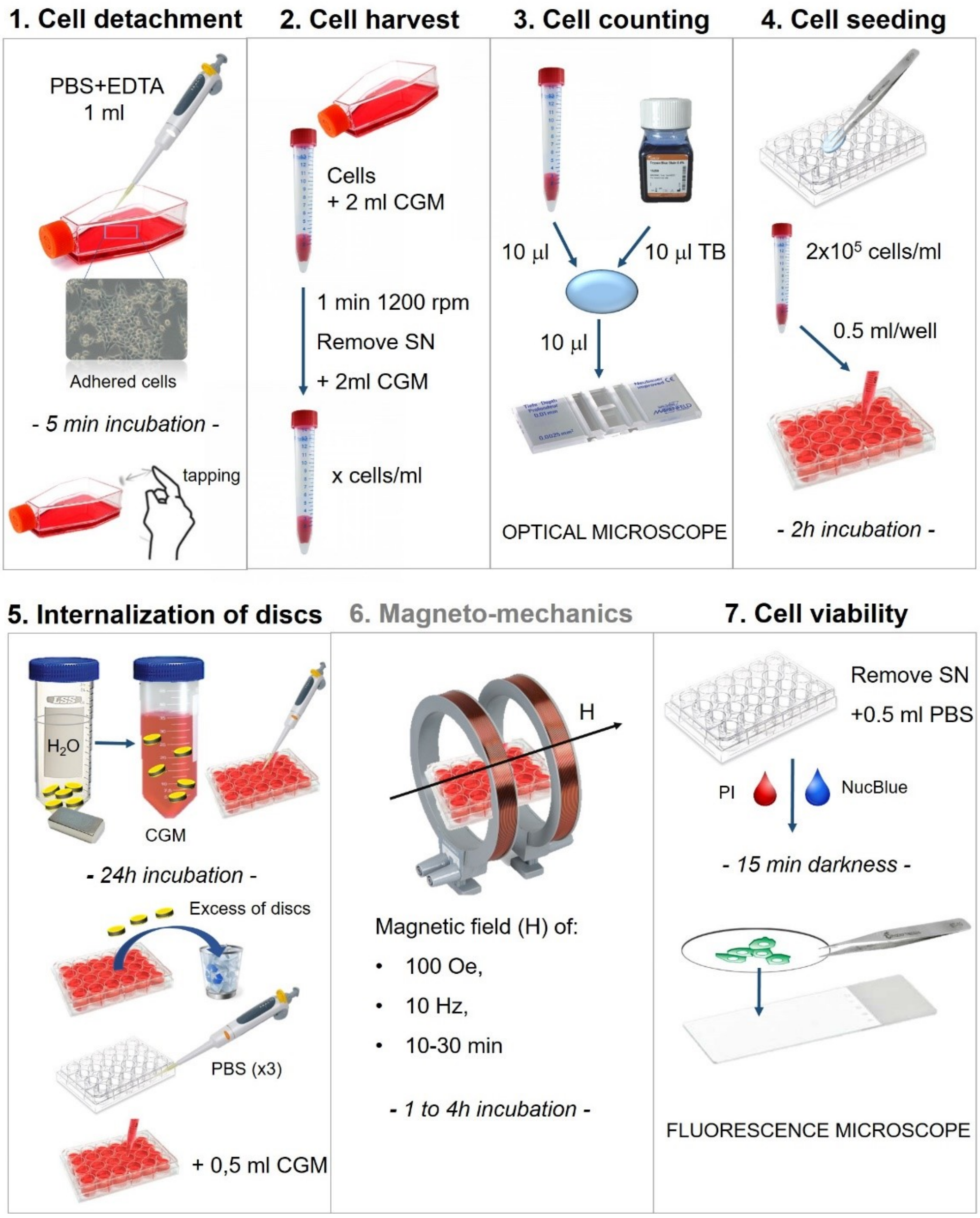

Figure 3.1. Protocol of the *in vitro* assays, from the preparation of the cells (steps 1-4) and the treatment (steps 5 and 6) to the cell viability assessment (step 7).
CGM: cell growth medium, SN: supernatant.

All of the assays described hereafter, were performed testing the microdiscs first because, as they have already been studied, there are some reference conditions in the literature that are helpful to initiate the experiments.

3.2. Intracellular uptake of discs

To study the internalization of the discs by the cells, images were captured by fluorescence/brightfield microscopy and, more accurately, by transmission electron microscopy (TEM). Additionally, we recorded live cell videos over 48 h to monitor the interaction of the discs with the cells. The fundamentals of techniques and the features of each device are described in Appendix A.

Even though the discs were not functionalized to ease the internalization by the lung carcinoma cells, the optical micrographs suggest that nanodiscs and even the microdiscs enter into the cells. As mentioned in the point 6 of the protocol, the wells were thoroughly washed with PBS ensuring the removal of the non-internalized discs. Moreover, the images were captured focusing on different layers of the cell, from the bottom to the top. Hence, we were able to observe whether the discs were actually in the inner layers. For instance, in Figure 3.2*a* the top layer is focused (*i.e.*, the cell surface), whereas in Figure 3.2*b*, a deeper layer is focused, where some nanodiscs appear inside the cell on the right.

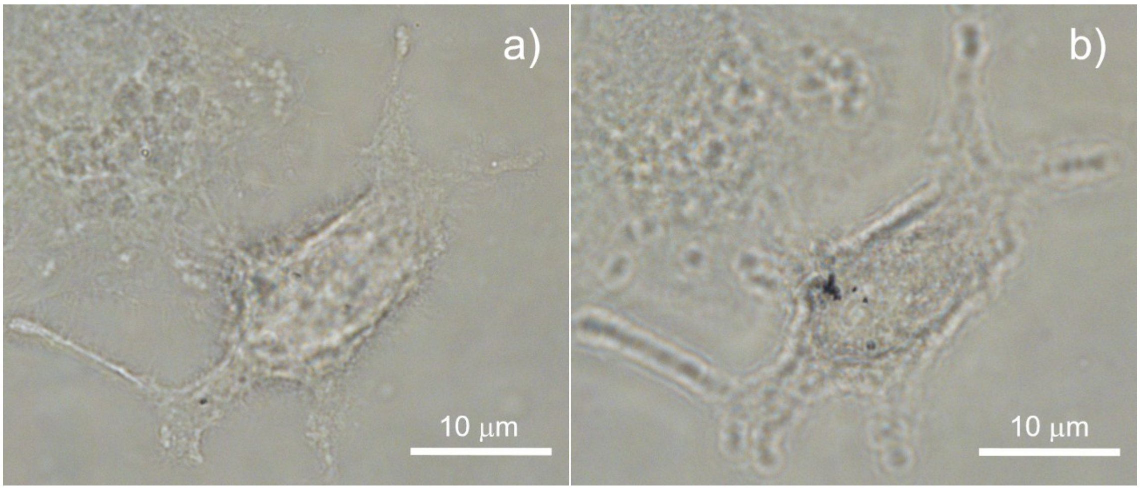

Figure 3.2. Optical micrographs of lung carcinoma cells after 24 h of incubation with nanodiscs ($R = 70$ nm and $T = 50$ nm, covered with gold). *a)* The surface of the cell is focused. *b)* An inner layer of the cell is focused appearing a group of nanodiscs.

Gold-covered microdiscs were added in a nominal proportion of 10 discs/cell, which was the same proportion used in [9]. In order to compare the internalization rates between the nanodiscs and the microdiscs, two options seemed to be the most reasonable: (A) addition of the nanodiscs in the same proportion or (B) addition of the nanodiscs equivalent in mass to 10 microdiscs/cell (that would be $\sim 1.6 \times 10^{-5}$μg/cell). The option A was not feasible since such a small amount of nanodiscs would impede the assessment using the microscope. Therefore, we chose the option B and added ~2000 nanodiscs per cell, $\sim 1.5 \times 10^{-5}$μg/cell. The results are shown in Figure 3.3, which indicates that the number of cells that have internalized nanodiscs is slightly higher, probably, due to the better distribution of the nano-sized discs in the medium. Furthermore, it must be taken into account the difficulty of finding the nanodiscs using the optical microscope; most likely, lots of them were missed, so the internalization rate may be even larger.

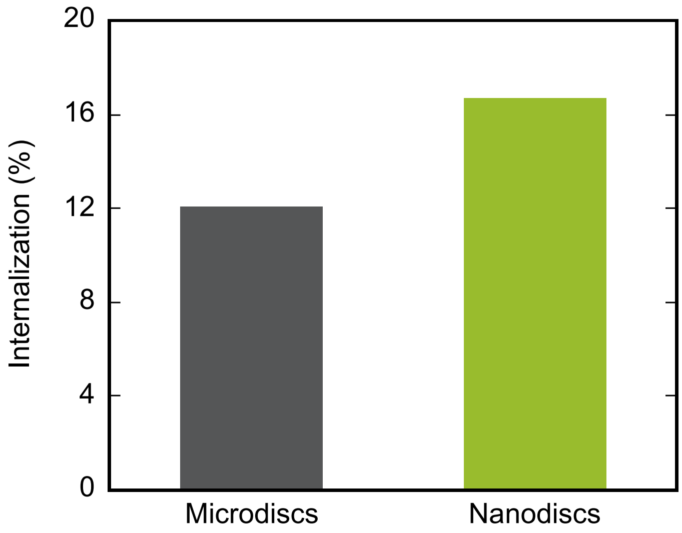

Figure 3.3. Percentages of cells that have internalized microdiscs (R = 1 µm and T = 60 nm, covered with gold) and nanodiscs (R = 70 nm and T = 50 nm, covered with gold) after 24 h of incubation.

Another interesting parameter to study the influence of the size on the internalization process is the number of particles taken up by each cell. As can be seen in Figure 3.4*a*, the microdiscs can be counted quite accurately whereas the number of nanodiscs is an approximate value that can be calculated by taking account of the image scale and the measured diameter of the nanodiscs (~140 nm). In this way, we estimate that the cell at the top of the Figure 3.4*b*, has internalized ~50 nanodiscs (zoomed in the inset). The cells with no discs are neglected from the calculations. Thus, in average, each cell internalizes ~6 micrometre-sized discs (nominally 10) or 100 nano-sized discs (nominally 2000). If the amount of discs is translated into micrograms of Permalloy, the difference increases significantly being 10^{-5}µg/cell (equivalent to 6 microdiscs) against 7.3×10^{-7}µg/cell (equivalent to 100 nanodiscs). This result is promising since the Permalloy ($Ni_{80}Fe_{20}$) mass and, thus, the nickel mass was reduced by almost two orders of magnitude whereas the number of magneto-mechanical actuators, *i.e.*, disc-shaped particles with magnetic vortex state, has been increased more than ten times.

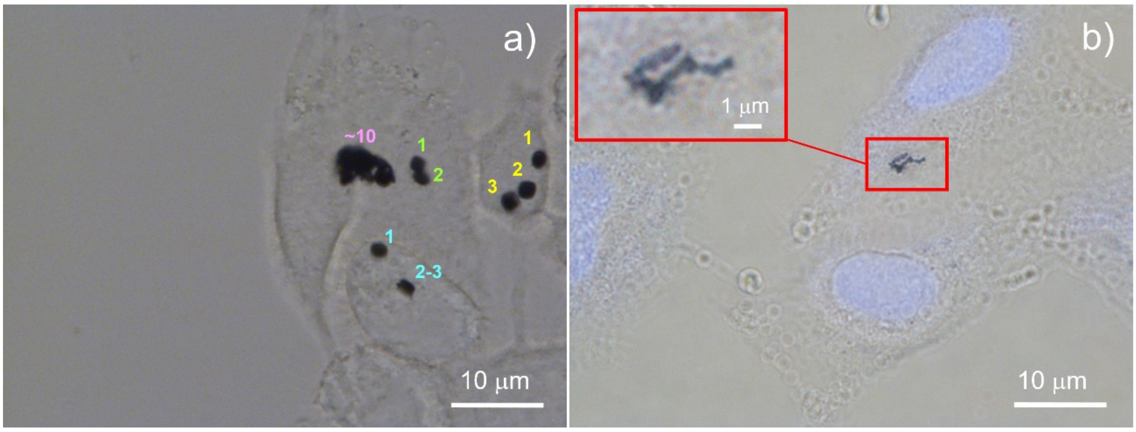

Figure 3.4. Micrographs of lung carcinoma cells after 24 h of incubation with (*a*) microdiscs (R = 1 μm and T = 60 nm, covered with gold) and (*b*) nanodiscs (R = 70 nm and T = 50 nm, covered with gold). The discs were added in nominal proportions of 10 and 2000 particles per cell, respectively.

Regarding the internalization mechanism, the process starts at the interaction between the particles and the cytoplasmic membrane, possibly through membrane proteins. Proteins contain a wide range of functional groups, including alcohols, thiols, carboxylic acids, carboxamides and a variety of basic groups able to react with the gold surface of the discs. Our hypothesis is that the cells internalize the particles by endocytosis and are subsequently accumulated into lysosomes, which are specialized organelles that contain hydrolytic enzymes. Lysosomes function as the digestive system of cells by processing compounds that enter the cell from the outside, as well as compounds inside the cell.

Transmission electron microscopy (TEM) was performed to provide insight to the intracellular localization of the discs. After 24 h of incubation with the particles, the cells were embedded in an epoxy resin and the solidified sample was cut in 70-90 nm thick slices (the protocol of the sample preparation is described in Appendix A). As shown in Figure 3.5, microdiscs are localized inside the cell and oriented perpendicular to the axis, suggesting that they may have been exposed to a low magnetic field during the fixation process (the same phenomena was observed in Ref. [12]). Clearly, the area surrounding the microdiscs contrasts with the texture of the cytoplasm, indicating they could be encapsulated in a lysosome (the holes are due to the dragging of the microdiscs during the cutting process).

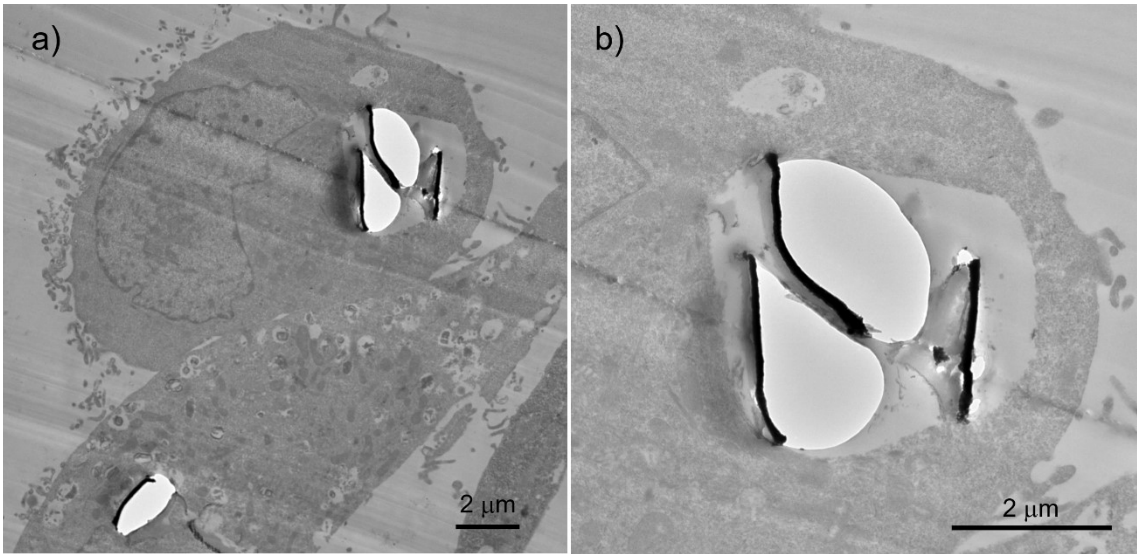

Figure 3.5. *a*) TEM image of lung cancer cells with microdiscs ($R = 1$ μm and $T = 60$ nm) inside. *b*) Three microdiscs, oriented perpendicular to the axis, are apparently encapsulated within a lysosome.

In the case of the nanodiscs, unfortunately, most of the cells did not survive the incubation, probably due to some residual contaminants from the nanodiscs fabrication/release process. Therefore, TEM images did not clarify the intracellular localization of the nanoparticles. However, some nanodiscs were localized within lysosome-like bags as pointed by the red arrow in Figure 3.6*a*. In Figure 3.6*b* instead, a group of nanodiscs seem to be interacting with the cell surface.

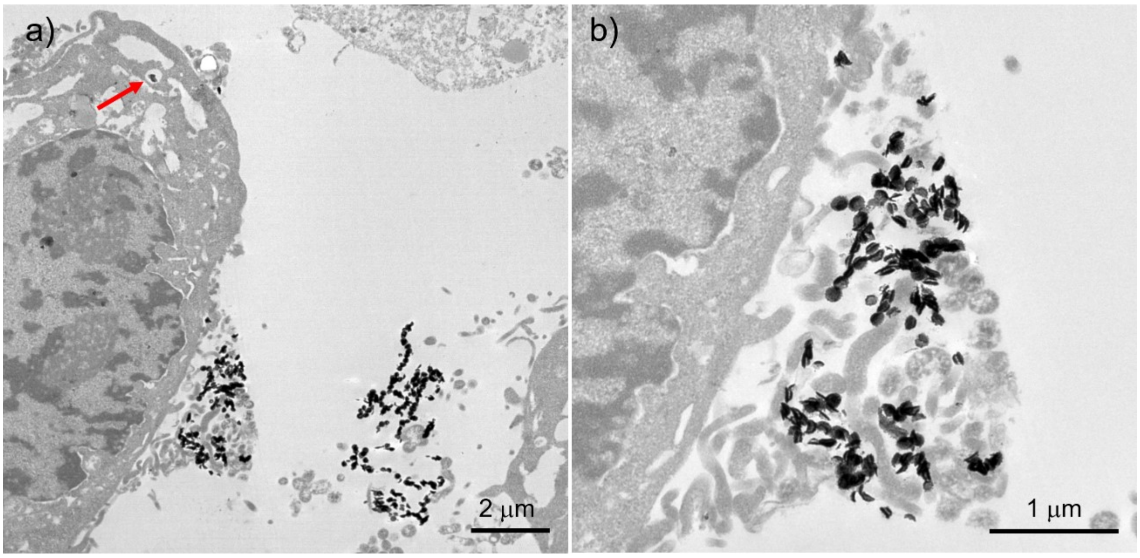

Figure 3.6. *a*) A small group of nanodiscs ($R = 70$ mm and $T = 50$ nm), pointed by the red arrow, is apparently within a lysosome of the lung cancer cell. *b*) A group of nanodiscs may be interacting with the cell surface.

For the further experiments, we used a larger concentration of microdiscs (nominally 25 microdiscs/cell) to increase the population of cells with particles to that observed using nanodiscs, *i.e.*, ~17 %.

3.3. Cytotoxicity

Prior to the study of the destructive capability of the discs under an external magnetic field, it is essential to evaluate their cytotoxic effect on the lung carcinoma cells. For that purpose, we followed the protocol described in section 3.1 and tested the impact of the microdiscs and the nanodiscs on the vital functions of the cells by adding, respectively, a nominal proportion of 25 and 2000 discs per cell.

Figure 3.7 collects two representative examples of the cytotoxicity tests. As described in the point 7 of the protocol, the NucBlue dyes the nuclei of all the cells blue (Figures 3.7*b* and 3.7*e*), which allows us to count the total population when using the DAPI standard filter. The PI instead, only penetrates in dead cells, thanks to the lower permeability of the dead cells membrane, and dyes the nuclei red, which can be observed when using the TRITC standard filter (Figures 3.7*c* and 3.7*f*). Representatively, none of the dead cells, marked with white arrows, have discs as point the red arrows in the brightfield images (Figures 3.7*a* and 3.7*b*). We followed this procedure in the rest of the assays.

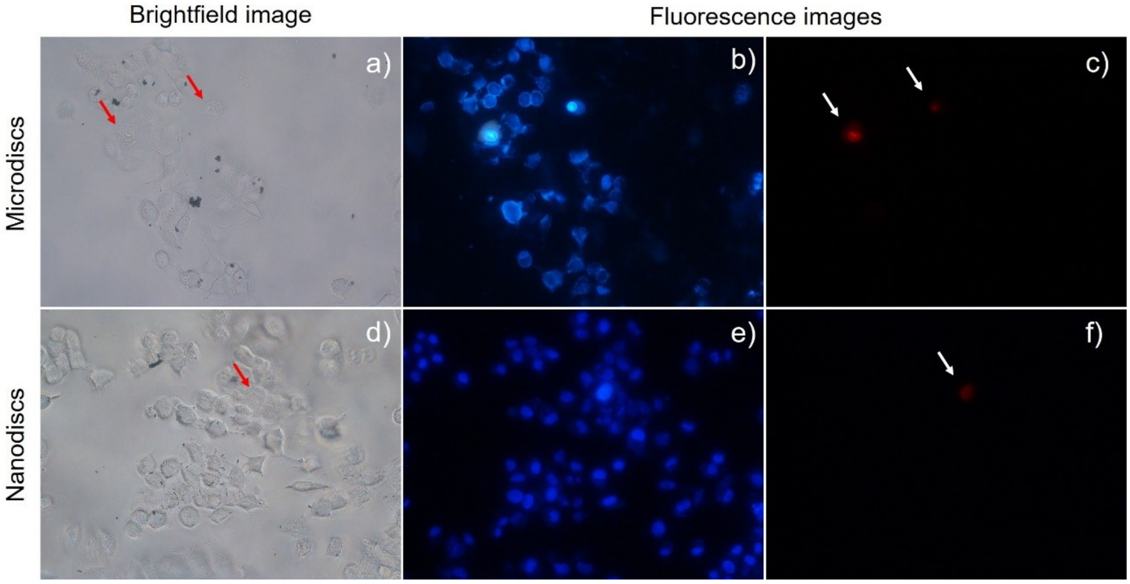

Figure 3.7. Micrographs of lung carcinoma cells after 24 h of incubation with microdiscs ($R = 1$ μm and $T = 60$ nm, covered with gold) and nanodiscs ($R = 70$ nm and $T = 50$ nm, covered with gold). (*a, d*) Microdiscs and the nanodiscs internalized by the cells. (*b, e*) The nuclei of all the cells. (*c, f*) Dead cells (marked with white arrows).

Figure 3.8 shows the results of cell viability after 24 h of incubation. Clearly, the viability is not affected by the introduction of Permalloy discs, being the live cells percentages of 99 % for the microdiscs covered with gold, 99.9 % for the microdiscs covered with titanium and 99.8 % for the nanodiscs covered with gold. This means that, in principle, the discs fabricated in the present Thesis are not cytotoxic by themselves. Probably, the gold and the titanium coatings play an important role on the positive result.

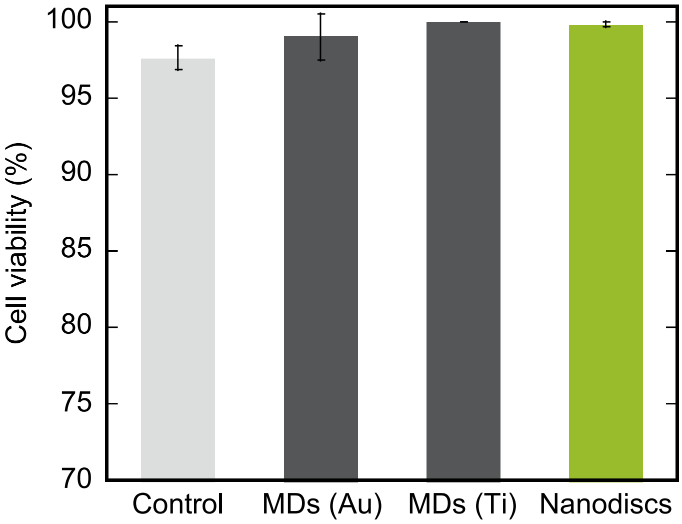

Figure 3.8. Percentage of viable cells after 24 h of incubation with microdiscs (R = 1 μm and T = 60 nm, covered with gold and titanium) and nanodiscs (R = 70 nm and T = 50 nm, covered with gold). Data represent the mean ± standard deviation, n = 3.
MDs: microdiscs, n: number of replicates.

However, there is another important indicator that should be evaluated when studying the cytotoxicity of a particle: the cell proliferation, *i.e.*, the increase in the number of cells as a result of cell growth and division.

The results of the cell proliferation after 24 h of incubation are presented in Figure 3.9. According to these results, despite the large deviation standard, the addition of the discs of both sizes may hinder the cellular reproduction since the control samples state with a population of ~600 cells/mm^2 whereas the samples with the discs count on ~500 cells/mm^2. As the A549 cell line approximately doubles its population in 24 h, we can consider that at t = 0 h, there were ~300 cells/mm^2, which, in the case of the control sample, after 24 h completed their cell cycle doubling the population, whereas in the case of the sample with discs, ~100 cells/mm^2 could not complete the cycle, reaching a population of ~500 cells/mm^2.

Interestingly, the percentage of the cells that could not undertake the cellular division (~20 %) is very close to the proportion of cells that had internalized particles. Therefore, although the internalization of the discs does not cause the death of the cells *per se*, the possibility that it inhibits the cell proliferation is rather plausible. Even though it may seem a non-desired effect, the capability of disrupting the cellular cycle could constitute an alternative or complementary therapeutic action if the discs specifically enter into cancer cells, which can be attained by functionalization.

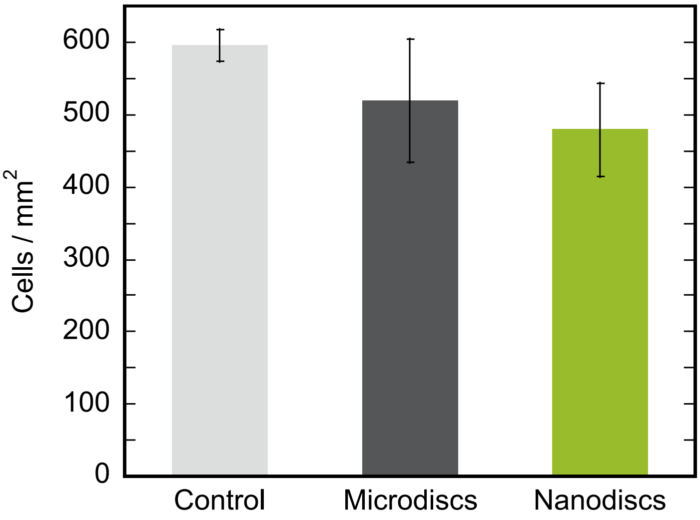

Figure 3.9. Influence of the addition of discs on the average number of lung carcinoma cells after 24 h of incubation. Data represent the mean ± standard deviation, $n = 3$.

Some examples of the disruption of the cell division were observed in the live cell videos, Figure 3.10 shows one of them. The cell marked with a red arrow is the result of the mitosis captured at $t = 2$ h. 19 h later, this cell internalizes a group of microdiscs (orange circle). The surrounding cells without discs, as the one marked with a blue arrow, divide whereas the cell with the microdiscs is not able to undertake the mitosis and, after 42 h of incubation, dies.

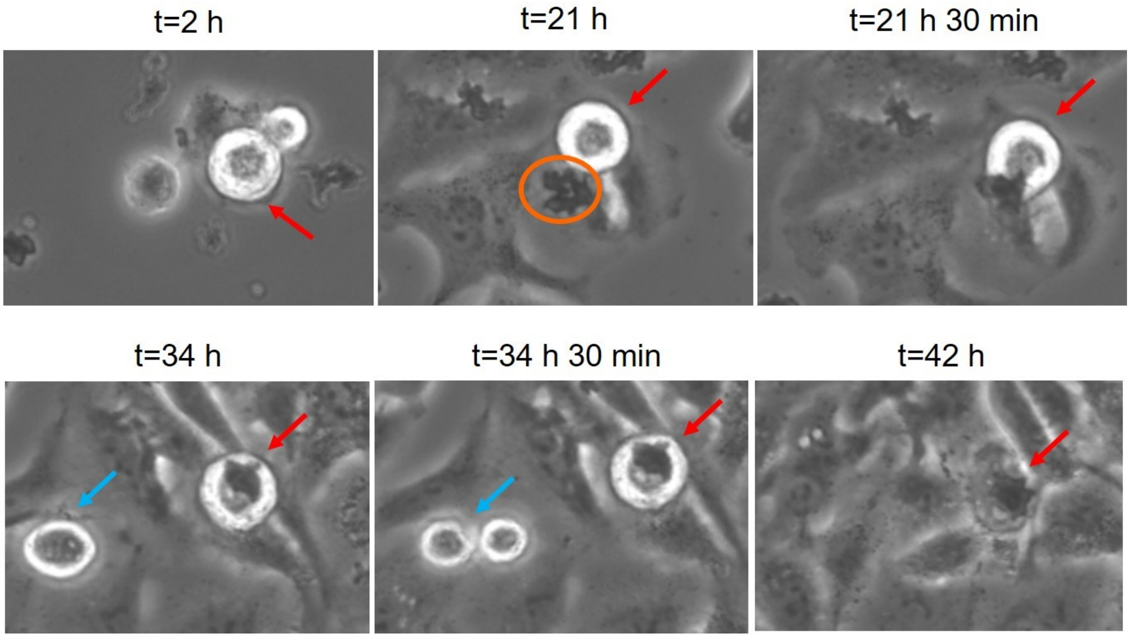

Figure 3.10. Live cell video captures at different times. At $t = 2$ h, the cell marked in red divides. At $t = 21$ h 30 min, it internalizes a group of microdiscs (orange circle). At $t = 34$ h 30 min, the cell marked in blue divides, whereas the cell with discs is not able to divide and dies after 42 h of incubation.

3.4. Magneto-mechanical stimulus

The last part of the Thesis addresses the study of the efficacy of the magneto-mechanically actuated nanodiscs to destroy cancer cells. The magnetic field station was built based on that reported by D-H Kim *et al*. [9] and is shown in Figure 3.11*a*. The AC magnetic field is generated by pair of Helmholtz coils and the well-plate with the cells is placed at the centre of the station. The magnetic field amplitude was set to 10 mT with a frequency of 10 Hz; it was reported to be sufficient to dramatically damage glioma cancer cell using Permalloy discs with $R = 0.5$ μm in [9].

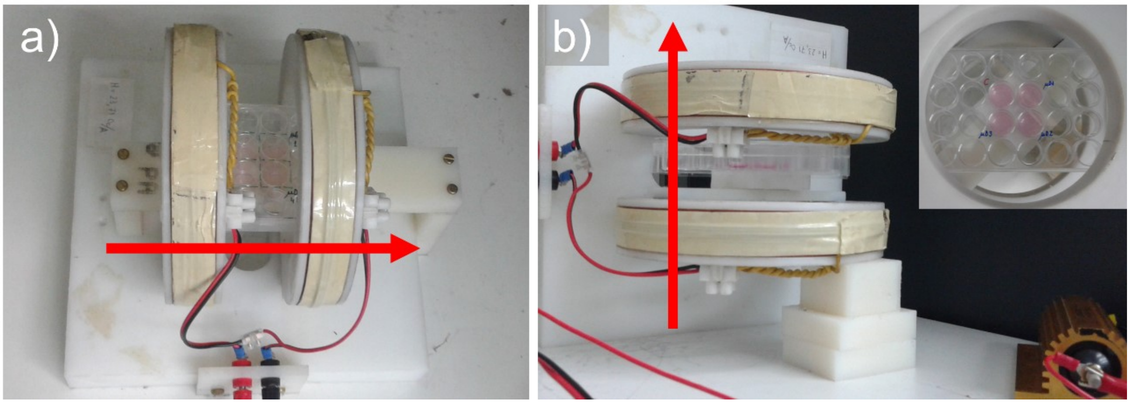

Figure 3.11. Magnetic field station. Helmholtz coils generate an AC field of 10 mT and 10 Hz (*a*) parallel or (*b*) perpendicular to the plane of the coverslips as the red arrows indicate. The well-plate is placed in the centre of the air gap as shown in the inset of the figure *b*.

The microdiscs used in these assays were covered with titanium. In the first assay, the magnetic field was applied parallel to the plane of the coverslips for 10 min and the viability was evaluated 1 h, 2 h and 4 h later to observe the evolution of the cells after the treatment. The control cells were examined after 4 h. The most significant results are those obtained with the cells that have internalized disc-shape-particles, therefore, the results presented hereinafter display the viability rates of the cells with discs. As shown in Figure 3.12, 1 h after the magnetic field application, the cells seem to be unharmed with almost 100 % of viability. One hour later, a reduction of 10 % in the viable cells was observed. Two hours further on, the rate of dead cells was kept almost constant being 13 %. Figure 3.13 shows representative micrographs of the first assay. Despite the outcome of the experiment is far from the expected one, it served to demonstrate that 1 h of incubation is not sufficient for the cells to experience any change in response to the applied stimulus. Hence, the post-treatment incubation time was set to 4 h for the following experiments.

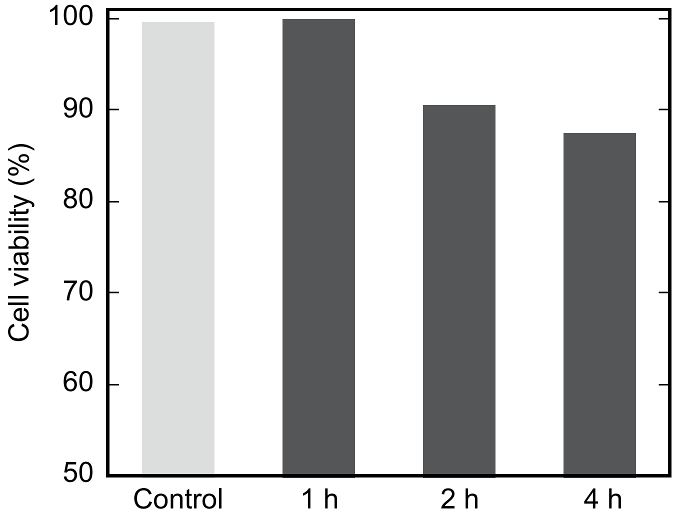

Figure 3.12. Percentage of viable cells (all of them hold microdiscs of $R = 1$ μm and $T = 60$ nm, covered with titanium) 1 h, 2 h and 4 h after the application of the magnetic field of 10 mT and 10 Hz for 10 min, being the field direction parallel to the coverslip plane.

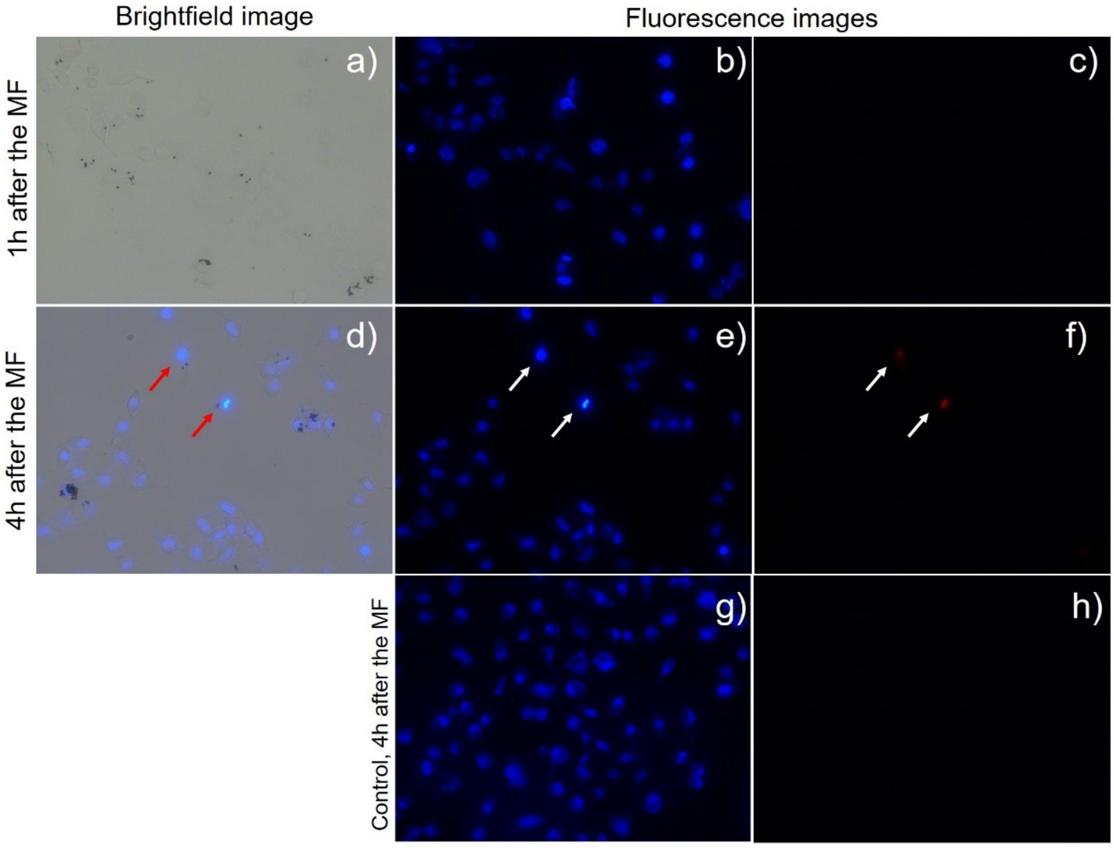

Figure 3.13. Cancer cells with microdiscs (R =1 μm and T = 60 nm, covered with titanium), (first and second row) and without (third row). 1 h after the magnetic stimulus, none of the cells were destroyed (*c*), whereas 3 h later, 2 of the 7 cells holding microdiscs (red arrows in *d*) are dead (white arrows in *f*). The magnetic field does not affect the cells without microdiscs (*g, h*).

In the second assay, the magnetic field was applied, again parallel to the plane of the coverslips, for 30 min. The percentage of dead cells 4 h after the magnetic stimulus resulted to be ~15 %. Therefore, the duration of the field application appear not to play a key role in the treatment, which led us to overhaul other parameters of the experiment, such as the direction of the magnetic field. To determine the ideal configuration, two points must be taken into account. On the one hand, the cell-culture we are studying is two-dimensional because the cells grow adhered to the coverslip forming a monolayer. On the other hand, the most favourable orientation for the microdiscs in a fluid is the horizontal one; most microdiscs internalized by cells are placed having the plane parallel to coverslip. This means that, using the configuration shown in Figure 3.11*a*, before the application of the magnetic field, a great part of the microdiscs are already aligned to it (being the angle α, described in the previous chapter, close to zero), thus, the torque of the microdiscs may be too small to produce any change in the cell integrity.

For this reason, the magnetic field station was modified in such a way that the field direction was perpendicular to the plane of the coverslips, as shown in Figure 3.11*b*. Furthermore, the perpendicular configuration increases the magnetic flux density affecting a cell since, as the A549 cells grow in the XY plane, more magnetic field lines will cross the cell. Both configurations are schematized in Figure 3.14.

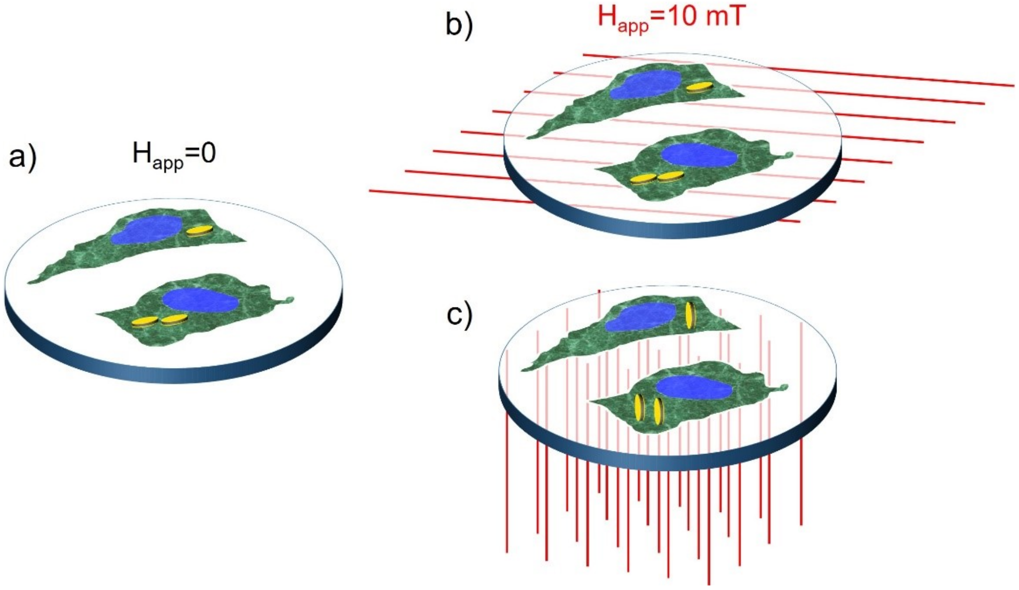

Figure 3.14. *a*) Cells adhered to the coverslip where most of the microdiscs are horizontally oriented. *b*) In the parallel configuration (Figure 3.11*a*), when the field is ON, the discs are already aligned to the field. *c*) In the perpendicular set-up (Figure 3.11*b*) the angle between the disc plane and the field direction is larger, enhancing the torque of the particle and the magnetic flux density affecting the cell is also higher (magnetic field lines in red).

Then, in the third assay, the magnetic field was applied perpendicular to the coverslips plane for 30 min. However, the dead cells rate did not increase from 15 % (the destruction of some cells is shown in Figure 3.15) indicating that the direction of the magnetic field is neither the key parameter. The other experimental conditions we could vary were the amplitude and the frequency of the magnetic field. As it was demonstrated in Chapter 2, a field as small as 2 mT and 1 Hz was proved sufficient to cause the mechanical torque of the microdisc in water. However, the movement of the particles in the cytoplasm is probably restricted and a higher magnetic field may be required. The field applied in the assays is five times larger (10 mT and 10 Hz) than that used in the light-transmission experiment, which may be sufficient to cause the rotation of the discs, but once the they are aligned with the field direction, the particles could get blocked due to the viscosity of the cytoplasm. Since our magnetic field set-up cannot produce greater magnetic fields, we did not find left room for improvement using the microdiscs and proceeded to test, for the very first time, the destructive capability of vortex state nanodiscs.

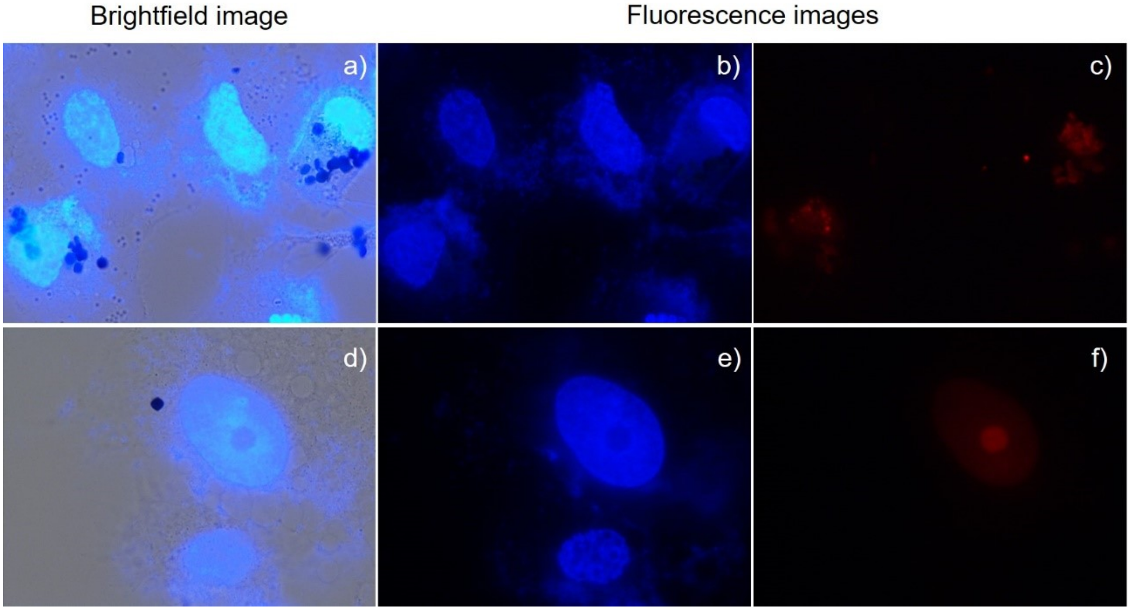

Figure 3.15. Cancer cells with microdiscs (R = 1 μm and T = 60 nm, covered with titanium), 4 h after the application of the magnetic field of 10 mT and 10 Hz for 30 min, in the perpendicular configuration.

The conditions were the same as those used in the last assay, *i.e.*, a magnetic field of 10 mT and 10 Hz perpendicular to the coverslips plane for 30 min. The nanodiscs (R = 70 nm and T = 50 nm covered with gold) were added in a nominal proportion of 2000 particles per cell. Four hours after the magnetic stimulus, the viability of the cells having nanodiscs was reduced by 30 %. Figure 3.16 compares the results obtained in the four assays, displaying the percentage of the cells viability after the treatment. Although the percentages may not be statistically sound, the results prove the ability of the nanodiscs to produce irreparable changes in cancer cell integrity. Figure 3.17 shows some micrographs of destroyed cells.

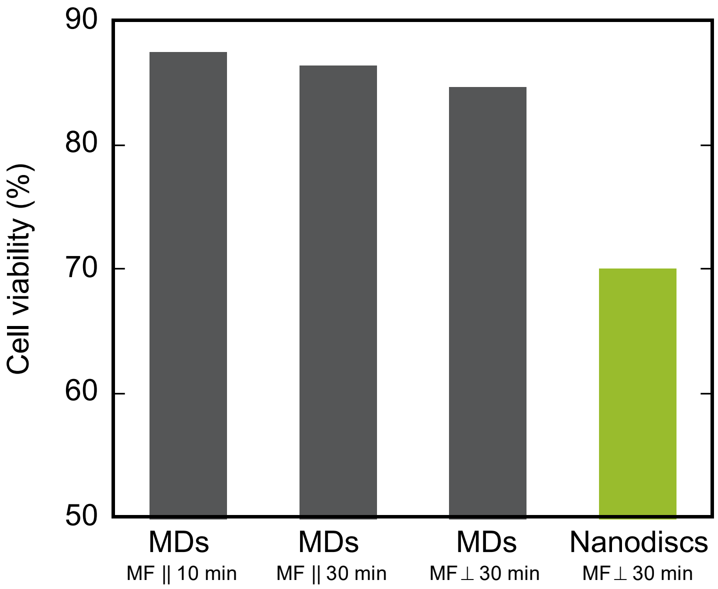

Figure 3.16. Percentages of lung carcinoma cell viability (all of them hold microdiscs or nanodiscs) 4h after the application of the magnetic field of 10 mT and 10 Hz.

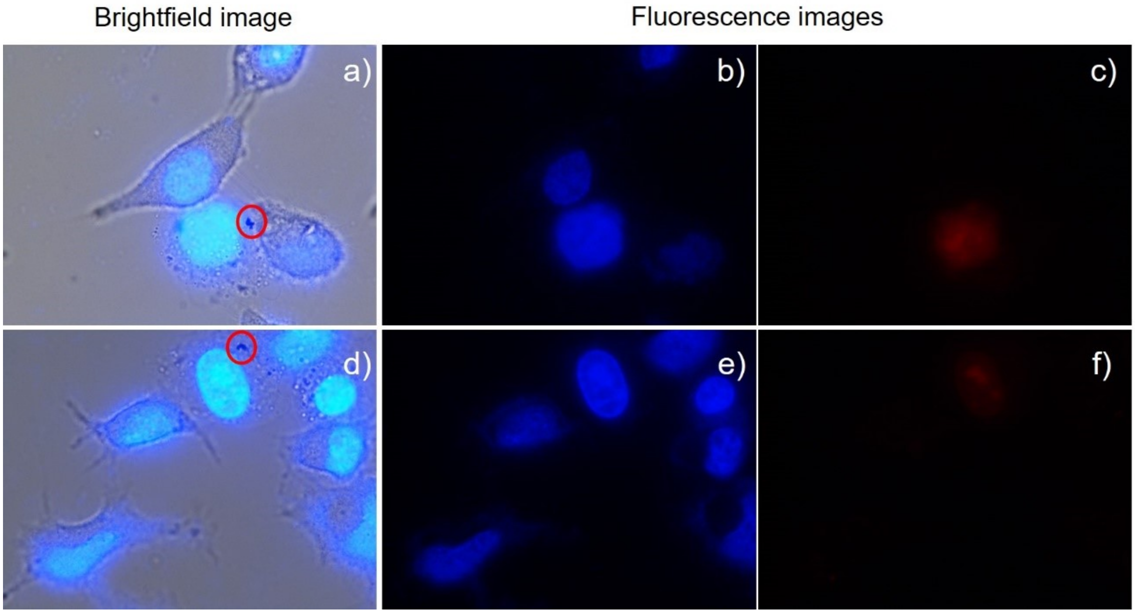

Figure 3.17. Micrographs of lung carcinoma cells with nanodiscs (R = 70 nm and T = 50 nm, covered with gold), 4 h after the application of the magnetic field of 10 mT and 10 Hz for 30 min, in the perpendicular configuration. In both examples, the cells that have nanodiscs (marked in red in *a* and *d*) have been destroyed (red nuclei in *c* and *f*).

To explain the effect of the treatment from the biological point of view, a cell death mechanism induced by the nanodiscs is proposed and summarized in Figure 3.18, where the lysosomal membrane rupture is suggested to be the principal cause. P. Saftig *et al*. have reported that lysosomal membrane permeabilization can induce the leakage of lysosomal hydrolases into the cytosol, and lead to cell death eventually [14, 15]. The membrane of the lysosome is a phospholipidic bilayer as it is the cellular membrane and the forces needed to break it are reported to be in the range of hundreds of piconewtons [16, 17]. In the previous chapter, we have estimated that each nanodisc can deliver a force of the order of piconewtons, which is too weak to rupture the membrane. However, the magnetic field leads to the formation of nanodiscs chains, as it was observed in the light-transmission experiment. Moreover, when removing the magnetic field, the nanodiscs rapidly break ranks and re-disperse in contrast with the microdiscs, which continue forming chains as it was deduced from the measurement of the relaxation times (see Figure 2.22 of the Chapter 2). Therefore, we hypothesize that once the nanodiscs are accumulated in the lysosomes, the chaining and re-dispersion of the nanodiscs created by the AC magnetic field could induce the lysosomal membrane rupture and trigger the cell death. Other magnetic nanoarchitectures have been proved to rupture the lysosomal membrane [18-20].

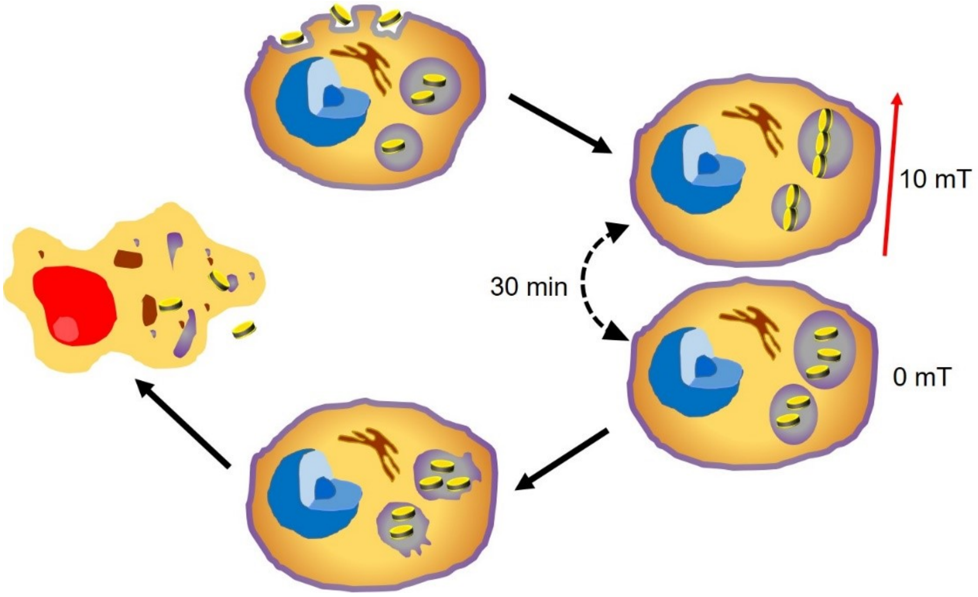

Figure 3.18. Scheme of the proposed mechanism of cancer cell destruction induced by vortex state nanodiscs. The lung carcinoma cells internalize the nanodiscs by endocytosis, which are accumulated in lysosomes. The AC magnetic field produces the chaining and re-dispersion of the particles. The associated forces break the lysosomal membranes, releasing the hydrolases to the cytosol and triggering the cell destruction.

3.5. Vortex nanodiscs in biomedicine

This final section intends to evaluate both the magneto-mechanical experiments with cancer cells performed in this Thesis (we propose new goals) and the potential of vortex nanodiscs for biomedical applications.

Figure 3.19 gives a schematic overview of the results, where the green circle represents the proportion of cells that have internalized nanodiscs (~17 %) and the red circle corresponds to the percentage of the dead cells (~30 % of the cells with nanodiscs and ~7 % of the total cells), being the ~75 % of them within the area of nanodiscs-holding cells.

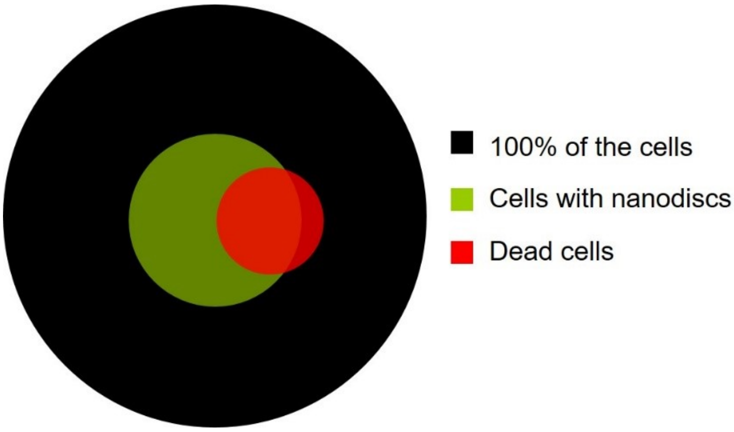

Figure 3.19. Visual description of the activity of the lung cancer cells during the *in vitro* assay. ~17 % of the total population have internalized nanodiscs after 24 h of incubation (green circle) and ~30 % of them have been destroyed 4 h after treatment. ~7 % of the total population were dead 4 h after treatment (red circle) and ~75 % of them have nanodiscs.

Moreover, after the magneto-mechanical treatment, several cells appeared to be damaged but still alive, so the propidium iodide (PI) could not cross the cell membrane and dye the nuclei red. The same phenomena was observed with the microdiscs. Indeed, the integrity of the cells holding discs is clearly disrupted as shown in Figure 3.20, suffering from cell shrinkage and membrane bubbling, characteristics of the cellular apoptosis. Therefore, the destructive effect of the nanodiscs could be larger than that indicated by the PI staining. Probably, the labelling of the apoptotic cascade hallmarks, such as caspase activation or DNA fragmentation, could have measured the destructive effectiveness of the nanodiscs with more accuracy [9, 11]. More specifically, the lysosomal membrane rupture can be detected through galectin-based strategy [21], which could prove the proposed cell death mechanism. Almost certainly, if the post-treatment time was extended to more than 4 h, the damaged cells would culminate the apoptotic process and the PI staining would be more efficient. However, the prolongation of the time is not convenient since the cell population would grow hindering the evaluation of the cell response to the magneto-mechanical actuation.

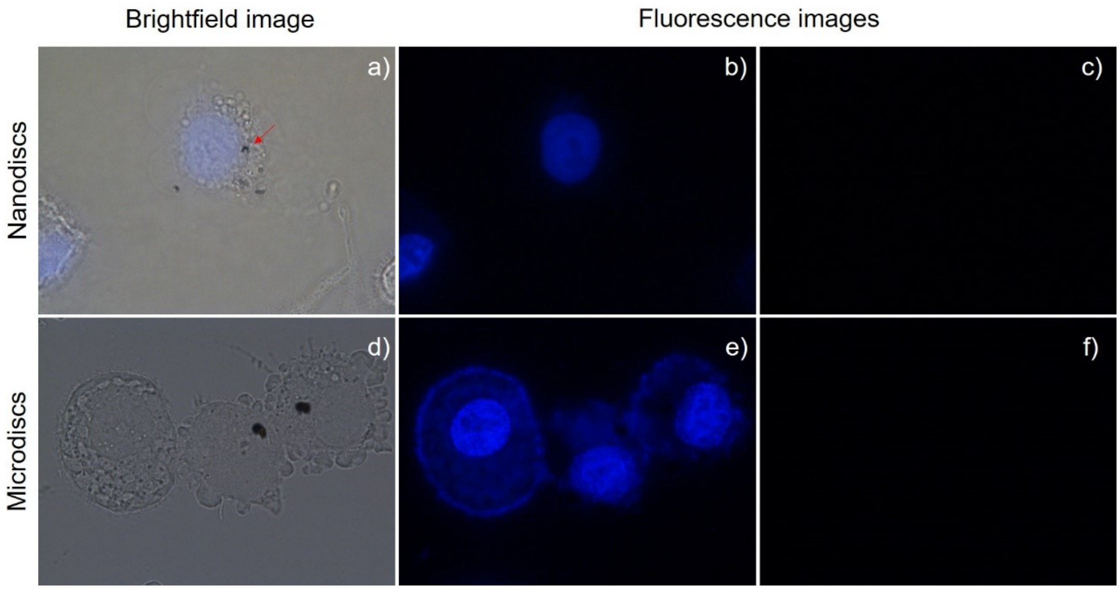

Figure 3.20. Micrographs of lung carcinoma cells holding nanodiscs (red arrow in *a*) or microdiscs 4 h after the application of the magnetic field of 10 mT and 10 Hz for 30 min in the perpendicular configuration. The cells with discs (*a* and *d*) suffer from membrane bubbling which is a characteristic of the apoptosis, indicating that they have been damaged. Nevertheless, they seem to be alive since the nuclei are not dyed red (*c* and *f*).

In any case, the efficacy of the treatment must be enhanced if the nanodiscs are intended to be used in further *in vitro* or *in vivo* assays. For that, two main issues ought to be addressed. On the one hand, the biofunctionalization of the nanoparticles is essential to improve the internalization by the cells and to specifically target lung carcinoma cells. On the other hand, the magnetic field configuration needs to be optimized to maximize the mechanical torque of the nanodiscs. Although the AC magnetic field used in our experiments produces a mechanical torque and the chaining of the discs (as demonstrated by the light-transmission experiment described in the Chapter 2), in the *in vitro* assays, once the plane of the particles is aligned to the field direction and the chain is formed, they could get stuck due to the large viscosity within the cell, and may not exert further torque. To overcome this problem, the group of Prof. Cowburn implemented a rotating magnetic field station consisting on a NdFeB Halbach array mounted on a motor to control its rotation [12]. When the plane of the disc is parallel to the plane of the magnetic field rotation, the magnetic moment of the disc can freely rotate in its own plane cancelling the mechanical torque. However, in the rest of the orientations, the magnetic moment of the particle is stuck and the disc rotates to get aligned to the field direction, ensuring a continuous torque. If considering the chaining of the nanodiscs, the rotating magnetic field would also produce a continuous rotation of the whole elongated nanoparticles agglomeration exerting a larger torque and, thus, a greater force as reported in [20]. Certainly, the biofunctionalization of the discs and the use of the rotating magnetic field in the *in vitro* experiments are our next steps in mind.

Beyond the purely mechanical action of the nanodiscs described and utilized in this Thesis, their magneto-mechanical actuation capacity can be exploited enabling alternative or complementary biomedical applications such as drug delivery or cancer cell proliferative inhibition. Actually, the mechanically activated local release of drugs using functionalized microdiscs has already been reported by D-H Kim *et al.* [22], where a low AC field induces the release of the drug (doxorubicin) encapsulated within the disc functional polymer coating (chitosan). Interestingly, during the cytotoxicity assays performed in this Thesis, a significant reduction of the cell population has been detected when using the nanodiscs. In fact, we observed that ~20 % of the cells could not undertake the mitosis, which is the same percentage of cells that had internalized nanodiscs. Therefore, as long as the nanodiscs specifically target cancer cells, they could mitigate or even stop the tumour growth.

References

[1] S. Dürr, C. Janko, S. Lyer, P. Tripal, M. Schwarz, J. Zaloga, R. Tietze and C. Alexiou, “Magnetic nanoparticles for cancer therapy”, *Nanotechnology Reviews*, vol. 2, pp. 395-409, 2013.

[2] R. K. Gilchrist, R. Medal, W. D. Shorey, R. C. Hanselman, J. C. Parrott and C. B. Taylor, “Selective inductive heating of lymph nodes”, *Annals of Surgery*, vol. 146, pp. 596–606, 1957.

[3] R. T. Gordon, J .R. Hines and D. Gordon, “Intracellular hyperthermia: a biophysical approach to cancer treatment via intracellular temperature and biophysical alterations”, *Medical Hypotheses*, vol. 5, pp. 83–102, 1979.

[4] N. F. Borrelli, A. A. Luderer and J. N. Panzarino, “Hysteresis heating for the treatment of tumours”, *Physics in Medicine and Biology*, vol. 29, pp. 487–94, 1984.

[5] S. Suzuki, K. Arai, T. Koike and K. Oguchi, “Studies on liposomal ferromagnetic particles and a technique of high frequency inductive heating—in vivo studies of rabbits”, *Journal of Japan Society for Cancer Therapy*, vol. 25, pp. 2649–58, 1990.

[6] A. Jordan, R. Scholz, P. Wust, H. Fahling and R. Felix, “Magnetic fluid hyperthermia (MFH): cancer treatment with AC magnetic field induced excitation of biocompatible superparamagnetic nanoparticles”, *Journal of Magnetism and Magnetic Materials*, vol. 201, pp. 413–19, 1999.

[7] E. A. Périgo, G. Hemery, O. Sandre, D. Ortega, E. Garaio, F. Plazaola, and F. J. Teran, “Fundamentals and advances in magnetic hyperthermia”, *Applied Physics Review*, vol. 2, pp. 041302, 2015.

[8] Q. A. Pankhurst, J. Connolly, S. K. Jones and J. Dobson, “Application of magnetic nanoparticles in biomedicine”, *Journal of Physics D: Applied Physics*, vol. 36, pp. R167–R181, 2003.

[9] D-H. Kim, E. A. Rozhkova, I. V. Ulasov, S. D. Bader, T. Rajh, M. S. Lesniak and V. Novosad, “Biofunctionalized magnetic-vortex microdiscs for targeted cancer-cell destruction”, *Nature Materials*, vol. 9, pp. 165–171, 2010.

[10] J. Vakkila and M. T. Lotze, “Inflammation and necrosis promote tumour growth”, *Nature Reviews Immunology*, vol. 4, pp. 641-648, 2004.

[11] S. Leulmi, H. Joisten, T. Dietsch, C. Iss, M. Morcrette, S. Auffret, P. Sabon and B. Dieny, "Self-polarization phenomenon and control of dispersion of synthetic antiferromagnetic nanoparticles for biological applications", *Applied Physics Letters*, vol. 97, pp. 253112, 2010.

[12] Y. Cheng, M. E. Muroski, D. C. M. C. Petit, R. Mansell, T. Vemulkar, R. A. Morshed, Y. Han, I. V. Balyasnikova, C. M. Horbinski, X. Huang, L. Zhang, R. P. Cowburn and M. S. Lesniak, "Rotating magnetic field induced oscillation of magnetic particles for in vivo mechanical destruction of malignant glioma", *Journal of Controlled Release*, vol. 223, pp. 75–84, 2016.

[13] T. Vemulkar, R. Mansell, D. C. M. C. Petit, R. P. Cowburn and M. S. Lesniak, "Highly tunable perpendicularly magnetized synthetic antiferromagnets for biotechnology applications", *Applied Physics Letters*, vol. 107, pp. 012403, 2015.

[14] P. Saftig and J. Klumperman, "Lysosome biogenesis and lysosomal membrane proteins: trafficking meets function", *Nature Reviews Molecular Cell Biology*, vol. 10, pp. 623-625, 2009.

[15] P. Boya and G. Kroemer, "Lysosomal membrane permeabilization in cell death", *Oncogene*, vol. 27, pp. 6434-6451, 2008.

[16] S. Sen, S. Subramanian and D. E. Discher, "Indentation and adhesive probing of a cell membrane with AFM: Theoretical model and experiments", *Biophysical Journal*, vol. 89, pp. 3203–3213, 2005.

[17] R. Afrin, T. Yamada and A. Ikai, "Analysis of force curves obtained on the live cell membrane using chemically modified AFM probes", *Ultramicroscopy*, vol. 100, pp. 187–195, 2004.

[18] A. M. Master, P. N. Williams, N. Pothayee, R. Zhang, H. M. Vishwasrao, Y. I. Golovin, J. S. Riffle, M. Sokolsky and A. V. Kabanov, "Remote actuation of magnetic nanoparticles for cancer cell selective treatment through cytoskeletal disruption", *Scientific Reports*, vol. 6, pp. 33560-33573, 2016.

[19] E. Zhang, M. F. Kircher, M. Koch, L. Eliasson, S. N. Goldberg and E. Renström, "Dynamic magnetic fields remote-control apoptosis via nanoparticle rotation", *ACS Nano*, vol. 8, pp. 3192-3201, 2014.

[20] S. Yajing, W. Congyu, T. Q. P. Uyeda, G. R. Plaza, B. Liu, Y. Han, M. S. Lesniak and Y. Cheng, “Elongated Nanoparticle Aggregates in Cancer Cells for Mechanical Destruction with Low Frequency Rotating Magnetic Field”, *Theranostics*, vol. 7, 2017.

[21] G. Kroemer and M. Jäättelä, “Lysosomes and autophagy in cell death control”, *Nature Reviews Cancer*, vol. 5, pp. 886-897, 2005.

[22] D-H. Kim, P. Karavayev, E. A. Rozhkova, J. Pearson, V. Yefremenko, S. D. Bader and V. Novosad, “Mechanoresponsive system based on sub-micron chitosan functionalized ferromagnetic disks”, *Journal of Materials Chemistry*, vol. 21, pp. 8422, 2011.

Conclusions

The key objectives of this Thesis, described in the Introduction, were satisfactorily fulfilled. They were oriented to develop a cost-effective fabrication of sub-100 nm Permalloy discs in the vortex state and to unravel the magnetic behaviour at such small dimensions, with the ultimate goal of using them as magneto-mechanical actuators to destroy cancer cells.

The main conclusions obtained are summarized below, organized along the three main areas of the research that constitute this work.

Concerning the search for nano-fabrication routes based on the use of self-assembled templates:

1. Alumina templates with tuneable porous size were prepared by the double anodization procedure. However, the technique could not be mastered to produce the desired nanostructures, raising important issues that eventually would require considerable efforts to be solved.
2. Nanosphere lithography (NSL) allowed us to prepare silicon oxide and Permalloy discs in sub-micrometric size. Nevertheless, important drawbacks were encountered such as: the difficulty of controlling all of the parameters related to obtaining large areas of PS spheres monolayers; the poor performance of Permalloy sculpting by ion milling; and finally the fact that the deposition of Permalloy over the silicon oxide pillars produces also a continuous film on the substrate, precluding the magnetic characterization of the discs since the removal of the pillars to detach the discs was also challenging.
3. Hole-mask colloidal lithography (HCL), which is an improved variant of NSL using surface charged polystyrene spheres, definitely met all the requirements to prepare Permalloy discs in nanometric size.

- The agglomeration of polystyrene spheres, which is the major problem of NSL, is eliminated thanks to the electrostatic forces between the negatively charged nanospheres and the positively charged surface, creating a non-ordered arrangement of PS spheres over the whole working area.
- Discs, 30 nm and 70 nm in radius, with well-defined morphology and small size distribution were fabricated. The thickness was accurately varied through the calibrated sputtering deposition time.
- The HCL method is a cost-effective nanofabrication technique with an estimated cost per wafer less than 5 euros and a production yield of up to 5×10^{10} nanostructures per wafer (~80 μg/wafer).
- A nanostructure-release-procedure was implemented based on a bottom germanium sacrificial layer that is eventually removed in hydrogen peroxide. Thus, we obtained both Permalloy nanodiscs on substrate, suitable for the morphological and magnetic characterization, and released nanodiscs for the assessment of the potential biomedical applications.

4. Permalloy microdiscs, 2 μm in diameter, were prepared by optical lithography. Titanium was selected as the biocompatible coating for the microdiscs since, its high adherence to the silicon oxide substrate, assures a successful lift-off in contrast with the gold coating.

With respect to the study of the magnetic behaviour of the nanodiscs prepared by HCL and the magneto-mechanical actuation capability of the nano and microdiscs, the main conclusions are:

1. We explored the limits of the vortex stability at the nanoscale by interpreting the particularities encountered in the measured hysteresis loops. For the Permalloy discs with R = 30 nm, being close to the convergence point of the three stable magnetic configurations (*i.e.*, in-plane single domain, out-of-plane single domain and vortex state), the thicknesses of 30 nm and 50 nm

approach the limits for presenting a well-defined vortex magnetisation reversal.

2. The discs with R = 30 nm and T = 50 nm present the characteristic shape produced by the vortex configuration and its magnetisation reversal process, what is significant since previous experimental evidence of the vortex behaviour in these range of dimensions have not produced such perfectly shaped loops.
3. The vortex core of the prepared nanodiscs is large compared to the total size of the disc, which has consequences in the magnetisation reversal mechanism. The most dramatic case corresponds to the nanodiscs with R = 30 nm and T = 50 nm, where the radius of the core can be even larger than the disc radius and which we have named *extra-large vortex*.
4. The analytical model developed in collaboration by K. Y. Guslienko to describe the large vortex state detected in our samples, is able to reasonably explain the measured vortex annihilation fields.
5. The nanodiscs and the microdiscs suspended in water respond rapidly to a magnetic field of 2 mT and 1 Hz aligning the plane of the discs parallel to the direction of the field and forming chains at the same time. When the magnetic field is removed, the nanodiscs re-disperse while the microdiscs keep forming chains, which is consistent with the self-polarization phenomena reported in the literature.
6. The forces that can be induced by nanodiscs with R = 70 nm are in the order of piconewtons, about 100 times smaller than the ones exerted by the microdiscs with R = 1 μm. These values were calculated from the in-plane magnetisation component of the disc induced by a field of 10 mT (*i.e.*, the field applied in the experiments with cells) with an angle of 45° between the applied field and the plane of the disc.

Concerning the study of the suitability of the Permalloy nanodiscs with R = 70 nm as magneto-mechanical actuators to destroy lung cancer cells:

1. The cancer cells internalize both the nanodiscs and the microdiscs covered with gold or titanium, even though they are not biofunctionalized. The discs were added in a nominal proportion of $\sim 1.5 \times 10^{-5}$μg/cell (*i.e.,* ∼2000 nanodiscs/cell and ∼10 microdiscs/cell) and incubated for 24 h.
    - The cell population with nanodiscs is up to 17 %, whereas the percentage of cells with microdiscs is about 12 %, probably due to the better distribution of the nano-sized particles.
    - Among the cells that hold particles, the average amount of particles per cell is ∼100 nanodiscs ($\sim 10^{-5}$μg) and ∼6 microdiscs ($\sim 10^{-7}$μg); the Permalloy ($Ni_{80}Fe_{20}$) mass and, thus, the potentially toxic nickel mass, has been reduced by almost two orders of magnitude whereas the number of magneto-mechanical actuators has been increased more than ten times.
2. The discs do not disrupt the viability of the cells, being the percentage of live cells almost 100 % for both diameters and coatings (gold and titanium), but they seem to inhibit the proliferation of the cells since the percentage of cells with discs is apparently the same as the percentage of cells that were not able to undertake the mitosis.
3. The application of the magnetic field of 10 mT and 10 Hz for 10 min leads to a low impact on the cell viability when using the microdiscs: only 4 h after the treatment, the cells started to exhibit some effect. Neither a longer treatment time (30 min), nor the application of the field perpendicular to the plane of the cell growth area, enhanced the efficiency of the assay. All the assays lead to a viability reduction of 15 % among the cells with discs.
4. In the case of nanodiscs, 4 h after the application of the magnetic field of 10 mT and 10 Hz for 30 min (with the field perpendicular to the cell growth area), the destroyed cell rate increased to 30 % among the cells with discs.
5. A hypothesis for the cancer cell death mechanism induced by the nanodiscs is proposed: the nanodiscs are internalized by the cell through endocytosis

and accumulated in the lysosomes. The chaining and re-dispersion of the nanodiscs created by the AC magnetic field could induce the lysosomal membrane rupture, releasing lysosomal hydrolases into the cytosol and triggering the cell death.

6. The use of a rotating magnetic field could definitely break the blocking and guarantee a continuum torque of the discs, enhancing the efficiency of the treatment. In our AC magnetic field station, when the field is switched on, the nanodiscs randomly oriented within the cell, suffer a mechanical torque that align their plane parallel to the field and, at the same time, makes them form chains also oriented with the field. However, when the field is removed, the particles may be stuck due to the large viscosity within the lysosome and, thus, could not relax like in water, hindering the exertion of further forces.

Appendix A

Experimental Methods

This appendix describes briefly the operating principles of the experimental techniques and equipment utilized in the Thesis. It does not intend to provide an exhaustive description of their working principle but only give the basic information necessary to supplement the fabrication routes and measurements presented along the Thesis.

Magnetron sputtering

Magnetron sputtering [1] consists in the bombardment of a target, made of the material that is to be deposited, with highly energetic inert gas ions, most usually Ar^+. A certain number of atoms from the target are expelled as a result of the energy transfer between the incoming Ar^+ ions and surface of the target. These extracted atoms travel through the deposition chamber and deposit onto the substrate placed opposite to the target, configuring, under the adequate process conditions, a thin film. The Ar^+ ions come from a plasma that is generated by the high voltage established between the anode and the target working as cathode. The deposition rate is greatly increased by intensifying the density of the plasma in the region close to the target. This is achieved in the so-called magnetron sputtering by the magnetic field generated by a set of magnets situated under the target. Figure A1 schematized the basics of a magnetron sputtering process.

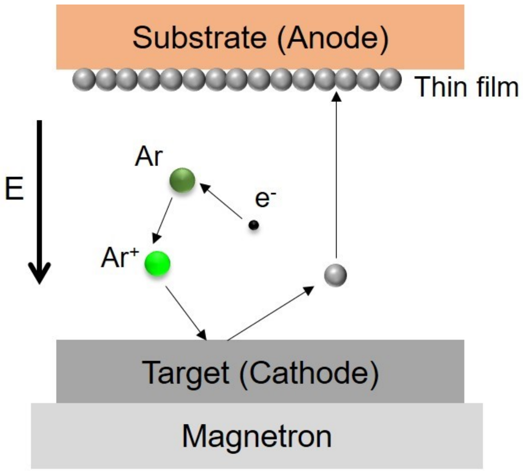

Figure A1. Schematic description of magnetron sputtering process.

The vacuum chamber used in this Thesis is a commercial Pfeifer Vacuum Classic 500 system equipped with magnetrons, whose process chamber is shown in Figure A2. The base pressure that can be reached in the chamber is 3×10^{-7} mbar using a turbo molecular vacuum pump. The sputtering facility has four separated magnetron cathodes (two of them special for magnetic targets) that can accommodate four different targets, allowing the deposition of different materials without opening the chamber. The height of the magnetrons can be modified to place them at a determined distance from the substrate, between 8 and 25 cm. The system is equipped with two DC and two RF (radio-frequency) power supplies to create the plasma, that can be connected to each magnetron, depending on the process to be done. The maximum attainable powers are 1000 W for the DC supplies and 300 W for the RF ones. The rotatory substrate holder allows positioning the desired substrate over the corresponding magnetron and depositing different materials in the same process without breaking the vacuum. In addition, a shutter can be operated between the target and the substrate to interrupt the deposition. A mass flow controller regulates the Ar gas flow in the chamber. The Ar pressure during the deposition process can be set between 2.4×10^{-2} and 8.4×10^{-3} mbar.

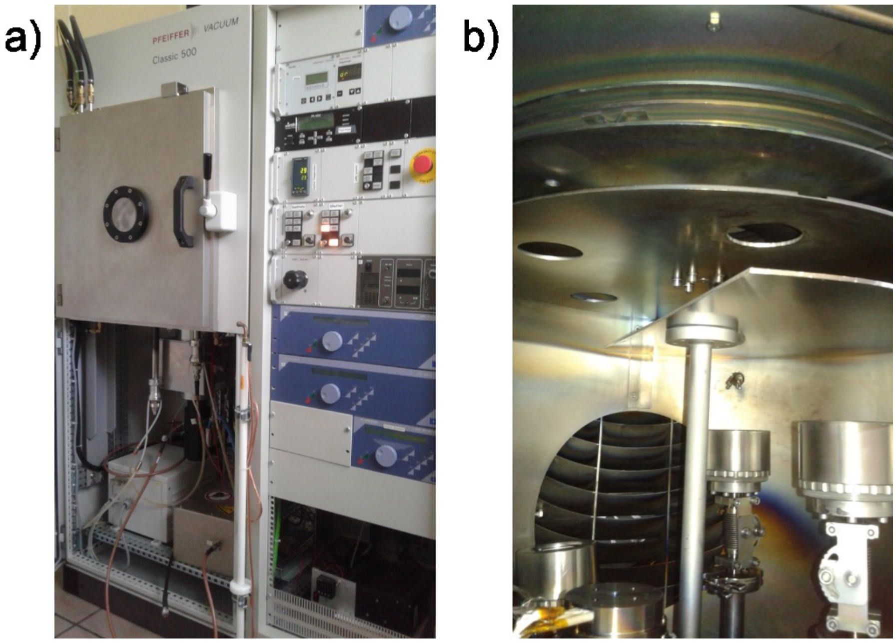

Figure A2. DC-magnetron sputtering system at the laboratory attached to the Clean Room of the University of the Basque Country (UPV/EHU). General view (*a*) and detail of the chamber (*b*).

Reactive ion etching (RIE)

Reactive ion etching [2] is today by far the most widely used dry etch process to transfer nanometric patterns. In this approach, the sample is etched by bombarding the surface with high-energy ions (several tens of eV to several keV) in a vacuum environment. A plasma radio frequency (13.56 MHz) is created inside a chamber, which has been previously filled with a gas mixture containing molecules that will generate radicals chosen to react with the sample surface. The latter is placed at the cathode of the system, which is generally coupled capacitively to the RF generator. This setup is designed so that it will spontaneously generate a negative potential at the sample surface when the plasma is initiated, due to the much higher mobility of free electrons in the plasma compared with the ions. This self-polarising potential accelerates positive ions in the plasma towards the sample and hence causes ion sputtering of the sample surface. The process is illustrated in Figure A3.

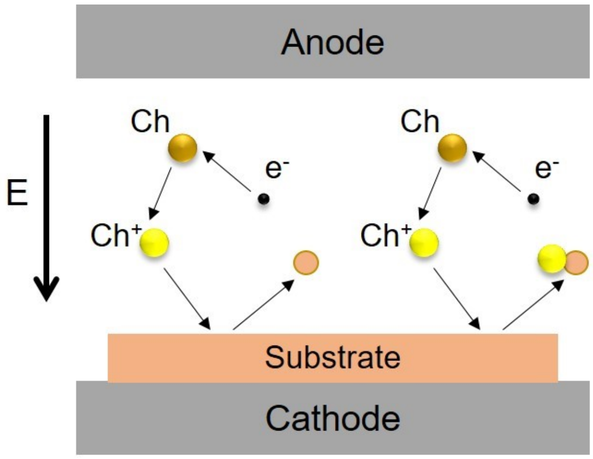

Figure A3. Schematic description of the reactive ion etching process where mechanical etching (on the left) or chemical etching (on the right) can be carried out.

The equipment used in this Thesis is a commercial Nano-Master NRE-4000 shown in Figure A4. This RIE system has a showerhead gas distribution and water cooled RF platen. The cabinet is made of stainless steel, whereas the chamber is a 13" cylinder made of aluminium that can open from the top for small substrate loading and has a load-lock for wafers up to 8". The chamber has two ports, one with a 2" window and the other with a blank off for diagnostic equipment such as end-point detection spectroscopy. The chamber reaches a base pressure in the 5 x 10^{-7} Torr range. It can be operated in the pressure range of 20 mTorr to 8 Torr. The pumping package has a 250 l/sec corrosive-proof turbomolecular pump, sieve filter and a 10 cfm PFPE (perfluoropolyether lubricant) prepared backing pump. The RF power is provided by 600 W 13.5 MHz power supply, and an auto-tuner. The substrate DC bias is continuously monitored and reaches a voltage as high as 500 V, which is important for creating an anisotropic etching profile.

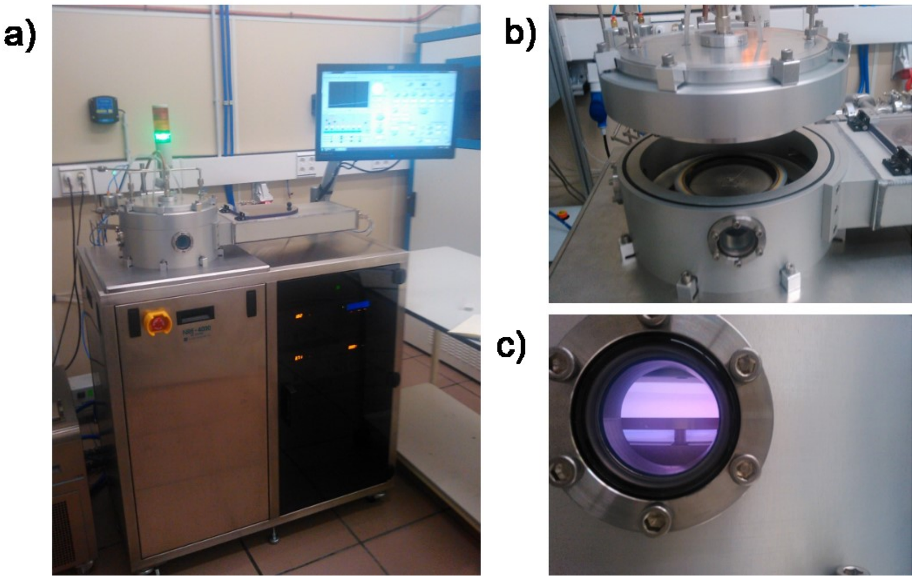

Figure A4. Reactive ion etching system located at the laboratory attached to the Clean Room of the University of the Basque Country (UPV/EHU). General view (*a*), main chamber (*b*) and oxygen plasma (*c*).

Thermal evaporation

Resistive thermal evaporation [3] is a popular physical vapour deposition technique because of its simplicity. Typically, metals are evaporated by passing a high current through a highly refractory metal. The refractory metal (for example W or Mo) is formed into a suitable container (*e.g.*, a boat or a filament) to hold the source material. Current is applied to heat the container, which then heats the material in contact with it. The process takes place in a high-vacuum environment and the vaporized molecules travel from the source to the substrate where they nucleate together, forming a thin-film coating as it is schematized in Figure A5.

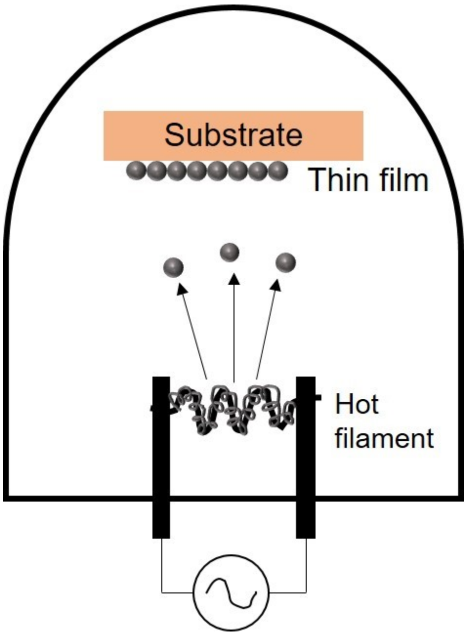

Figure A5. Schematic description of thermal evaporation process where a wire of metal is winded around the filament.

The equipment used in the present Thesis is a commercial Edwards Auto 306 shown in the Figure A6 that is located in the Clean Room of the Cavendish Laboratory (University of Cambridge, UK). The thermal evaporation was employed to fabricate the 2 μm discs. For that, gold pellets were placed in boats of tungsten whereas a wire of Permalloy was winded around the tungsten filament (Figure A6*b*).

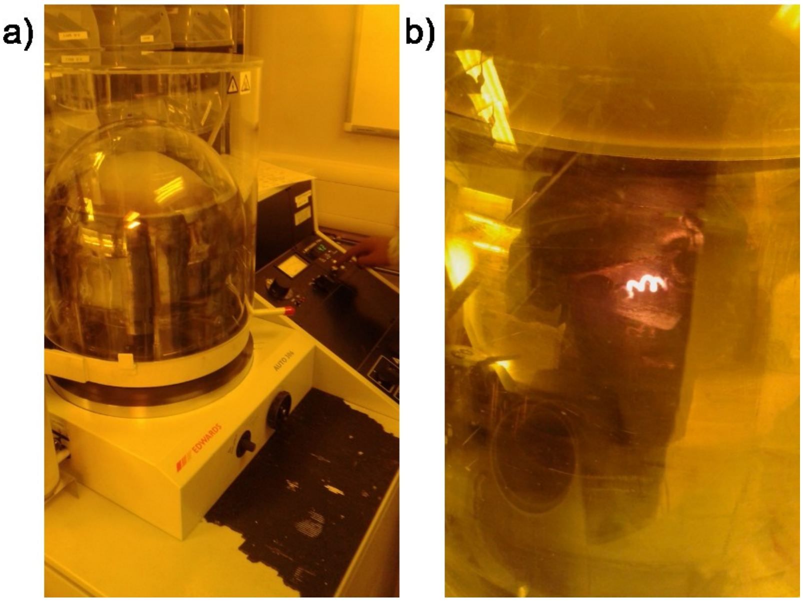

Figure A6. Thermal evaporation system located in the Clean Room of the Cavendish laboratory (University of Cambridge, UK). General view (*a*) and detail of Permalloy in evaporation (*b*).

Clean Room

The microdiscs were prepared by means of photolithography as explained in the section 1.2.1 (Chapter 1). The main apparatus needed are the spinner (to coat the photoresist over the wafer), the mask aligner (to accurately position the patterned mask on the wafer) and the UV-lamp (for the ultraviolet-light exposure that transfers the pattern to the photoresist).

The discs 10 μm in diameter were prepared in the Clean Room of the University of the Basque Country (UPV/EHU), shown in Figure A7. The spinner is from Laurell Technologies Corporation (model WS400E-6NPP-Lite). The mercury lamp, that exposes a 365 nm wavelength UV-light, was manufactured by Bachur and Associates (model LS100-2). The mask aligner was designed and manufactured by Suministro de Materiales y Asistencia S.L., according with our specifications.

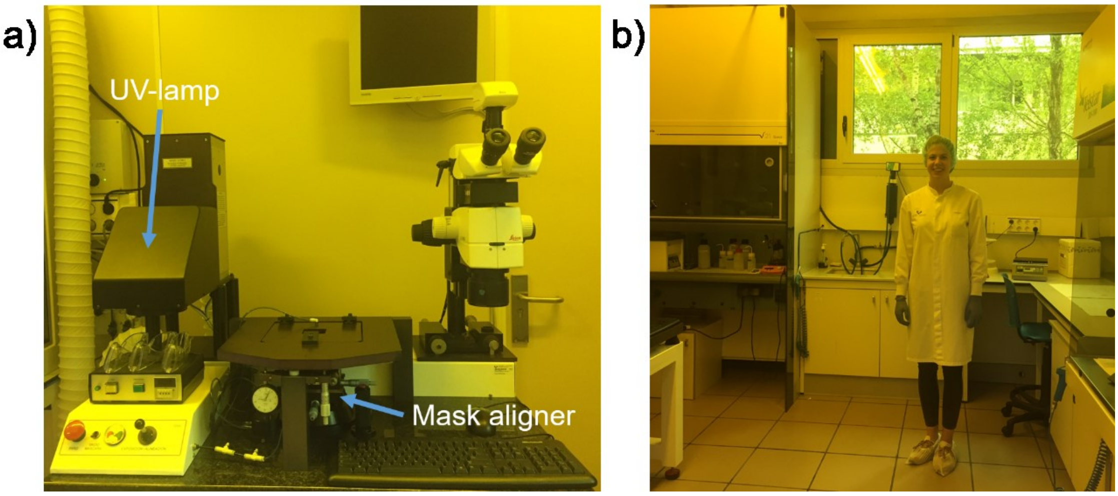

Figure A7. Clean Room located at the University of the Basque Country (UPV/EHU). *a*) UV-lamp and mask aligner. (*b*) Clean Room clothes.

The discs 2 μm in diameter were prepared in the Clean Room located at the Cavendish Laboratory (University of Cambridge, UK), shown in Figure A8. The spinner was the same used in UPV/EHU. The mask aligner (MJB4, from SUSS MicroTec) and the mercury lamp (365 nm UV-light), are located at the Nanoscience Centre (University of Cambridge, UK).

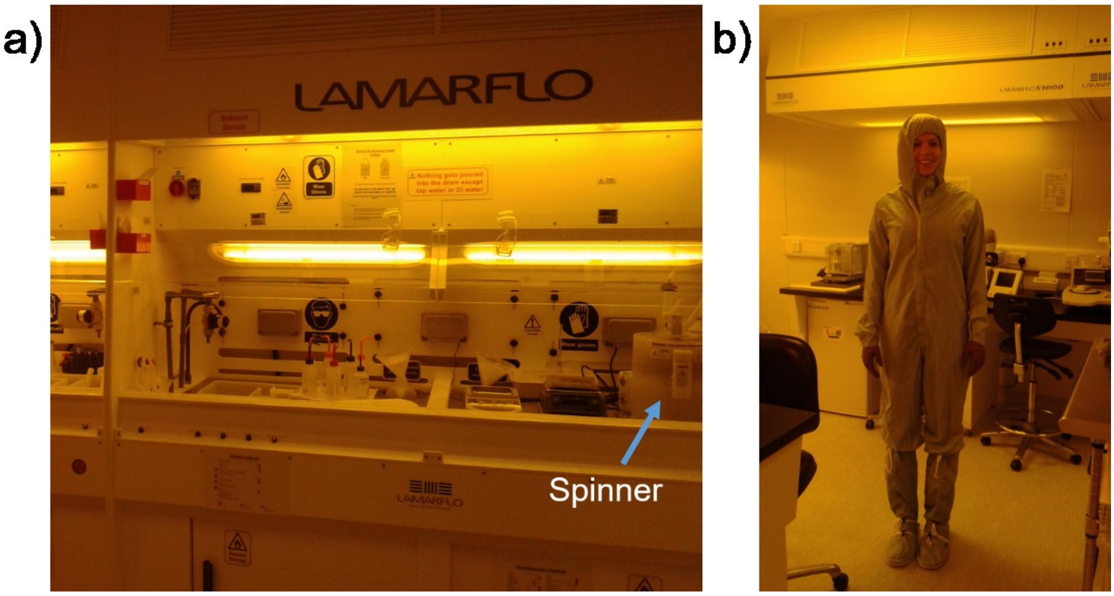

Figure A8. Clean Room located at the Cavendish Laboratory (University Cambridge, UK). *a*) Spin-coating area. (*b*) Clean Room clothes.

Scanning electron microscopy (SEM)

The scanning electron microscope [4] is one of the most versatile instruments available for the examination and analysis of the microstructure, morphology and chemical composition characterizations. The image formation in the SEM is dependent on the acquisition of signals produced from the electron beam and specimen interactions. These interactions, illustrated in Figure A9, can be divided into two major categories: elastic interactions and inelastic interactions. The most widely used signal produced by the interaction of the primary electron beam with the specimen is the secondary electron emission signal. When the primary beam strikes the sample surface causing the ionization of specimen atoms, loosely bound electrons may be emitted and these are referred to as secondary electrons. As they have low energy, typically an average of around 3–5 eV, they can only escape from a region within a few nanometres of the material surface. Therefore, secondary electrons accurately mark the position of the beam and give topographic information with good resolution.

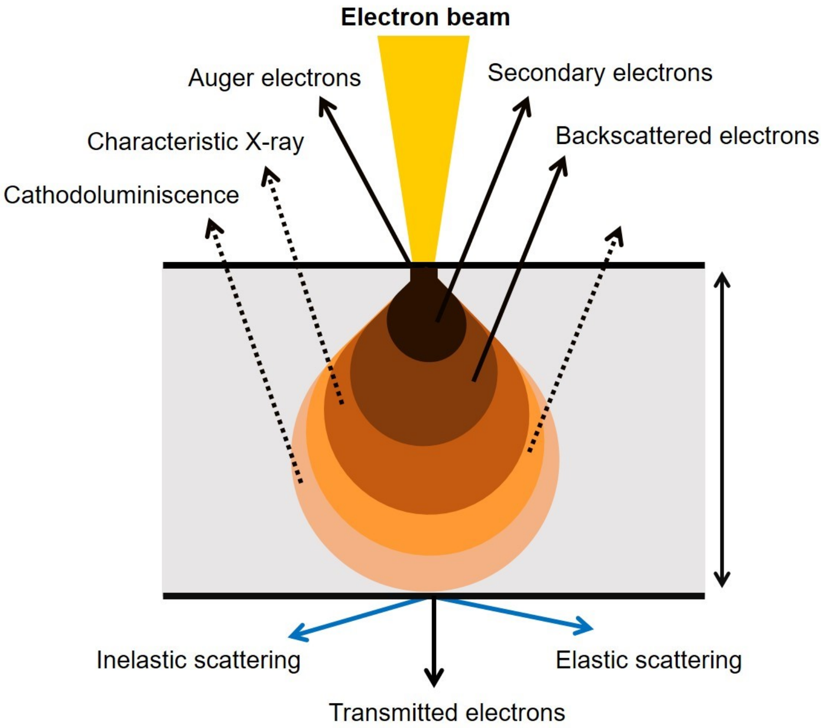

Figure A9. Illustration of the signals generated by the electron beam–specimen interaction in the scanning electron microscope and the regions from which the signals can be detected.

In this work, two SEM equipment were used depending on the required resolution: table-top Hitachi TM3000 with a resolution of 30 nm, located in the laboratory adjacent to the Clean Room (Figure A10*a*) and MEB-FEG JEOL 7000F with a resolution of 1 nm, located at the General Research Services (Figure A10*b*), both at the University of the Basque Country (UPV/EHU).

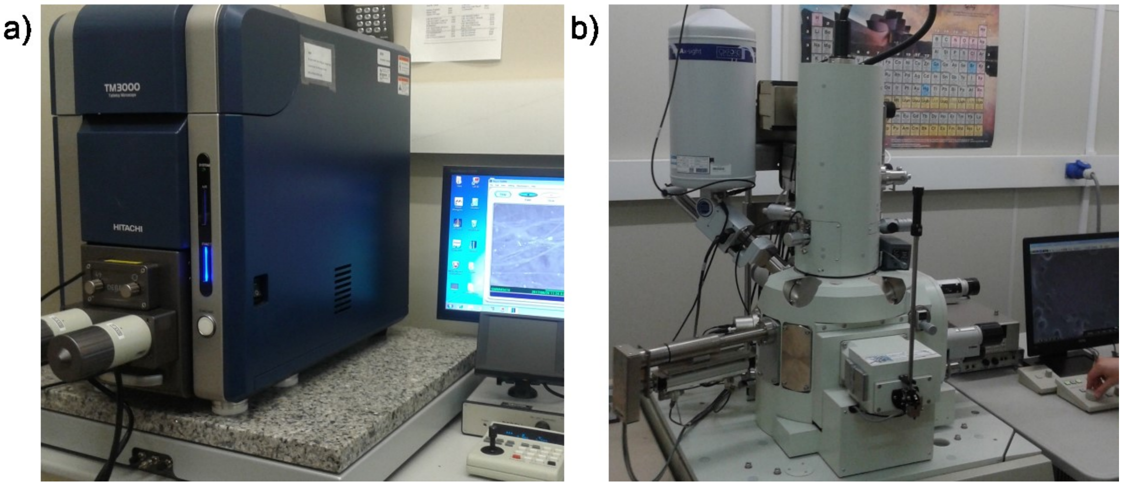

Figure A10. Scanning electron microscopes located (*a*) in the laboratory adjacent to the Clean Room and (*b*) in the general research services of the University of the Basque Country (UPV/EHU).

Transmission electron microscopy (TEM)

In a transmission electron microscope [5], the specimen is irradiated with an electron beam of uniform current density. In contrast to SEM, the image is formed by the transmitted electrons (Figure A10), that is why the specimen must be very thin, typically of the order of 5 nm to 0.5 μm for 100 keV electrons. The equipment used in this work is a JEOL 1400 Plus shown in Figure A11.

Figure A11. Transmission electron microscope located in the general research services of the University of the Basque Country (UPV/EHU).

The protocol followed to prepare the samples involves 11 steps:

1. Cell pre-fixation with glutaraldehyde 2 vol.% in PBS at 24 °C for 24 h.
2. Cell detachment, with the help of a scraper, and centrifugation (1200 rpm, 5 min), obtaining a pellet.
3. Fixation with glutaraldehyde 2 vol.% in cacodylate 0.1 M at room temperature.
4. Pellet washing with cacodylate and sucrose 4-8 vol.% (three times).
5. Post-fixation with OsO_4 1 vol.% in cacodylate, 1 h in darkness at 4 °C.
6. Pellet washing in cacodylate for 10 min (three times).
7. Dehydration in acetone in a series of growing concentration (30 %, 50 %, 70 %, 90 %, 96 % and twice in pure acetone), 15 min each.
8. Pellet washing in pure propylene oxide (PO) for 10 min (twice).
9. Embed the pellet in epoxy resin (ER) in a series of growing concentration: PO-ER 2:1 (60 min), PO-ER 1:1 (60 min), PO-ER 1:2 (60 min) and ER 100 % (overnight).

10. Transfer the pellet to the capsule, embed in new epoxy resin and polymerize at 55°C for 48 hours.
11. Ultramicrotomy: semi-fine cuts, staining with toluidine blue, selection of the desired zone by optical microscope, ultra-fine cuts, grids contrast with lead citrate and uranyl acetate.

Atomic and magnetic force microscopies (AFM/MFM)

The atomic force microscope [6] works by measuring the deflection of an elongated cantilever where a small conic probe is located at one of the edges of a flexible cantilever, whereas the other edge is put in contact with a piezoelectric material. A laser spot hits on the back part of the probe in the edge of the cantilever and its position is detected by a photodetector; the position of the reflection of the laser in the photodetector will change according to the lateral and vertical movements occurring in the cantilever, which are due to the forces generated on the probe by its interaction with the sample. The mechanism is schematized in Figure A12*a*.

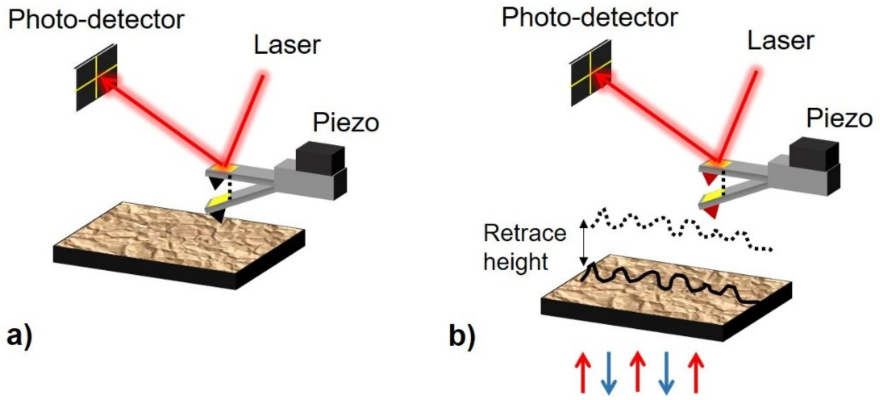

Figure A12. Schematic description of the atomic force microscopy measurement (*a*) and the two-step magnetic force microscopy measurement (*b*).

The AFM tool used in this Thesis is a commercial Nanotec Electrónica shown in the Figure A13. To measure the topography of the nanodiscs, we used the non-contact mode. With this dynamic AFM mode it is possible to reach atomic resolution in a consistent way, and is based on the fact that the distance between the surface and the probe is big enough so that the forces acting on the probe are only attractive. The feedback signal in this mode is the frequency shift on the cantilever oscillation produced by the probe-sample interaction required to maintain a constant oscillation amplitude during the whole measurement. The oscillation amplitudes usually employed in the non-contact dynamic AFM mode are in the range of 40 nm.

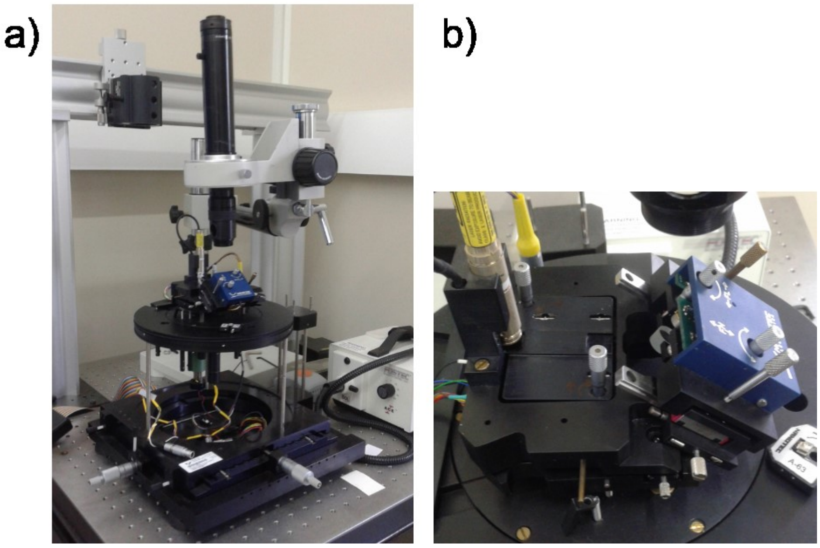

Figure A13. Atomic force microscope located at the Materials Laboratory of the University of the Basque Country (UPV/EHU). General view (*a*) and zoomed view (*b*).

The magnetic force microscopy [7] is a variant of the atomic force microscopy where the tip is covered by a layer of ferromagnetic material with specific magnetisation. In our case, as mentioned in the Chapter 2, homemade Co coated tips were used. In order to reconstruct the map of nanodiscs' magnetic structure, a two-pass technique was used in dynamic non-contact mode: on the first pass, the AFM topographic image is obtained, for the second pass, the tip is retracted 20 nm from the surface and the scanning is repeated. The value of the distance must be large enough to make the Van der Waals force smaller than the magnetic interaction force. The process is schematically described in Figure A12*b*. The magnetic force microscope used by Eider Berganza, in the group of Dr. Agustina Asenjo at ICMM, for the measurement of the vortex cores of the nanodiscs is also a commercial Nanotec Electrónica, shown in Figure A14, with a coil that generates the magnetic field (Figure A14*b*).

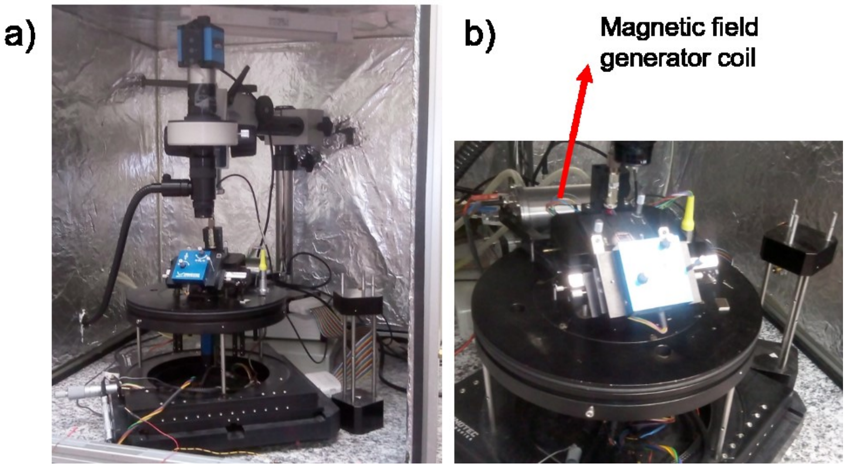

Figure A14. Magnetic force microscope located at the Instituto de Ciencia de Materiales, Madrid. General view (*a*) and zoomed view showing the coil (*b*).

Magneto-optic Kerr effect magnetometry (MOKE)

In a MOKE hysteresis loop tracer the magnetic signal from the sample is measured from the rotation of the polarization plane of the light reflected by the magnetized material. The experimental set-up (Figure A16), located in the Laboratory of Magnetism in the University of the Basque Country, is coincident with the one described in [8]. It uses the longitudinal mode MOKE (meaning that the direction of the magnetisation is parallel to the reflecting surface and is contained in the plane of incidence) and *s*-polarized incident light (the electric field perpendicular to the plane of incidence). Due to the magnetisation of the sample, the polarization plane of the reflected light acquires a small *p*-polarized component (with the electric field contained in the plane of incidence). The reflected light is filtered by a second polarizer, nearly crossed with respect to the first one. In this way, the amplitude of the transmitted light is directly proportional to the component of the surface magnetisation parallel to the plane of incidence. Figure A15 schematizes this MOKE configuration.

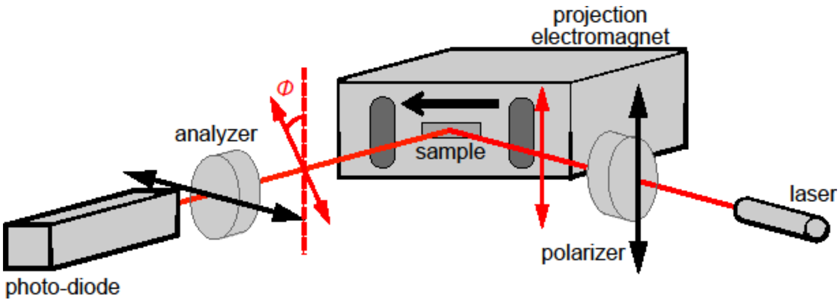

Figure A15. Scheme of magneto-optic Kerr effect magnetometry measurement.

As light source, a laser diode with a wavelength of 670 nm (red light) and a power of about 3 mW is used. The laser produces a rectangular spot size of about 330 μm in diagonal. A set of lenses is introduced to focus the spot and reduce its size down to 20 μm. The sample is magnetized by the magnetic field created by a projected-field electromagnet, capable of creating fields up to 2 kOe in the plane of the sample. The electromagnet is fed by a bipolar Kepco power supply and water-refrigerated. The actual field applied to the sample is measured by a Hall probe. The detecting photo-diode is placed in an anti-reflections tube that includes a convergence lens to focus the light in the centre of the sensor.

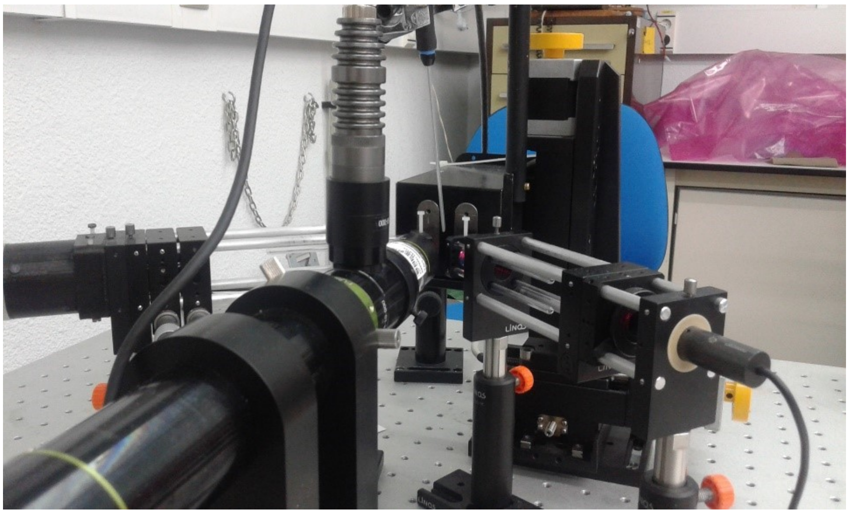

Figure A16. Magneto-optic Kerr effect magnetometer located at the Laboratory of Magnetism at the University of the Basque Country (UPV/EHU).

Superconducting quantum interference device (SQUID)

The superconducting quantum interference device [9] is the most sensitive magnetic flux detector. This device, operating at cryogenic temperatures with quantum-limited sensitivity, has demonstrated field resolution at the 10^{-17} T level. The SQUID sensor, which is based on the quantum tunnelling through Josephson junctions, is less than 2 mm in diameter. During the measurement, the sample is shifted through a set of secondary superconducting coils inductively coupled to the SQUID sensor by means of an intermediate circuit. The configuration is schematized in Figure A17. The relation between the measured signal and the actual magnetic moment of the sample is determined by calibrating a sample with a well-known magnetic moment.

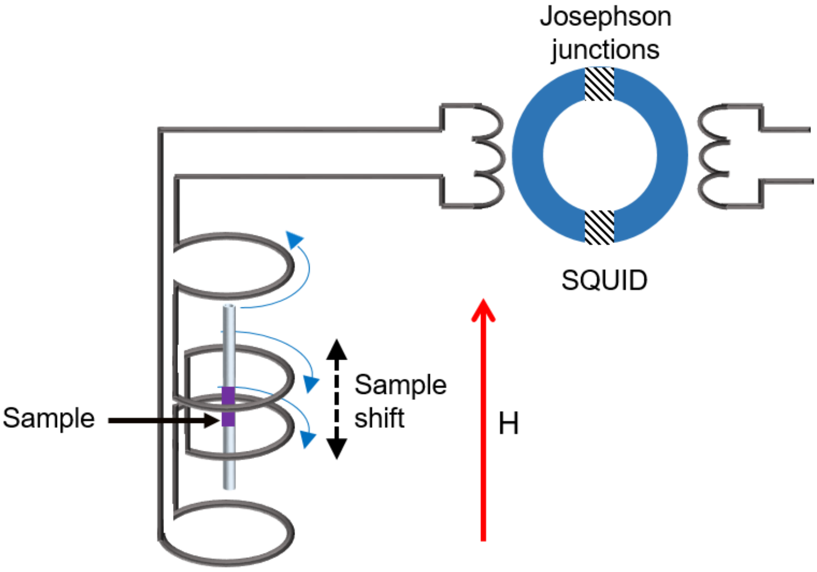

Figure A17. Schematic description of the measurement using a DC superconducting quantum interference device.

The DC SQUID magnetometer used in this Thesis is a commercial MPMS 3 (Quantum Design) system shown in Figure A18, which is located at the general research services of the University of the Basque Country. The system has a 7 T magnet, unlimited temperature control between 5 and 400 K, and a sensitivity of 10^{-8} emu. For the measurement of the magnetic response of the nanodiscs, we used the vibrating mode with an amplitude of oscillation of 5 mm.

Figure A18. SQUID located at the general research services of the University of the Basque Country (UPV/EHU).

Vibrating sample magnetometry (VSM)

The vibrating sample magnetometer [10] measures the magnetic moment of a sample when it is vibrated perpendicularly to a uniform magnetizing field. With this instrument, changes as small as 10^{-5} to 10^{-6} emu can be detected. The sample is vibrated perpendicularly to the applied field by a loudspeaker assembly. The oscillating magnetic field of the vibrating sample induces a voltage in the stationary detection coils (pick-up coils) and from measurements of this voltage the magnetic properties of the sample are deduced. The measurement mechanism is schematized in Figure A19.

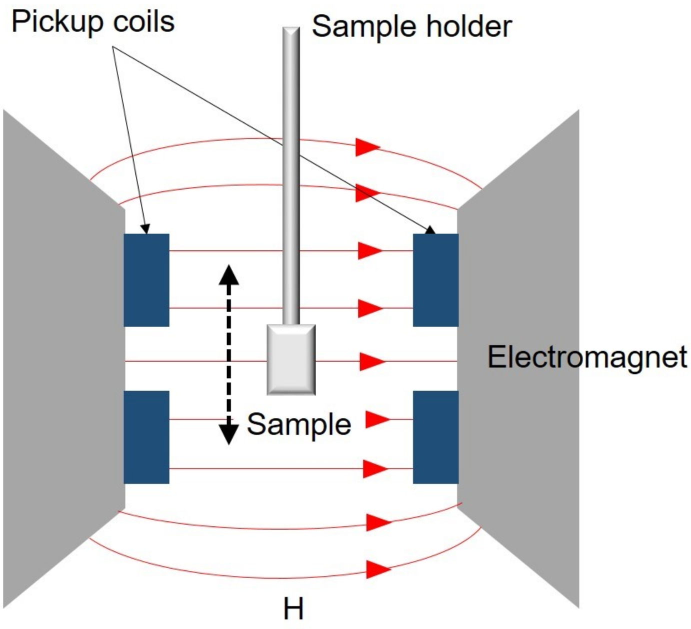

Figure A19. Schematic description of the vibrating sample magnetometry.

The VSM measurements of the nanodiscs in water were performed in the Cavendish Laboratory (University of Cambridge). The experimental set-up is shown in Figure A20. The electromagnet from GMW (model 3472-70) can create a magnetic field up to 1.75 T. 200 µl of the nanodiscs/microdiscs' aqueous solution were encapsulated in small cylindrical cases (6 mm in diameter). For the low temperature measurements, nitrogen liquid was used.

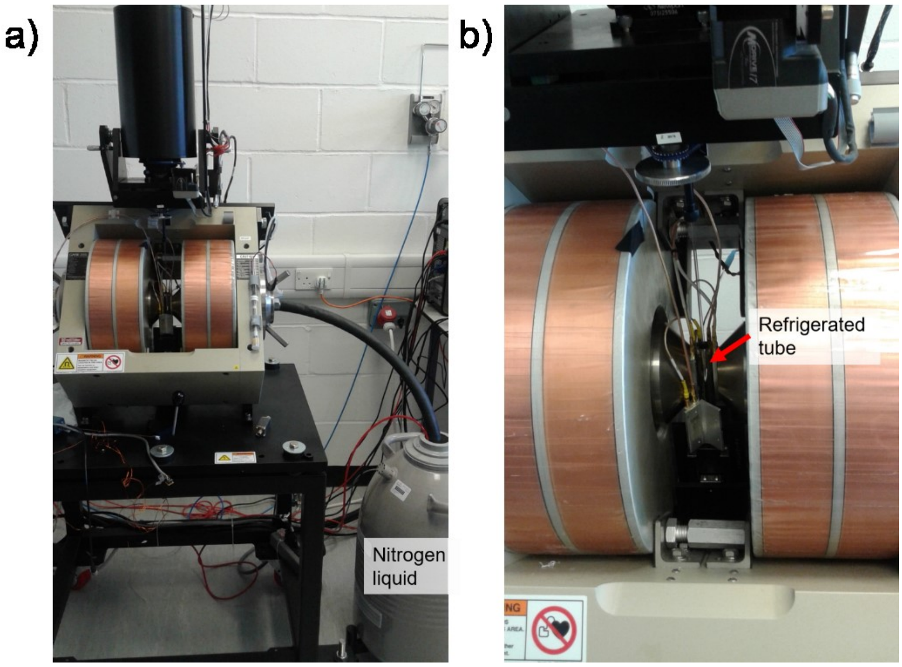

Figure A20. Vibrating sample magnetometer located at the Cavendish Laboratory, University of Cambridge (UK). General view (*a*) and details of sample holder and the refrigerated tube (*b*).

Fluorescence microscopy

Fluorescence microscopy [11] is currently one of the more powerful and versatile techniques available for biological studies. The technique uses fluorophores that have large absorption cross-sections at a specific wavelength and emit light at a longer wavelength. Because of the combination of high absorption cross-section and high quantum efficiency, fluorophore labelled molecules are very bright and readily distinguishable from other background signals. With the development of genetically encoded fluorescent proteins, it has become possible to image protein expression, localization, and activity in living cells. The fundamental working mechanism of the fluorescence microscopy is schematized in Figure A21*a*.

The fluorescence microscope used in this Thesis is a commercial Nikon Eclipse-Ni shown in the Figure A21*b*. The microscope has two cameras: Nikon DS-Fi2 and a high-resolution Zyla sCMOS (Andor, an Oxford Instruments Company).

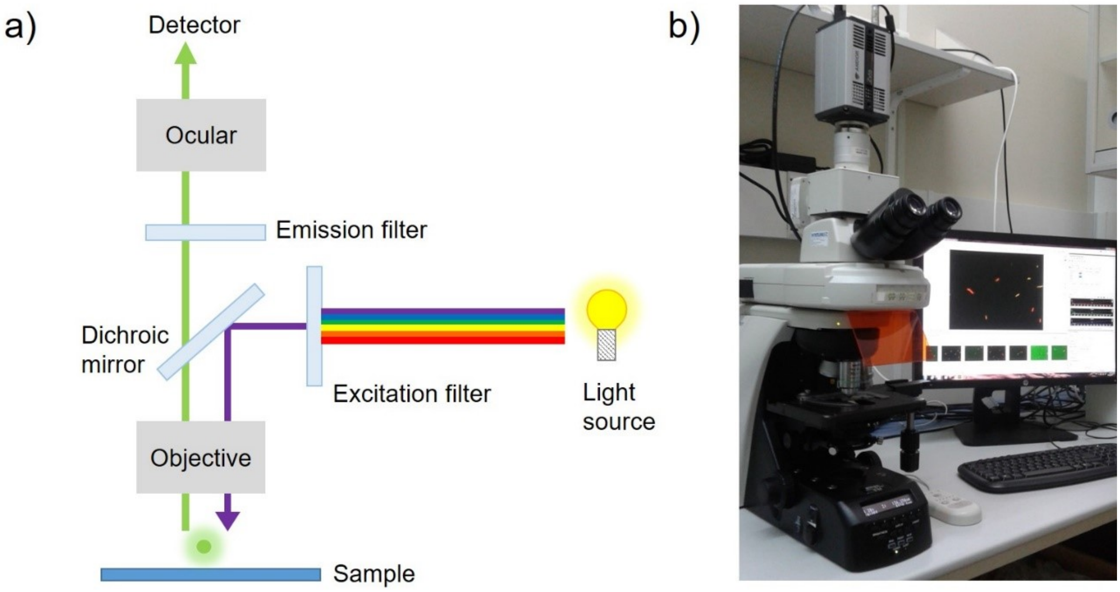

Figure A21. Schematic description of the fluorescence microscopy (*a*) and the fluorescence microscope (*b*) located at the Department of Immunology, Microbiology and Parasitology of the University of the Basque Country (UPV/EHU).

Live cell recorder

The live cell videos were recorded by a Nikon BioStation IM that combines a cell incubator that provides control of temperature, humidity and gas concentration, with a monitoring system. The equipment is presented in Figure A22.

Figure A22. Live cell recorder located at the general research service at the Medicine Faculty of the University of the Basque Country (UPV/EHU).

References

[1] P. J. Kelly and R. D. Arnell, “Magnetron Sputtering: a review of recent developments and applications”, *Vacuum*, vol. 56, pp. 159-172, 2000.

[2] D. Mailly and C. Vieu, “Nanoscience: Nanotechnology and Nanophysics”, *Springer*, 2007.

[3] M. J. Madou, “Fundamentals of Microfabrication and Nanotechnology”, vol. II, *CRC Press*, 2012.

[4] C. W. Oatley, W. C. Nixon and R. F. W. Pease, “Scanning Electron Microscopy”, *Advances in Electronics and Electron Physics*, vol. 21, pp. 181-247, 1966.

[5] L. Reimer, “Transmission Electron Microscopy, Physics of Image Formation and Microanalysis”, *Springer series in Optical Sciences*, 1984.

[6] F. J. Giessibl, “Advances in atomic force microscopy”, *Reviews of Modern Physics*, vol. 75, pp. 949-983, 2003.

[7] U. Hartmann, “Magnetic Force Microscopy”, *Annual Review of Materials Science*, vol. 29, pp. 53–87, 1999.

[8] Z. Q. Qiu and S. D. Bader, “Surface magneto-optic Kerr effect”, *Review of Scientific Instruments*, vol. 71, pp. 1243, 2000.

[9] J. Clarke, W. M. Goubau and M. B. Ketchen, “Tunnel Junction dc SQUID: Fabrication, Operation, and Performance”, *Journal of Low Temperature Physics*, vol. 25, 1976.

[10] S. Foner, “A versatile and sensitive vibrating sample magnetometer”, *Review of Scientific Instruments*, vol. 30, pp. 548, 1959.

[11] J. W. Lichtman and J-A. Conchell, “Fluorescence Microscopy”, *Nature Methods*, vol. 2, pp. 910-919, 2005.

Appendix B

Analytical calculations

This theory was developed by Prof. Guslienko to interpret our results. Cylindrical coordinates $(\boldsymbol{\rho}, \boldsymbol{\varphi})$ are used to describe the in-plane radius vector $\boldsymbol{\rho}(\boldsymbol{x}, \boldsymbol{y})$ and assume that the disc magnetisation can be averaged over the thickness, that is, over the $\boldsymbol{z}$ coordinate. The position of the vortex core $\mathbf{X} = (X, Y)$ in the disc is expressed in reduced variables as $\mathbf{s} = \mathbf{X}/R$. If an external in-plane magnetic field $\mathbf{H}$ is applied, then it is convenient to express the dot magnetisation as $\mathbf{M}(\boldsymbol{\rho}, \mathbf{X}) = \mathbf{M}(\boldsymbol{\rho} - \mathbf{X})$, assuming that the vortex is rigidly shifted from its equilibrium position at the disc centre.

The total magnetic energy $W = L \int d^2\boldsymbol{\rho} w$ can be decomposed in series on the small parameter $|s| \ll 1$ as

$$W(s) = W(0) + \kappa |s|^2/2 - \mu_0 H \langle M \rangle V \tag{B1}$$

where κ is the stiffness coefficient, and $\langle M \rangle$ is the averaged disc magnetisation component along the in-plane bias magnetic field H direction.

The problem is reduced to the calculation of the magnetic energy $W(s)$. We use the complex variables $z = (x + iy)/R$ and an analytic function $f(z)$ to describe the displaced vortex. The magnetisation components can be expressed as

$$m_x + i m_y = \frac{2f(z)}{1 + |f(z)|^2}, \quad m_z = \frac{1 - |f(z)|^2}{1 + |f(z)|^2}. \tag{B2}$$

We apply the rigid vortex model $f(z) = e^{i\Phi_0}(z - s)/c$, which corresponds to the vortex equilibrium skyrmion-like magnetisation profile $cos\Theta_0(\rho) = (R_c^2 - \rho^2)/(R_c^2 + \rho^2)$. Here, $c = R_c/R \geq 1$ is the reduced vortex core radius (the case of

$c \ll 1$ was considered by Guslienko *et al.* (Ref. [5], Chapter 2) and $\Phi_0 = C\pi/2$ ($C = \pm 1$ is the vortex chirality).

According to Eq. B1 there are exchange and magnetostatic contributions to the disc magnetic energy of the vortex displaced from the dot centre. The exchange contribution to the stiffness coefficient κ is $\kappa_{ex}(c) = -8ATc^2/(1+c^2)^3$. To calculate the vortex magnetostatic energy w_m we distinguish the energy of the bulk, side surface and face disc surface magnetic charges. The energy cannot be simply expressed via the analytical function $f(z)$. Therefore, we used a direct calculation of w_m via the magnetisation bulk and surface divergence, $div\,\mathbf{m}$ and $(\mathbf{m}\cdot\mathbf{n})$ respectively, where the vector $\mathbf{n}$ is normal to the dot surface ($\mathbf{n} = \hat{\boldsymbol{z}}, \hat{\boldsymbol{\rho}}$ for the face and side surface charges, correspondingly). The bulk magnetic charges are absent within the rigid vortex model ($div\,\mathbf{m} = 0$). The magnetostatic energy of the face and side surface charges of the displaced vortex can be calculated by the equation

$$W_m(\mathbf{s}) = \frac{1}{2}(\mu_0/4\pi)M_s^2 \int dS \int dS' \frac{m_n(\mathbf{r},\mathbf{s})m_n(\mathbf{r}',\mathbf{s})}{|\mathbf{r}-\mathbf{r}'|} \qquad \text{(B3)}$$

where $m_n = (\mathbf{m}\cdot\mathbf{n})$ is the surface divergence.

The side surface charges stiffness coefficient, calculated from Eq. B3, is

$$\kappa_m^s(c,\beta) = 4\pi M_s^2 R^2 T c^2 (1+c^2)^{-3} F_1(\beta),$$

where

$$F_1(\beta) = \int_0^\infty dt t^{-1} f(\beta t) J_1^2(t), \quad f(x) = 1 - \big(1 - exp(-x)\big)/x,$$

and $\beta = T/R$ is the disc aspect ratio. The face magnetic charges stiffness coefficient is calculated as

$$\kappa_m^f(c,\beta) = 8\pi M_s^2 R^2 T/(\beta c^2) \int_0^\infty dk (1 - \exp(\beta k))\, F(k,c),$$

where the function $F(k,c)$ is given by

$$F(k,c) = 2\left[\int_0^1 d\rho \rho^2 J_1(k\rho)/(1+\tau)^2\right]^2 /c^2 +$$

$$+\int_0^1 d\rho\rho J_0(k\rho)(1-\tau)/(1+\tau)\int_0^1 d\rho\rho J_0(k\rho)(\tau-1)/(1+\tau)^3,$$

and $\tau = (\rho/c)^2$.

We can write the total stiffness coefficient

$$\kappa = \kappa_{ex} + \kappa_m^s + \kappa_m^f$$

(in units of $\mu_0 M_s^2 V$) for the circular disc as

$$\kappa(c,\beta,R) = -\frac{4}{\pi}\left(\frac{l_{ex}}{R}\right)^2 \frac{c^2}{(1+c^2)^3} + \frac{4c^2}{(1+c^2)^2}F_1(\beta) +$$

$$+\frac{8}{c^2\beta}\int_0^\infty dk(1-\exp(-\beta k))F(k,c) \tag{B4}$$

where $l_{ex} = \sqrt{2A}/M_s$ is the exchange length.

Calculating the average in-plane dot magnetisation, the Zeeman energy density can be expressed as

$$w_H(s) = -\frac{2c}{1+c^2}H\mu_0 M_s.$$

(B5)

The equilibrium vortex core position displacement s_0 in a small in-plane magnetic field (H) can be calculated from the equation $\partial W/\partial \mathrm{s} = 0$ as

$$s_0 = 2cH/\kappa(1+c^2)M_s.$$

Following the Ref. [5] of the Chapter 2, we consider that the field at which the vortex core centre crosses the disc border $s_0 = 1$ should give a good estimation of the vortex annihilation field, H_{an}, for $c > 1$.

$$H_{an}(c,\beta,R) = \frac{(1+c^2)}{2c}\kappa(c,\beta,R)M_s \tag{B6}$$

where the stiffness coefficient $\boldsymbol{\kappa(c,\beta,R)}$ is given by Eq. B4.

Appendix C

List of publications

1. M. Goiriena-Goikoetxea, K. Y. Guslienko, M. Rouco, I. Orue, E. Berganza, M. Jaafar, A. Asenjo, M. L. Fdez-Gubieda, L. Fernández Barquín and A. Garcia-Arribas, "Magnetization reversal in circular vortex dots of small radius", *Nanoscale*, vol. 9, 11269, 2017.
2. M. Goiriena-Goikoetxea, A. Garcia-Arribas, M. Rouco, A. V. Svalov and J. M. Barandiaran, "High-yield fabrication of 60 nm Permalloy nanodiscs in well-defined magnetic vortex state for biomedical applications", *Nanotechnology*, vol. 27, 175302, 2016 (Featured on the cover of *Nanotechnology* in the volume 27, number 17, 29 April 2016)

Other publications not directly related to the Thesis:

3. A. García-Arribas, M. Goiriena-Goikoetxea, E. Fernández and J. M. Barandiaran, "Magnetoimpedance in Samples with patterned surfaces for the detection of magnetic particles and ferrofluids", *IEEE Transactions on Magnetics,* 2017 (in press) DOI: 10.1109/TMAG.2017.2705349
4. A. García-Arribas, L. Combarro, M. Goiriena-Goikoetxea, G. V. Kurlyandskaya, A. V. Svalov, E. Fernández, I. Orue and J. Feuchtwanger, "Thin-film magnetoimpedance structures onto flexible substrates as deformation sensors", *IEEE Transactions on Magnetics*, vol. 53, 2000605, 2016.
5. E. Axpe, L. Bugnicourt, D. Merida, M. Goiriena-Goikoetxea, I. Unzueta, R. Sanchez-Eugenia, J. A. Garcia, F. Plazaola and S. Contera, "Sub-nanoscale free volume and local elastic modulus of chitosan/carbon nanotube biomimetic nanocomposite scaffold-materials", *Journal of Materials Chemistry B*, vol. 3, pp. 3169-3176, 2015.